Brain States in Health and Disease: Insights from Neuroimaging and Theoretical Neuroscience

Anira Escrichs

TESI DOCTORAL UPF / ANY 2022

Director: Gustavo Deco
Department: Engineering and Information and
Communication Technologies

upf. **Universitat**
Pompeu Fabra
Barcelona

Abstract

Spontaneous brain activity persists and transitions between brain states, such as from wakefulness to sleep, from development to ageing, or it may transition to pathological states such as coma. Nevertheless, a consensual definition of brain state remains elusive, and the best way of measuring its dynamical complexity is unknown. Here, we propose whole-brain computational frameworks combined with neuroimaging data to characterise brain states in health and disease. We show that such states exhibit unique complex dynamics across spacetime scales. Furthermore, we show that whole-brain models can be fitted to such states to study *in silico* the capacity of brain areas to promote a transition, e.g., from disease to health. Finally, we show that perturbations of this model can measure the brain's reactivity in different conscious and unconscious states. In the long term, these methods may open new ways for clinical interventions to rebalance brain disorders.

Keywords— resting-state fMRI, dynamical complexity, turbulence, whole-brain computational modelling, *in silico* perturbations, brain dynamics, brain states, ageing, meditation, sleep, disorders of consciousness

Resum

L'activitat cerebral espontània persisteix i transiciona entre estats cerebrals, com ara de la vigília al son, del desenvolupament a l'envelliment, o pot transicionar a estats patològics com el coma. Tanmateix, una definició consensuada d'estat cerebral segueix sent esquiva, i es desconeix la millor manera de mesurar la seva complexitat dinàmica. Aquí, proposem marcs computacionals de tot el cervell per caracteritzar estats cerebrals en la salut i la malaltia. Mostrem que aquests estats presenten dinàmiques complexes úniques a través d'escales espacio-temporals. Addicionalment, ajustem models de tot el cervell als estats cerebrals per estudiar *in silico* la capacitat de les àrees cerebrals per promoure una transició, per exemple, de la malaltia a la salut. Finalment, mostrem que les pertorbacions d'aquest model poden mesurar la reactivitat del cervell en estats conscients i inconscients. A llarg termini, aquests mètodes poden obrir noves vies per reequilibrar els transtorns cerebrals.

Keywords— IRMf en estat de repòs, complexitat dinàmica, turbulència, models computacionals a gran escala, pertorbacions *in silico*, estats cerebrals, envelliment, meditació, son, trastorns de la consciència

Foreword

The present thesis has been developed under the supervision of Prof. Dr Gustavo Deco in the Computational Neuroscience Group at the Center for Brain and Cognition, Department of Engineering and Information and Communication Technologies, at Pompeu Fabra University. It has been financially supported by the Catalan project Imagenoma de L'Envelliment (Ageing Imageomics Study); the project Brain Connectivity during Stroke Recovery and Rehabilitation (id. 201725.33), funded by the Fundació La Marato de TV3 2017 (grant agreement 201725.33); and the HBP SGA3 Human Brain Project Specific Grant Agreement 3 (grant agreement no. 945539), funded by the EU H2020 FET Flagship programme.

The thesis is presented as a compendium of publications following the regulations of the PhD school. In particular, it contains four first-author articles published in internationally recognised, peer-reviewed indexed scientific journals, presented using the university affiliation. In addition, a list of additional works is presented as the product of national and international collaborations conducted during the PhD period.

Outcomes

1. ***Escrichs, A.**, *Perl, Y.S., Uribe, C., Camara, E., Türker, B., Pyatigorskaya, N., López-González, A., Pallavicini, C., Panda, R., Annen, J., Gosseries, O., Laureys, S.,Naccache, L., Sitt, J., Laufs, H., Tagliazucchi, E., Kringelbach, M. L., and Deco, G. (2022). *Unifying turbulent dynamics framework distinguishes different brain states.* Communications biology, 5(1), 638. `https://doi.org/10.1038/s42003-022-03576-6`

2. **Escrichs, A.**, Perl, Y.S., Martinez-Molina, N., Biarnes, C., Garre, J., Fernandez-Real, J.M., Ramos, R., Marti, R., Pamplona, R., Brugada, R., Serena, J., Ramio-Torrenta, L., Coll, G., Gallart, L., Barretina, J., Vilanova, J., Mayneris-Perxachs, J., Saba, L., Pedraza, S., Kringelbach, M.L., Puig, J., and Deco, G. (2022). *The effect of external stimulation on functional networks in the aging healthy human brain.* Cerebral cortex (New York, N.Y. : 1991), bhac064. `https://doi.org/10.1093/cercor/bhac064`

3. **Escrichs, A.**, Biarnes, C., Garre-Olmo, J., Fernández-Real, J. M., Ramos, R., Pamplona, R., Brugada, R., Serena, J., Ramio-Torrenta, L., Coll-De-

Tuerom G., Gallart, L., Barretina, J., Vilanova, J.C,, Mayneris-Perxachs, J., Essig, M., Figley, C.R., Pedraza, S., Puig, J., and Deco, G. (2020). *Whole-brain dynamics in aging: disruptions in functional connectivity and the role of the rich club.* Cerebral cortex (New York, N.Y. : 1991), 31(5), 2466–2481. `https://doi.org/10.1093/cercor/bhaa367`

4. **Escrichs, A.**, Sanjuán, A., Atasoy, S., López, A., Garrido, C., Camara, E., and Deco, G. (2019). *Characterizing the Dynamical Complexity Underlying Meditation.* Frontiers in systems neuroscience, 13, 27. `https://doi.org/10.3389/fnsys.2019.00027`

Related works

1. Sanz Perl, Y., **Escrichs, A.,** Tagliazucchi, E., Kringelbach, M.L., Deco G. (2022). *Strength dependent perturbation of whole-brain model working in different regimes reveals the role of fluctuations in brain dynamics.* PLoS Comput Biol 18(11): e1010662. `https://doi.org/10.1371/journal.pcbi.1010662`

2. Soler-Toscano, F., Galadí, J., **Escrichs, A.**, Perl, Y.S., López-González, A., Sitt, J., Annen, J., Gosseries, O., Thibaut, A., Panda, R., Esteban, F.J, Laureys, S., Kringelbach M.L., Langa, J., and Deco G. (2022). *What lies underneath: Precise classification of brain states using time-dependent topological structure of dynamics.* PLoS Comput Biol 18(9): e1010412. `https://doi.org/10.1371/journal.pcbi.1010412`

3. Panda, R., Thibaut, A., Lopez-Gonzalez, A., **Escrichs, A.**, Bahri, M. A., Hillebrand, A., Deco, G., Laureys, S., Gosseries, O., Annen, J., and Tewarie, P. (2021b). *Disruption in structural-functional network repertoire and time resolved subcortical-frontoparietal connectivity in disorders of consciousness.* eLife, 11, e77462. `https://doi.org/10.7554/eLife.77462`

4. *Uribe, C., ***Escrichs, A.**, De Filippi, E., Perl, Y.S., Junque, C., Gomez-Gil, E., Kringelbach, M. L., Guillamon, A., and Deco, G. (2022). *Whole-brain dynamics differentiate among cisgender and transgender individuals.* Hum. Brain Mapp, 43(13), 4103–4115. `https://doi.org/10.1002/hbm.25905`

5. De Filippi, E., Marins, T., **Escrichs, A.**, Gilson, M., Moll, J., Tovar-Moll, F., and Deco, G. (2022). *One session of fMRI-Neurofeedback training on motor imagery modulates whole-brain effective connectivity and dynamical*

complexity. Cerebral Cortex Communications, Volume 3, Issue 3, 2022, tgac027. `https://doi.org/10.1093/texcom/tgac027`

6. Mayneris-Perxachs, J., Castells-Nobau, A., Arnoriaga-Rodríguez, M., Martin, M., de la Vega-Correa, L., Zapata, C., Burokas, A., Blasco, G., Coll, C., **Escrichs, A.**, Biarnés, C., Moreno-Navarrete, J. M., Puig, J., Garre-Olmo, J., Ramos, R., Pedraza, S., Brugada, R., Vilanova, J. C., Serena, J., Gich, J., Ramió-Torrentà, L., Pérez-Brocal, V., Moya, A., Pamplona, R., Sol, J., Jové, M., Ricart, W., Portero-Otin, M., Deco, G., Maldonado, R., and Fernández-Real, J. M. (2022). *Microbiota alterations in proline metabolism impact depression.* Cell Metab., 34(5):681–701.e10. `https://doi.org/10.1016/j.cmet.2022.04.001`

7. *De Filippi, E., ***Escrichs, A.**, Càmara, E., Garrido, C., Marins, T., Marti Sanchez-Fibla, Gilson, M., and Deco, G. (2022). *Meditation-induced effects on whole-brain structural and effective connectivity.* Brain structure and function, 1-16. `https://doi.org/10.1007/s00429-022-02496-9`

8. Cruzat, J., Perl, Y. S., **Escrichs, A.**, Vohryzek, J., Timmermann, C., Roseman, L., Luppi, A. I., Ibañez, A., Nutt,D., Carhart-Harris, R., Tagliazucchi, E., Deco, G., and Kringelbach, M. L. (2022). *Effects of classic psychedelic drugs on turbulent signatures in brain dynamics.* Network Neuroscience, pages 1–42. `https://doi.org/10.1162/netn_a_00250`

9. De Filippi, E., Uribe, C., Avila-Varela, D., Martínez-Molina, N., Gashaj, V., Pritschet L., Santander, T., Jacobs, E., Kringelbach, M.L., Perl Y.S., Deco, G., and **Escrichs, A.** (2021). *The Menstrual Cycle Modulates Whole-Brain Turbulent Dynamics.* Frontiers in Neuroscience, 15. `https://doi.org/10.3389/fnins.2021.753820`

10. López-González, A., Panda, R., Ponce-Alvarez, A., Zamora-López, G., **Escrichs, A.**, Martial, C., Gosseries, O., Kringelbach, M. L., Annen, J., Laureys, S., and Deco, G. (2021). *Loss of consciousness reduces the stability of brain hubs and the heterogeneity of brain dynamics.* Communications biology, 4(1), 1037. `https://doi.org/10.1038/s42003-021-02537-9`

11. Puig J, Biarnés C, Pedraza S, [et al. including **Escrichs A**] (2020). *The Aging Imageomics Study: rationale, design and baseline characteristics of the study population.* Mechanisms of ageing and development, 189, 111257. `https://doi.org/10.1016/j.mad.2020.111257`

12. Panda, R., Lopez-Gonzalez, A., Gilson, M., Gosseries, O., Thibaut, A., Frasso,G., Cecconi, B., **Escrichs, A.**, group Collaborators, G., Deco, G.,

Laureys, S.,Zamora-Lopez, G., and Annen, J. (2021). *Posterior integration and thalamo-frontotemporal broadcasting are impaired in disorders of consciousness.* bioRxiv, page 2021.11.08.467694. `https://doi.org/10.1101/2021.11.08.467694`

13. *Martinez-Molina, N., ***Escrichs, A.,** Perl., YS, Sarkamo, T., Sihvonen, A., Kringelbach, ML and Deco, G (2022). *The evolution of whole-brain turbulent dynamics during recovery from traumatic brain injury.* bioRxiv, page 2022.11.30.518501. `https://doi.org/10.1101/2022.11.30.518501`

*equal contribution

Contents

List of Figures

Chapter 1

INTRODUCTION

1.1 The resting state

In recent years, the so-called resting state has become a central focus in the scientific community and has been mainly investigated with non-invasive neuroimaging techniques to study human brain function. Probably, the first evidence that the brain at rest contains information about its functional organisation was in the 1990s [Biswal et al., 1995]. The authors examined the slow (< 0.1Hz) spontaneous fluctuations in the blood-oxygenation-level-dependent (BOLD) signal of functional magnetic resonance imaging (fMRI) to study how two structurally connected cortical areas (i.e., the left and right brain areas of the motor cortex) functionally correlate when the brain does not perform any specific task. They observed a functional connectivity (FC) pattern of brain activity that seemed similar to the activation pattern when subjects executed a motor task, thus identifying the well-known sensorimotor network during the resting state. This finding progressively shifted the neuroscience community from studying task-related fMRI experiments, where subjects responded to specific stimuli or tasks, to studying resting state fMRI experiments, where subjects remain quiet inside the scanner without thinking about anything in particular (i.e., the resting state). Since then, several resting state fMRI studies have focused exclusively on the identification and characterisation of resting state brain networks [Lowe et al.,

1998, Greicius et al., 2003, Beckmann et al., 2005, Rogers et al., 2007, Fox and Raichle, 2007, Damoiseaux et al., 2006, Deco et al., 2013]. Several functional resting state networks have been identified, such as the default mode network (DMN) and the visual, subcortical, cerebellum, executive control (also called dorsal attention network [DAN]), ventral attention, and auditory networks. Such networks have been shown to be spatially consistent across subjects, and their spontaneous BOLD activity shows a close correspondence between task conditions and rest **(Figure 1.1)** [Damoiseaux et al., 2006, Smith et al., 2009]. One of the resting state networks receiving the closest attention has been the DMN. Brain areas of the DMN show greater activity during the resting state than during task performance [Raichle et al., 2001] and its activity is anti-correlated with activity in the DAN [Fox et al., 2005, Sridharan et al., 2008], reflecting a brain mechanism controlling the shift between internally- and externally-directed cognition [Clare Kelly et al., 2008, Sherman et al., 2014].

For clinical applications, resting state fMRI has been particularly useful for measuring brain activity in patients who cannot perform a task or are unable to communicate, such as patients in a minimally conscious state (MCS), in an unresponsive wakefulness state (UWS), or with locked-in syndrome [Laureys et al., 2004, Owen et al., 2006, Fernández-Espejo and Owen, 2013, Panda et al., 2021b]. Furthermore, several studies have applied resting state fMRI to study brain disorders such as depression, schizophrenia, stroke, or Parkinson's disease, among others [Drysdale et al., 2016, Adhikari et al., 2017, Saenger et al., 2017, Puig et al., 2018, Yu et al., 2019, Mayneris-Perxachs et al., 2022] (for clinical reviews, see [Rosazza and Minati, 2011, Fox and Greicius, 2010]).

In addition, studies that have combined resting state fMRI and diffusion tensor imaging (DTI) have tried to reveal the brain's structure-function relationship. Human brain structural connectivity (SC) has been mainly measured using DTI, a non-invasive neuroimaging technique that makes it possible to track brain white matter fibers by measuring the random diffusion-driven motion of water molecules [Le Bihan, 2003, Sporns et al., 2005]. In particular, it has been shown that direct white matter pathways exist between brain areas of the resting state networks and that FC correlates with the underlying SC, indicating that resting state networks emerge from the underlying anatomical connectivity [Koch et al.,
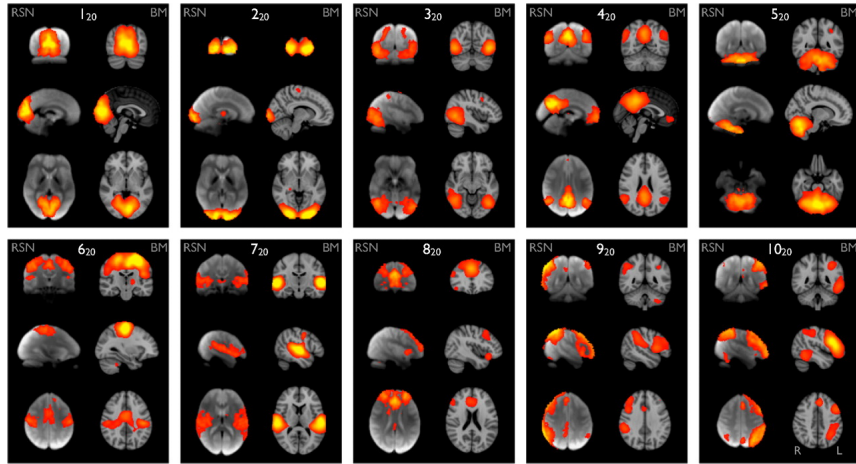
Figure 1.1: ICA maps showing a close correspondence between tasks and rest. These ICA maps from resting state fMRI data in healthy subjects show a close correspondence between rest and task conditions. Components 1, 2, and 3 correspond to visual networks. Component 4 clearly shows the default mode network. Component 5 corresponds to the cerebellum. Component 6 corresponds to the sensorimotor network. Component 7 shows the auditory network. Component 8 corresponds to the executive control network. Components 9 and 10 show the left and right frontoparietal networks. Figure adapted from [Smith et al., 2009].

2002, Van Den Heuvel et al., 2009, Hagmann et al., 2008, Greicius et al., 2009, Deco et al., 2011]. However, FC has also been observed between brain areas where there are no white matter connections, which suggests that those functional correlations are mediated by indirect structural connections, such as, for example, a third brain area [Damoiseaux et al., 2006, Deco et al., 2011, Van Den Heuvel et al., 2009, Honey et al., 2009]. Consequently, even though resting state networks can depend on the underlying structural connectivity, the brain activity cannot be understood only in these terms, and the missing link in those studies has been to consider the underlying brain dynamics [Deco et al., 2013].

1.2 Whole-brain dynamics

Traditionally, FC has been estimated as a correlation coefficient over an entire scan (i.e., static or grand average FC). Nevertheless, collapsing the temporal fluctuations through correlations has led to an oversimplified description of functional brain networks [Zalesky et al., 2014, Allen et al., 2014]. In response to this limitation, recent investigations have focused on studying the temporal evolution of spontaneous fluctuations, showing that brain activity is not static over time but rather shows highly complex temporal dynamics [Honey et al., 2009, Deco et al., 2013, Hutchison et al., 2013, Calhoun et al., 2014, Ponce-Alvarez et al., 2015]. These studies have evidenced that the spatio-temporal structure is essential for understanding the fundamental features of brain networks.

Several methods have been developed for studying how brain networks reconfigure across time. Model-free (also known as data-driven) and model-based frameworks are two conceptual and complementary tools for studying brain dynamics (for reviews, see: [Hutchison et al., 2013, Popovych et al., 2019, Lurie et al., 2020, Bolton et al., 2020]). On the one hand, model-free frameworks refer to those methods that measure brain dynamics changes empirically, that is, from the observed signal data. One of the most common is the sliding-window approach, where the FC is measured at continuous time points within a given window, and sequentially the procedure is repeated by shifting the window until the end of the scan duration. The result is a succession of FC patterns at different time points, displaying how the anatomical organisation fluctuates across time. Similarly, the phase synchronisation approach measures the instantaneous phase between pairs of brain areas at each time point by estimating the Hilbert transform [Glerean et al., 2012, Ponce-Alvarez et al., 2015]. Both techniques (sliding window and Hilbert transform) can be used to apply the k-means clustering approach to identify spatiotemporal patterns across subjects [Allen et al., 2014, Cabral et al., 2017, Deco et al., 2019, Kringelbach and Deco, 2020]. Furthermore, in neuroscience, it has been highly useful to implement tools from physics to describe large-scale brain activity. For example, metastability has been used to measure how the synchronisation between different brain areas fluctuates across time and can be calculated as the standard deviation of the global Kuramoto

order parameter across time in neuroimaging data [Deco and Kringelbach, 2016, Deco et al., 2017a]. This measure obtains the global level of synchronisation of the total oscillating signals of brain areas and is given by the following equation:

$$R(t) = \frac{1}{N} \left| \sum_{k=1}^{n} e^{i\varphi_k(t)} \right| \tag{1.1}$$

where $\varphi_k(t)$ is the phase of each filtered signal in brain area k. Consequently, if the n phases are uniformly distributed, then $R = 0$ (full desynchronisation), whereas if all phases are equal, $R = 1$ (full synchronisation).

Recently, however, the concept of metastability has been extended to study not only the global level of synchronisation of the brain but also its local level across spacetime scales. Notably, the local Kuramoto order parameter, defined as the local level of system synchronisation across spacetime, offers a precise characterisation of the level of turbulence and the spatiotemporal characteristics of the brain [Deco and Kringelbach, 2020, Deco et al., 2021a]. That is, metastability measures the variability across time of the global level of synchronisation of the system, whereas turbulence measures the local level of synchronisation. Such local synchronisation between brain areas has been related to the rotational vortices described in fluid dynamics, and the size of these vortices determines the spatial scales where the information processing is evaluated, i.e., in the so-called vortex space. In fluid dynamics, turbulence provides the optimal transmission of energy and information in a system [Frisch, 1995, Kolmogorov, 1941a, Kolmogorov, 1941b, Kuramoto, 1984], whilst in neuroscience, turbulence has shown to play an essential role in facilitating the efficient transmission of information in the brain [Deco and Kringelbach, 2020, Deco et al., 2021b]. This framework is explained in detail in Chapter 2.

On the other hand, the model-based approach refers to methods that model the underlying dynamics from the empirical data in order to find a mechanistic explanation of brain dynamics. Such computational models are fundamental for studying the relation between the underlying anatomy and whole-brain dynamics. Several approximations of realistic brain models have been employed to model local dynamics, from spiking networks

5

to mean-field models [Ghosh et al., 2008, Honey et al., 2009, Demirtaş et al., 2017, Deco and Jirsa, 2012]. However, models of coupled non-linear oscillators can capture with higher precision the fundamental features of mesoscopic brain dynamics, e.g., the interplay between local and global brain dynamics. Oscillators have been modelled to study synchronisation in many physical and biological systems, from linear to non-linear oscillators [Deco et al., 2021b]. One of the main differences between linear and non-linear oscillators is their response to perturbations. When a linear oscillator is perturbed, it oscillates with a different amplitude. In contrast, the amplitude in a non-linear oscillator is self-regulated, meaning that it decays with time, returning to the same region in phase space [García-Morales and Krischer, 2012]. Non-linear oscillators can be described using a universal mathematical model, the so-called Stuart–Landau equation, an ordinary differential equation of a complex order parameter. In neuroscience, the whole-brain model with Stuart-Landau (also known as Hopf) oscillators has been used to model the mesoscopic dynamics of brain areas. This model describes the dynamics of each brain area by a Hopf bifurcation allowing for studying the transition from noisy to oscillatory dynamics [Deco et al., 2017a]. The interactions between Hopf oscillators have allowed researchers to fit and reproduce several aspects of empirical neuroimaging data such as FC, FC dynamics, metastability, and even turbulence [Deco and Kringelbach, 2017, Deco and Kringelbach, 2020, Deco et al., 2021b]. This model is explained in more detail in Chapter 2.

1.3   Brain states in health and disease

Spontaneous brain activity persists in different conscious and unconscious brain states such as psychedelic [Cruzat et al., 2022, Carhart-Harris et al., 2016], meditation [Escrichs et al., 2019, De Filippi et al., 2022], sleep [Jobst et al., 2017, Deco et al., 2019], or disorders of consciousness states [Soler-Toscano et al., 2022, López-González et al., 2021, Panda et al., 2021a]. Furthermore, such activity transitions among healthy brain states, as in the different sleep stages, from development to ageing, or it can transition to pathological states such as coma [Goldman et al., 2019]. Characterising the underlying dynamics of brain states and their transitions can provide a better understanding of brain function and cognition in both health

and disease. Nonetheless, there is no consensual and precise definition of brain state, and the best way of measuring its dynamical complexity using neuroimaging remains unknown [Kringelbach and Deco, 2020, Escrichs et al., 2022a, Tagliazucchi et al., 2016, Deco et al., 2015, Tononi et al., 1994].

The definition of brain state remains elusive probably because brain dynamics are more complex to understand than previously thought [Deco et al., 2017b]. Earlier descriptions of brain states have been limited to estimating the grand average FC without capturing the underlying dynamics [Carhart-Harris et al., 2016, Tagliazucchi et al., 2016, Kringelbach and Deco, 2020]. Recent definitions suggest capturing the dynamic nature of brain states, e.g., by measuring the broadness of communication across the whole-brain network [Deco et al., 2017b, Deco and Kringelbach, 2017], or by clustering the most similar global spatiotemporal patterns across all subjects [Deco et al., 2019, Cabral et al., 2017]. However, it has been proposed that to characterise brain states, it could be helpful to consider not only the underlying dynamics but also the responses elicited by external perturbations [Goldman et al., 2019, Massimini et al., 2005].

Massimini and colleagues proposed a theoretical measure for assessing dynamical complexity by investigating transcranial magnetic stimulation (TMS) perturbation-elicited brain activity changes during different brain states [Casali et al., 2013, Massimini et al., 2005, Ferrarelli et al., 2010]. The authors presented a theoretical index called the perturbational complexity index (PCI) that measured the brain's response after a direct TMS perturbation. The PCI made it possible to discriminate between different conscious and unconscious brain states (wakefulness, sleep, anaesthesia, and patients recovering from a coma) without requiring the subjects to perform any specific task. In this way, the level of consciousness was measured based on the complexity of cortical interactions, independently of the capacity of the subjects to react to external stimuli.

Another way to study the brain responses evoked by external perturbations is via *in silico* stimulation protocols. Such protocols are based on causal whole-brain computational models, which are helpful for studying how different brain states react to artificial perturbations [Deco et al., 2018, Perl et al., 2021b, Perl et al., 2021a] as well as forcing transitions between them [Kringelbach and Deco, 2020]. Various strategies have been

used to manipulate the perturbations, such as shifting the local dynamics of brain areas in the opposite direction [Deco et al., 2019, Escrichs et al., 2022b], by applying non-sustained perturbations [Deco et al., 2018, Perl et al., 2021a] or by perturbing with an external periodic force [Perl et al., 2021b, Escrichs et al., 2022a]. This mechanistic framework has proven effective in dissociating between brain states in health and disease, such as sleep, disorders of consciousness, or pharmacologically induced loss of consciousness. Altogether, this approach allows studying how different brain states respond to artificial stimulations through an exhaustive exploration of all possible local brain areas and, importantly, is not restricted by ethical limitations of *in vivo* stimulations in humans [Clausen, 2010, Kringelbach et al., 2007, Deco et al., 2018].

At present, however, the challenge remains to develop a dynamical framework that can establish the balance between different brain complexity levels needed to distinguish between conscious and unconscious brain states in health and disease. A consensual definition of brain states would help design mechanistic frameworks for characterising them in terms of dynamical complexity and underlying causal mechanisms, and in turn, it could offer novel ways for translational clinical interventions to rebalance brain disorders.

Chapter 2

HYPOTHESIS AND OBJECTIVES

This thesis leverages recent neuroimaging and theoretical neuroscience advances to extend our understanding of the complex brain dynamics underlying brain states. In particular, we propose, test, and expand different model-free and model-based frameworks in order to characterise, define and simulate brain states in health and disease from empirical neuroimaging data (resting state fMRI and DTI). The general hypothesis is that these frameworks will allow us to extract specific local, global, spatial, and temporal features, as well as causal mechanistic explanations of the brain dynamics underlying such features, and even rebalance the dynamics of brain disorders from a theoretical point of view.

Specific objectives

1. To study dynamical complexity levels from resting state fMRI data using model-free frameworks in expert meditators and healthy controls during meditation and rest *(Article 1)* and during healthy ageing *(Article 2)*.

2. To test a probabilistic framework for describing the spatiotemporal dynamics of whole-brain activity in the healthy ageing human brain.

This probabilistic strategy will typify substates as probability distributions of all participants' common and persistent brain states. This allows for recurrent substates to be detected and characterised in terms of probability of occurrence and frequency *(Article 2)*.

3. To investigate the effect of exhaustive *in silico* stimulations on whole-brain dynamics in the healthy human brain *(Article 3)*. We tested the hypothesis that causal whole-brain modelling combined with *in silico* perturbations could predict optimal stimulation targets to rebalance the underlying brain dynamics in older subjects. In particular, we were interested in forcing transitions from the brain states of older participants to the brain states of middle-aged participants.

4. To test and extend a unifying turbulent dynamics framework for accurately describing and characterising different brain states in health and disease *(Article 4)*. We hypothesised that combining model-free and model-based frameworks would allow us to extract specific features of turbulent dynamics underlying conscious and unconscious states.

Chapter 3

METHODS

> When I meet God, I am going to ask him two questions:
> why relativity? and why turbulence? I really believe he
> will have an answer for the first.
>
> *Werner Heisenberg*

The following section introduces the novel model-free and model-based frameworks implemented and tested in the current thesis to study the dynamical complexity and the underlying causal mechanisms in different brain states using resting state fMRI data. In particular, the meditation dataset comprised experienced meditators and healthy controls during meditation and the resting state. The healthy ageing dataset comprised two groups scanned during the resting state, the middle-aged and older groups. The sleep dataset included healthy subjects during deep sleep and the resting state. Finally, the disorders of consciousness (DoC) dataset included healthy participants and DoC patients diagnosed in a minimally conscious state (MCS) or unresponsive wakefulness state (UWS) (see Appendix for detailed information on the resting state fMRI datasets).

3.1 Model-free frameworks

3.1.1 Intrinsic ignition

We tested and quantified the intrinsic ignition framework using resting state fMRI data in *Article 1* and *Article 2*. In particular, in *Article 1* we analysed a dataset comprised of healthy controls and expert meditators during the resting state and meditation. Furthermore, in *Article 2* we analysed a dataset consisting of middle-aged and older subjects. In this article, the framework was assessed across the whole-brain functional network and independently within eight well-known resting state networks.

The intrinsic ignition framework characterises the dynamical complexity of different brain states by measuring how the level of integration evolves at a time window when a brain area triggers an event **(Figure 3.1)**. An ignition event is captured when the signal of a brain area crosses a fixed threshold [Tagliazucchi et al., 2012]. The phase for each brain area is measured by computing first the Hilbert transform, and then the phase lock matrix $P_{jk}(t)$, which describes the state of phase synchronisation between regions j and k at time t as follows:

$$P_{jk}(t) = \mathrm{e}^{-3|\varphi_j(t) - \varphi_k(t)|} \tag{3.1}$$

where the difference between $\varphi_j(t)$ and $\varphi_k(t)$ is the obtained phase between brain areas j and k at time t. The integration is defined by measuring the length of the largest connected component in the binarised symmetric matrix $P_{jk}(t)$. The integration represents the broadness of communication across the network for each event evoked. Finally, repeating the process for all events crossing the threshold in each brain area, the mean and the standard deviation of the integration across the network are calculated.

3.1.2 PMS

In *Article 2*, we assessed the probabilistic metastable substates (PMS) framework in a large resting state fMRI dataset of healthy human adults to identify recurrent dynamic functional connectivity patterns (here referred to as metastable substates). The PMS fully typifies substates as

stochastic subdivisions of regular and persistent brain states. This allows recurrent substates to be detected and characterised in terms of probability of occurrence and frequency. The fundamental idea of the PMS is to cluster global spatiotemporal patterns, which allows its statistics to be characterised **(Figure 3.1)**.

In brief, the average BOLD time series of each brain area is Hilbert-transformed to yield the phase evolution of the regional signals. Then, the phase coherence for each pair of brain areas at any given time t is computed as the cosine of the phase differences as:

$$dFC(n, p, t) = \cos\left(\theta(n, t) - \theta(p, t)\right) \tag{3.2}$$

This process yields a 3D matrix of $NxNxT$ size, where N is the number of brain areas in the used parcellation, and T indicates the number of volumes acquired across time. Then, the large number of NxN dynamic connectivity matrices are clustered to estimate metastable states. However, reducing the dimensionality of the coherence matrices improves the signal-to-noise ratio and the reliability of any clustering or classification process to describe the states. The method extracts the first $(Nx1)$ eigenvector, i.e., $V1$, of each NxN coherence matrix, from which a discrete number of reduced dynamic patterns can be detected by applying clustering across time points and subjects. Due to the symmetry of the dynamic matrices, each leading eigenvector can be used in turn to estimate the corresponding dynamic matrix. The k-cluster centroids define the metastable substates, each with a probability of occurrence and frequency. This probability description is a biomarker of brain states.

3.1.3 Turbulence

We extended the concept of metastability to study not only global spatial synchronisation but also local spatial synchronisation of brain states by using elements of turbulence theory. The turbulence measure is a generalisation of the concept of metastability. That is, metastability is defined as the variability across time of the global level of synchronisation of the whole system, commonly known as the global Kuramoto order parameter of a dynamical system. Here, however, we studied the local Kuramoto
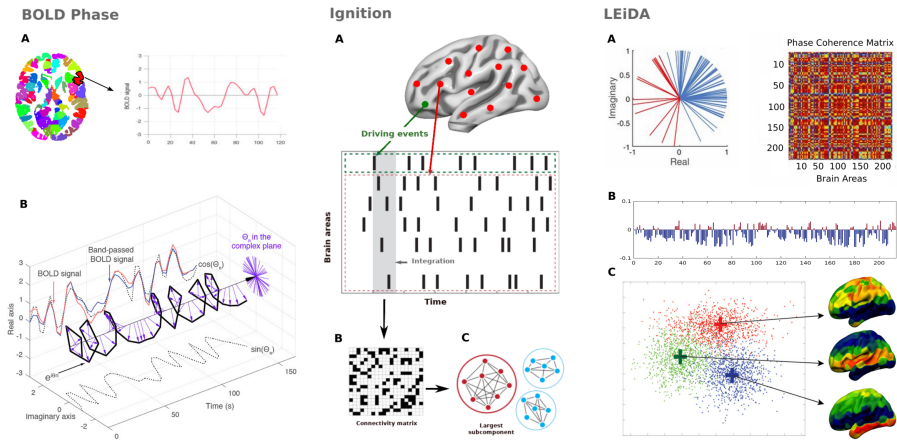
13

Figure 3.1: Intrinsic ignition and PMS frameworks. Both model-free frameworks are based on the phase synchronisation of BOLD signals. The BOLD time series are extracted for each brain area of the parcellation [left panel (A)], and the phase space of the BOLD signal is computed using the Hilbert transform [left panel (B)]. The phase dynamics can be represented in the complex plane as $e^{i\varphi_n}$ (bold black line), the real part as $\cos\varphi$ (dotted black line), and the imaginary part as $\sin\varphi$ (dotted black line). The purple arrows represent the Hilbert phases at each TR. The middle panel shows the intrinsic ignition framework. Events are captured by applying a threshold method [Tagliazucchi et al., 2012] (green area). For each ignition event evoked, the activity in the rest of the network (red stippled area) is measured in the time window [(A), grey area]. A binarised phase lock matrix is obtained from the time window (B). The integration is obtained from this phase lock matrix by calculating the largest subcomponent (i.e., by applying the global integration measure (C) [Deco et al., 2017a, Deco et al., 2015]). The process is repeated for each event and brain area until the end of the scan. Then, the mean ignition and node metastability (as standard deviation) are measured for each brain area. The right panel shows the representation of the LEiDA framework. This method characterises differences between groups in dynamic functional connectivity patterns or metastable substates. The BOLD phases of all brain areas are represented in the complex plane (A). The right panel shows the phase coherence matrix between each pair of brain areas. The leading eigenvector V1(t) from this matrix is extracted (B). A k-means clustering algorithm is applied to obtain the metastable substates from all the leading eigenvectors across time points, number of subjects, and groups (C). Figure adapted from [Escrichs et al., 2021].

14

order parameter in different brain states, defined as the local level of synchronisation across spacetime (**Figure 3.2**).

The amplitude turbulence, $R_\lambda(\bar{x}, t)$, is defined as the modulus of the local Kuramoto order parameter for a given brain area as a function of time:

$$R_\lambda(\bar{x}, t)\, e^{i\vartheta_\lambda(\bar{x},t)} = k \int_{-\infty}^{\infty} d\bar{x}\prime G_\lambda\left(\bar{x} - \bar{x}'\right) e^{i\varphi(\bar{x}',t)} \tag{3.3}$$

where G_λ is the local weighting kernel $G_\lambda(\bar{x}) = e^{-\lambda|\bar{x}|}$, λ is the spatial scaling, $\varphi(\bar{x}, t)$ are the phases of the empirical data computed by the Hilbert transform, and k is the normalisation factor $[\int_{-\infty}^{\infty} d\bar{x}\prime G_\lambda\left(\bar{x} - \bar{x}'\right)^{-1}]$. Thus, R_λ defines local levels of synchronisation as a function of space, $\bar{x}$, and time, t, at a given scale, λ. This measurement captures what we call brain vortex space, R_λ, over time. Finally, the level of amplitude turbulence is defined as the standard deviation across spacetime of the local Kuramoto order parameter (R):

$$D = \sqrt{\langle R_\lambda^2 \rangle_{(n,t)} - \langle R_\lambda \rangle_{(n,t)}^2} \tag{3.4}$$

where the brackets $<>_{(n,t)}$ represent average values across space and time.

Information cascade flow and information cascade

In addition, we defined the information cascade flow (IF), which indicates how the information travels from a given spatial scale λ to a lower scale in consecutive time steps. This measure estimates the information transfer across scales and is computed as the time correlation between the local Kuramoto order parameter at two consecutive scales and times:

$$IF(\lambda) = \langle corr_t(R_\lambda(\bar{x}, t + \Delta t), R_{\lambda - \Delta\lambda}(\bar{x}, t)) \rangle_{\bar{x}} \tag{3.5}$$

where the brackets $<>_{\bar{x}}$ denotes averages across time and space, $t + \Delta t$ corresponds to a time step, and $\Delta\lambda$ is a scale step.

Then, we calculated the information cascade by averaging the information cascade flow across all scales λ to capture the overall information processing behaviour.
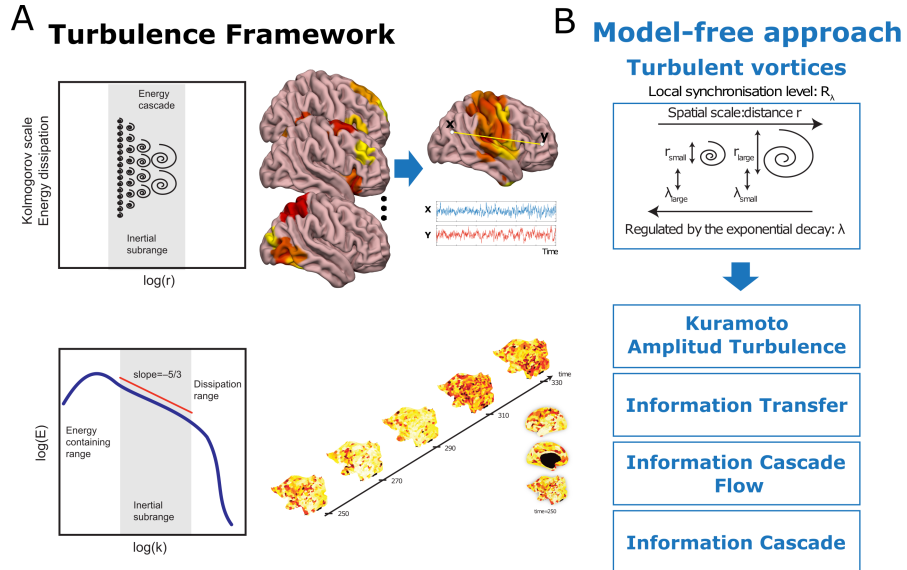
Figure 3.2: Turbulence framework. **A)** In fluids, turbulence is one of the most common dynamical regimes where the mixing movement governs. The energy cascade, i.e., how the energy travels across scales while dissipating, and the statistical properties defined as power laws on the energy levels and structure functions, determine the turbulent behaviour of the fluid (left panel). Recently, using fMRI data, it has been demonstrated that the brain exhibits turbulence-like dynamics (right panel) [Deco and Kringelbach, 2020]. **B)** The analogy between turbulence and brain activity can be determined by the local Kuramoto order parameter (R) at different scales (λ). From this parameter, different brain information measures can be assessed. Namely, the amplitude turbulence, calculated as the standard deviation of the modulus of the local Kuramoto order parameter; the information transfer, calculated as the correlation of local synchronisation across space at a given scale; the information cascade flow, calculated as the correlation of the local Kuramoto order parameter across scales; and the information cascade, calculated as the average across scales of the information cascade flow. Figure adapted from [Escrichs et al., 2022a].

Information transfer correlation

The spatial information transfer indicates how the information travels across space at a specific scale, λ. This measurement is computed as the slope of a linear fitting in the log-log scale of the time correlation between the local Kuramoto order parameter of two brain areas at the same scale as a function of its Euclidean distance (r) within the inertial subrange:

$$log\left(corr_t\left(R_n^\lambda, R_p^\lambda\right)(r)\right) = A^\lambda * log\left(r\right) + B^\lambda \qquad (3.6)$$

where A^λ and B^λ are the fitting parameters for each scale (λ), and r is the spatial distance in the brain. The negative slope (A^λ) stands for the transfer in the spatial direction r of the information in terms of time correlation of the local level of synchronisation. In this respect, when the slope is steeper, the information travels over shorter distances, while a flatter slope indicates that the information is transferred over longer distances.

In *Article 4*, we assessed the turbulence framework in different brain states (resting state, meditation, deep sleep, minimally conscious states and unresponsive wakefulness state) using resting state fMRI data.

3.2 Model-based frameworks

> All models are wrong, but some are useful.
>
> George E. P. Box

3.2.1 The Hopf model

We used the Hopf model to simulate the empirical PMS explained in the previous section and apply *in silico* perturbations to the model in order to force transitions between brain states of different age groups *(Article 3)*. We also used this model to measure the reactivity of information encoding capabilities of the brain in different conscious (rest, meditation) and unconscious (sleep, MCS, UWS) brain states *(Article 4)*.

The Hopf whole-brain model is based on the integration of structure and dynamics **(Figure 3.3)**. The model consists of n anatomically interconnected brain areas based on the parcellation used, coupled with the underlying SC. The local dynamics of each brain area are described using the normal form of a supercritical Hopf bifurcation, which makes it possible to emulate the dynamics for each brain area from noisy to oscillatory dynamics defined as follows:

$$
\begin{aligned}
\frac{\mathrm{d}x_n}{\mathrm{d}t} &= [a_n - x_n^2 - y_n^2]x_n - \omega_n y_n + \beta\eta_n(t) \\
\frac{\mathrm{d}y_n}{\mathrm{d}t} &= [a_n - x_n^2 - y_n^2]y_n + \omega_n x_n + \beta\eta_n(t)
\end{aligned}
\tag{3.7}
$$

where $\eta_n(t)$ is a term to add Gaussian noise with a fixed standard deviation $\beta = 0.02$. This normal form has a supercritical bifurcation at $a_n = 0$, such that for $a_n > 0$ the system is at a stable limit cycle oscillation with frequency $f_n = \omega_n/2\pi$, and for $a_n < 0$ the local dynamics are in a stable point (i.e., noisy state). The intrinsic frequency ω_n of each brain area is obtained from the empirical data.

In order to model the whole-brain dynamics, the underlying SC is added to couple the local dynamics of brain areas n with p and is represented by the coupling term C_{np}. Thus, the whole-brain dynamics are defined by the following set of coupled equations:

$$
\begin{aligned}
\frac{\mathrm{d}x_n}{\mathrm{d}t} &= [a_n - x_n^2 - y_n^2]x_n - \omega_n y_n + G\sum_{p=1}^{N} C_{np}(x_p - x_n) + \beta\eta_n(t) \\
\frac{\mathrm{d}y_n}{\mathrm{d}t} &= [a_n - x_n^2 - y_n^2]y_n + \omega_n x_n + G\sum_{p=1}^{N} C_{np}(y_p - y_n) + \beta\eta_n(t)
\end{aligned}
\tag{3.8}
$$

The variable x_n reproduces the BOLD signal of each brain area. The global coupling factor G is scaled equally for each brain area for simplicity and corresponds to the control parameter of the model. This parameter makes it possible to obtain the dynamical optimal working point of the model (i.e., where the simulations best fit the empirical neuroimaging data).
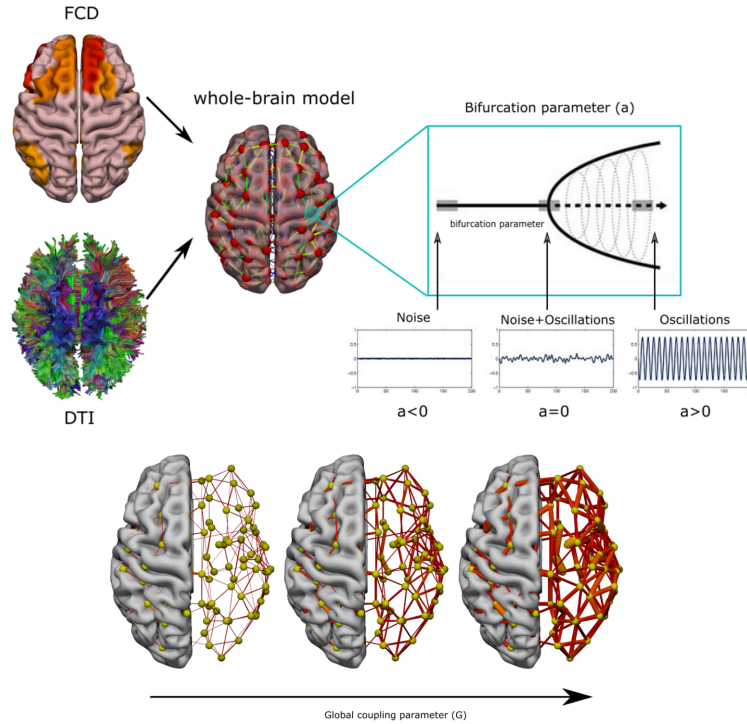
Figure 3.3: The Hopf model. The whole-brain computational model is built based on empirical functional and structural data between the total brain areas of a given brain parcellation. The local dynamics of each brain area are represented by a Hopf bifurcation equation, which describes the transitions between noise and oscillation. The local bifurcation parameter, a, can shows three different dynamical regimes: noise or stable fixed point ($a < 0$), fluctuating subcritical regime ($a \approx 0$) and oscillatory supercritical regime ($a > 0$). The lower panel shows the representation of the global coupling parameter G. This parameter represents the conductivity of the structural connections across the network. A lower coupling G denotes subcritical behaviour, indicating decreased brain dynamics, whilst a higher coupling G indicates an enhanced transmission of information among brain areas.

3.2.2 PMS simulation

The PMS explained in section 3.1.2 can be simulated using the Hopf model. We used this approach in order to force transitions from a given brain state to another. In brief, the local dynamics of each brain area were described using the normal form of a Hopf bifurcation, and the bifurcation parameters of each oscillator, a, were set on the edge of the bifurcation point. The coupling parameter, G, was optimised to fit the whole-brain model to the PMS. In particular, the centroids of the empirical PMS were used to construct the model based on the probability of the empirical centres. Finally, the empirical and simulated PMS were compared using the symmetrised KL distance as follows:

$$
\begin{aligned}
KL\left(P_{emp}, P_{sim}\right) = 0.5\bigg(\sum_i P_{emp}\left(i\right)\ln\left(\frac{P_{emp}\left(i\right)}{P_{sim}\left(i\right)}\right) + \\
\sum_i P_{sim}\left(i\right)\ln\left(\frac{P_{sim}\left(i\right)}{P_{emp}\left(i\right)}\right)\bigg)
\end{aligned}
\tag{3.9}
$$

where $P_{emp}(i)$ are the empirical and $P_{sim}(i)$ the simulated probabilities of the extracted brain states i. The optimal simulated PMS is obtained where the KL distance between the empirical and simulated PMS is minimal (i.e., the optimal working point of the model). Then, we applied *in silico* perturbations (explained in the next section) in order to force a transition between the PMS of different groups.

3.2.3 *In silico* perturbations

We used the Hopf model to apply two types of perturbations. In *Article 3*, we applied *in silico* perturbations in order to force transitions between brain states of different age groups. In contrast, in *Article 4*, we applied *in silico* perturbations to assess the susceptibility and information encoding capability measures. Such measures allowed us to obtain the brain's reactivity to external perturbations and were assessed in different conscious (rest, meditation) and unconscious (sleep, MCS, UWS) brain states.

Forcing transitions between brain states

The perturbation consists of systematically perturbing each brain area of the model using two different protocols (noise and synchronisation). The perturbations are based on shifting the local bifurcation parameter (a) of the optimised PMS model. In particular, the noise protocol shifts the parameter (a) by applying negative values (i.e., in the range [-0.1: 0] in steps of 0.01), whereas the synchronisation protocol shifts the parameter by applying positive values (i.e., in the range [0: 0.1] in steps of 0.01). Finally, in order to obtain those brain areas promoting the best transition, the KL distance (explained in section 3.2.2) between the target PMS and perturbed PMS is calculated. The best transition is that in which the KL distance is minimal.

Susceptibility and information encoding capability

The susceptibility measure of the whole-brain model defines the brain's sensitivity to react to external stimulations. In contrast to susceptibility, the information capability measure captures how the external stimulations are encoded in whole-brain dynamics. Both measures are estimated on the brain vortex space, R_λ, i.e., evaluated by calculating the modulus of the local Kuramoto order parameter (explained in section 3.1.1).

To measure the **susceptibility**, the Hopf model was perturbed by randomly changing the local bifurcation parameter, a_n, in the range [-0.02: 0]. The sensitivity of the perturbations on the spatiotemporal dynamics was calculated by measuring the modulus of the local Kuramoto order parameter as:

$$D = \left\langle \left\langle \left\langle \tilde{R}_n^{(m)}(t) \right\rangle_t - \left\langle R_n^{(m)}(t) \right\rangle_t \right\rangle_{trials} \right\rangle_s \qquad (3.10)$$

where $\tilde{R}_n^{(m)}(t)$ corresponds to the perturbed case, $R_n^{(m)}(t)$ to the unperturbed case, and $\langle \ \rangle_t$, $\langle \ \rangle_{trials}$, and $\langle \ \rangle_s$ to the average across time, trials, and space, respectively.

The **information capability**, I, was defined as the standard deviation across trials of the difference between the perturbed $\tilde{R}_n^{(m)}(t)$ and

unperturbed $R_n^{(m)}(t)$ mean of the modulus of the local Kuramoto order parameter across time t, averaged across all brain areas n as:

$$I = \langle\langle\langle\left(\langle\tilde{R}_n^{(m)}(t)\rangle_t - \langle R_n^{(m)}(t)\rangle_t\right)^2\rangle_{trials} - \\ \langle\left(\langle\tilde{R}_n^{(m)}(t)\rangle_t - \langle R_n^{(m)}(t)\rangle_t\right)^2\rangle_{trials}\rangle_s$$

(3.11)

where the brackets $\langle\ \rangle_t$, $\langle\ \rangle_{trials}$, and $\langle\ \rangle_s$ denote the averages defined as above.

Chapter 4

RESULTS

4.1   Article 1

Title: Characterizing the Dynamical Complexity Underlying Meditation.

Authors: Escrichs, A., Sanjuán, A., Atasoy, S., López, A., Garrido, C., Camara, E., and Deco, G.

Journal: Frontiers in Systems Neuroscience. 2019

DOI: https://doi.org/10.3389/fnsys.2019.00027

Characterizing the Dynamical Complexity Underlying Meditation

Anira Escrichs [1,2]*, Ana Sanjuán [1], Selen Atasoy [3], Ane López-González [1], César Garrido [4], Estela Càmara [2,5] and Gustavo Deco [1,6]*

[1] Computational Neuroscience Group, Department of Information and Communication Technologies, Center for Brain and Cognition, Universitat Pompeu Fabra, Barcelona, Spain, [2] Cognition and Brain Plasticity Unit, Bellvitge Biomedical Research Institute (IDIBELL), L'Hospitalet de Llobregat, Barcelona, Spain, [3] Department of Psychiatry, University of Oxford, Oxford, United Kingdom, [4] Radiology Unit, Hospital Clínic Barcelona, Barcelona, Spain, [5] Department of Cognition, Development and Educational Psychology, University of Barcelona, Barcelona, Spain, [6] Institució Catalana de la Recerca i Estudis Avançats, Barcelona, Spain

Over the past 2,500 years, contemplative traditions have explored the nature of the mind using meditation. More recently, neuroimaging research on meditation has revealed differences in brain function and structure in meditators. Nevertheless, the underlying neural mechanisms are still unclear. In order to understand how meditation shapes global activity through the brain, we investigated the spatiotemporal dynamics across the whole-brain functional network using the Intrinsic Ignition Framework. Recent neuroimaging studies have demonstrated that different states of consciousness differ in their underlying dynamical complexity, i.e., how the broadness of communication is elicited and distributed through the brain over time and space. In this work, controls and experienced meditators were scanned using functional magnetic resonance imaging (fMRI) during resting-state and meditation (focused attention on breathing). Our results evidenced that the dynamical complexity underlying meditation shows less complexity than during resting-state in the meditator group but not in the control group. Furthermore, we report that during resting-state, the brain activity of experienced meditators showed higher metastability (i.e., a wider dynamical regime over time) than the one observed in the control group. Overall, these results indicate that the meditation state operates in a different dynamical regime compared to the resting-state.

Keywords: ignition, whole-brain, meditation, resting-state, fMRI, integration, dynamical complexity

1. INTRODUCTION

During the last 2,500 years, contemplative traditions have explored the nature of the mind through self-discipline and self-observation. Meditation per se is not a philosophy or a religious practice, but a method of mental training which enables to cultivate a variety of human abilities, ranging from developing a clearer mind and enhancing attention to cultivating altruistic love and compassion toward other beings (Ricard et al., 2014).

In the last decade, MRI studies exploring the neural correlates of meditation have revealed important insights into how this mental training changes brain function and structure (Brewer et al., 2011; Kilpatrick et al., 2011; Froeliger et al., 2012; Hasenkamp et al., 2012; Taylor et al., 2013; Garrison et al., 2014; Marchand, 2014; Tang et al., 2015; Panda et al., 2016; Kyeong et al., 2017; Mooneyham et al., 2017; Marusak et al., 2018). Yet, little is known about how meditation influences the capability to transmit information across the whole-brain functional network.

Recently, it has been proposed that a brain state can be defined by measuring how the broadness of communication is elicited and distributed through the brain over time, i.e., by characterizing its underlying dynamical complexity (Deco et al., 2017). Investigating the propagation of the neural activity by measuring their dynamical implications (Hutchison et al., 2013) across the whole-brain network may help to explain the fundamental principles of the underlying mechanisms of different brain states (Deco et al., 2011, 2015; Sporns, 2013; Allen et al., 2014). Theoretical methods have been successfully applied to characterize different states of consciousness such as wakefulness, sleep, anesthesia or psychedelic states (Tagliazucchi and Laufs, 2014; Tagliazucchi et al., 2014; Atasoy et al., 2017, 2018; Deco et al., 2017; Jobst et al., 2017).

Here, we investigate the brain's macro-scale mechanisms underlying meditation as well as meditation-induced long-term changes in resting-state using the Intrinsic Ignition Framework (Deco and Kringelbach, 2017; Deco et al., 2017). This data-driven method allows to study the spatiotemporal dynamics across the whole-brain functional network by measuring the effect of naturally occurring local activation events on whole-brain integration.

2. METHODS

2.1. Participants

A total of forty participants were recruited for this experiment. Half of the participants were experienced meditators (mean (SD) age = 39.8 (10.29); education years = 13.6; mean (SD) hours meditation experience = 9526.9 (8619.8); 7 females) and were recruited from Vipassana communities of Barcelona. All of them had a minimum of 1,000 h of meditation experience and confirmed that they maintained daily practice (>1 hour/day). The other half were well-matched control participants with no prior meditation experience (mean (SD) age = 39.75 (10.13); education years= 13.8; 7 females). Participants reported no history of neurological disorder, provided written informed consent, and were compensated for their participation. The study was approved by the Ethics Committee of the Bellvitge Hospital in accordance with the Helsinki Declaration on ethical research.

2.2. Resting-State and Meditation fMRI

A total of 450 brain volumes in each condition were analyzed (≈15 min). During rest, participants were asked to look at a fixation cross on the screen, remain as motionless as possible, not to think about anything in particular as well as not to fall asleep. After resting acquisition, all participants were engaged in meditation. Meditators were asked to practice anapanasati meditation (focused attention on breathing). In this type of meditation, subjects try to concentrate all their attention on natural breathing, and when they realize that the mind wanders, they need to recognize it and come back to natural breathing without judgment. Controls were instructed in meditation before being scanned following the instructions as taught by S.N. Goenka (Hart, 1987), who was a Vipassana meditation teacher. Controls confirmed that they understood the procedure after the simulation.

2.3. MRI Data Acquisition

MRI images were acquired on a 3T TIM TRIO scanner (Siemens, Erlangen, Germany) using 32-channel receiver coil. The high-resolution T1-weighted images were acquired with 208 slices in the sagittal plane, repetition time (TR) = 1,970 ms, echo time (TE) = 2.34 ms, TI = 1,050 ms, flip angle = 9°, field of view (FOV) = 256 mm, voxel size $1 \times 1 \times 1$ mm. Resting-state and meditation fMRI were performed by a single shot gradient-echo EPI sequence (TR = 2,000 ms; TE = 29 ms; FOV = 240 mm; in-plane resolution 3 mm; 32 transversal slices with thickness = 4 mm; flip angle = 80°).
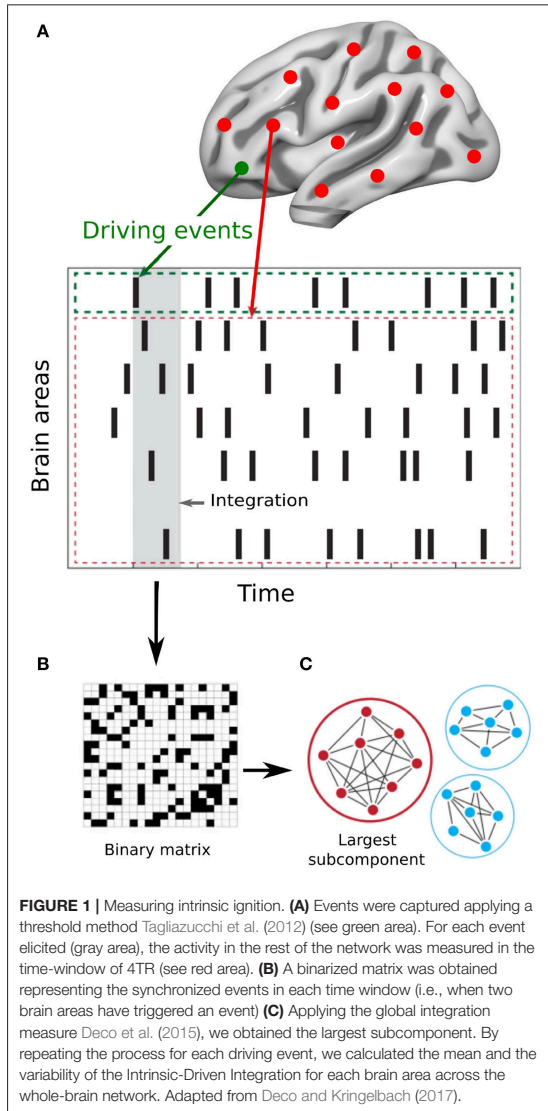
2.4. Preprocessing

Preprocessing was computed using the Data Processing Assistant for Resting-State fMRI (DPARSF) (Chao-Gan and Yu-Feng, 2010). Preprocessing included: manually reorienting T1 and EPI images; discarding the first 10 volumes due to magnetic field inhomogeneities; slice-timing correction; realignment for head motion correction; T1 co-registration to functional image; European regularization segmentation; removal of spurious variance through linear regression: six parameters from the head motion correction, the global mean signal, the white matter signal, and the cerebrospinal fluid signal, CompCor; removal of the linear trend in the time-series; spatial normalization to the Montreal Neurological Institute (MNI); spatial smoothing with 6 mm FWHM Gaussian Kernel; and band-pass temporal filtering (0.01-0.25Hz) (Biswal et al., 1995; Lowe et al., 1998). Finally, we extracted the time-series according to a resting-state atlas of 268 nodes, which ensures the functional homogeneity within each node (Shen et al., 2013).

One meditator was removed due to incidental findings in the MRI session. In addition, 3 controls during meditation and 1 control during rest were excluded due to a head rotation >2 mm or 2°. Moreover, the frame-wise displacement (FD) (Jenkinson et al., 2002) was calculated due to its consideration of voxel-wise differences in motion in its derivation (Yan et al., 2013). Subjects with head motion >2 standard deviations above the group average and movement in more than 25% of time points were excluded from the analysis. FD correction led to the exclusion of 1 control during meditation. Therefore, the final sample of the study included: 19 controls during rest and 16 controls during meditation, 19 meditators during rest and 19 meditators during meditation. After exclusion, no significant differences in terms of age, educational level and gender were observed between groups.

2.5. Intrinsic Ignition Framework

The Intrinsic Ignition Framework (Deco and Kringelbach, 2017) measures the degree of elicited whole-brain integration of spontaneously occurring events across time. **Figure 1** describes the algorithm to obtain the intrinsic integration across events of each brain area. First, the time-series are filtered within the narrowband 0.04–0.07 Hz to avoid artifacts (Glerean et al., 2012). Then, for each brain area, driving events are captured for each timepoint and fixed as a binary signal by transforming the filtered time-series into z-scores, $z_i(t)$. A threshold θ is imposed given by the sum of the mean and the standard deviation of the signal in each brain area, such that the binary sequence $\sigma(t)$ = 1 if $z_i(t) > \theta$ and is crossing the threshold from below and

FIGURE 1 | Measuring intrinsic ignition. **(A)** Events were captured applying a threshold method Tagliazucchi et al. (2012) (see green area). For each event elicited (gray area), the activity in the rest of the network was measured in the time-window of 4TR (see red area). **(B)** A binarized matrix was obtained representing the synchronized events in each time window (i.e., when two brain areas have triggered an event) **(C)** Applying the global integration measure Deco et al. (2015), we obtained the largest subcomponent. By repeating the process for each driving event, we calculated the mean and the variability of the Intrinsic-Driven Integration for each brain area across the whole-brain network. Adapted from Deco and Kringelbach (2017).

σ (t) = 0 otherwise (Tagliazucchi et al., 2012). If a brain area has triggered an event (**Figure 1A** green line) then the integration in the rest of the network is measured within the set time window of 4TR (**Figure 1A** gray time window). A binary matrix is constructed (**Figure 1B**) representing the synchronized events in each timepoint (i.e., when two brain areas have triggered an event). Afterwards, the global integration measure (Deco et al., 2015) is defined as the largest component in the binarized connectivity matrix, given by the length of the connected component considered as an adjacency matrix (**Figure 1C**). Finally, the Intrinsic-Driven Mean Integration (IDMI) is defined

as the averaged integration across events, and the variability as the standard deviation of the Intrinsic-Driven Integration. We would like to remark the similitude of our quantitative measure of ignition and the avalanche framework (see, for example, Beggs and Plenz, 2003).

2.6. Surrogate Analysis

To ensure that the observed results were not obtained by chance, we applied a surrogate data testing method. Specifically, we randomly permuted the original timeseries across time and measured the ignition in each spontaneous event on the shuffled data. After repeating the process 50 times, we tested whether the empirical ignition values were significantly higher than the surrogates' ignition values.

2.7. Statistical Analyses

Here, we compared the IDMI and the variability values for each group (controls and meditators) between conditions (resting and meditation), and we examined if there were differences between groups in the same condition (resting and meditation). Furthermore, we validated our results by comparing the real conditions vs. the randomized ignition data. To do so, we used a Monte-Carlo permutation method. We randomly shuffled the labels between conditions to obtain two new simulated conditions (10,000 permutations). Then, we evaluated how many times the difference between the simulated conditions was higher than the difference between the real conditions. This is, we computed the p-value of the null hypothesis that the two random distributions show higher difference than the real conditions. Additionally, we applied the Bonferroni correction for multiple comparisons.
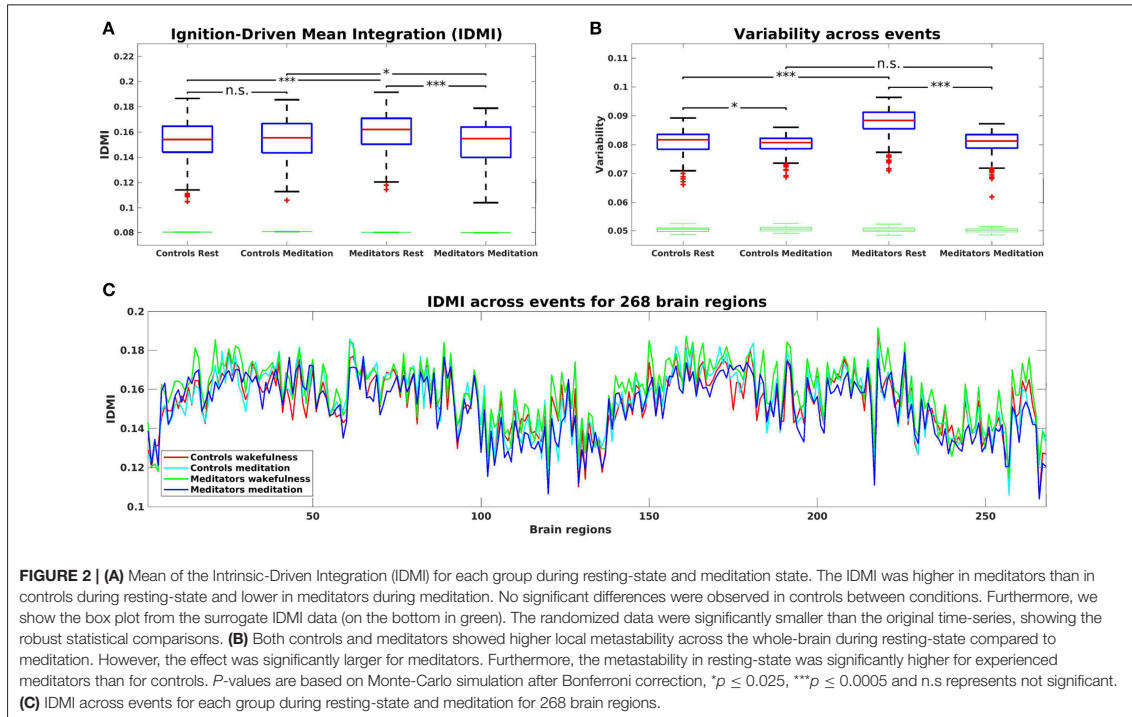
3. RESULTS

3.1. Intrinsic-Driven Mean Integration (IDMI)

Figure 2A shows the IDMI for each group and brain state, while **Figure 2C** shows the IDMI for each group and each brain area. The IDMI captures the spatial diversity as differences in average intrinsic ignition profiles across the different nodes. The brain activity of meditators during resting-state showed the highest values of the IDMI compared to the control group ($p < 0.001$, Monte-Carlo simulations after Bonferroni correction). Furthermore, this value decreased significantly when meditators were engaged in meditation ($p < 0.001$, Monte-Carlo simulations after Bonferroni correction). In contrast, controls did not show any differences between resting-state and meditation conditions.

3.2. Variability of Intrinsic-Driven Integration

Next, we calculated the variability of the Intrinsic-Driven Integration in both states (resting-state and meditation) for each group (controls and meditators). **Figure 2B** shows the variability for each group and brain state. The variability describes the heterogeneity of each brain area, which is closely connected to its local metastability (Deco and Kringelbach, 2017). Thus, it describes how the local activity

FIGURE 2 | (A) Mean of the Intrinsic-Driven Integration (IDMI) for each group during resting-state and meditation state. The IDMI was higher in meditators than in controls during resting-state and lower in meditators during meditation. No significant differences were observed in controls between conditions. Furthermore, we show the box plot from the surrogate IDMI data (on the bottom in green). The randomized data were significantly smaller than the original time-series, showing the robust statistical comparisons. **(B)** Both controls and meditators showed higher local metastability across the whole-brain during resting-state compared to meditation. However, the effect was significantly larger for meditators. Furthermore, the metastability in resting-state was significantly higher for experienced meditators than for controls. *P*-values are based on Monte-Carlo simulation after Bonferroni correction, *$p \leq 0.025$, ***$p \leq 0.0005$ and n.s represents not significant. **(C)** IDMI across events for each group during resting-state and meditation for 268 brain regions.

in each brain area changes across time. High levels of metastability in a node represent a more dynamic function over time, while lower levels represent greater stability. The brain activity of controls and experienced meditators showed higher functional variability (i.e., metastability) in resting-state than in meditation. Nevertheless, the effect was significantly larger for meditators ($p < 0.001$, Monte-Carlo simulations after Bonferroni correction) than for controls ($p = 0.022$, Monte-Carlo simulations after the Bonferroni correction). Furthermore, the metastability in resting-state was significantly larger for experienced meditators than for controls ($p < 0.001$, Monte-Carlo simulations after the Bonferroni correction).

4. DISCUSSION

A growing scientific interest lies in the characterization of the meditation state. Hasenkamp and colleagues (Hasenkamp et al., 2012) captured the interactions between four cognitive phases during meditation, but disregarded the dynamical properties that contain relevant spatiotemporal information. Mooneyham and colleagues applied a dynamical functional connectivity approach dissociating mental states during a meditation scan. The authors reported that after a 6 weeks intervention mindfulness program, subjects spent more time in the state of focused attention and less time in the state of mind-wandering (Mooneyham et al.,

2017). In addition, a study that applied graph theoretical analysis (Jao et al., 2016) characterized the degree of the hierarchical organization during meditation. This study revealed that the nodes that had the highest integration degree during rest had the lowest integration degree during meditation, and vice versa. Our work extends these findings by exploring the brain activity during meditation by characterizing the dynamical complexity in terms of how local information is broadcasted across the whole-brain.

Here, we have characterized the dynamical complexity underlying resting-state and meditation in healthy controls and experienced meditators as evidenced by the level of intrinsic ignition. Specifically, in meditators but not in controls, we observed a significant increase of intrinsic ignition during resting-state compared to meditation (**Figure 2A**). In addition, during resting-state, meditators showed the maximal variability of intrinsic ignition (i.e., metastability) across the whole network, revealing a state of maximum network switching (**Figure 2B**).

Our results showing an increase of intrinsic ignition during rest compared to meditation are consistent with recent studies on information propagation across the brain. Irrmischer and colleagues found a shift from more complex brain dynamics during rest to a state of reduced information propagation during meditation, importantly, only in meditators (Irrmischer et al., 2018). Furthermore, Gard and colleagues demonstrated using

graph theory that yoga and meditation practitioners showed greater network integration than controls during rest (Gard et al., 2014). In addition, the increase of metastability in meditators during resting-state is congruent with the increase of the temporal complexity of oscillations during rest in meditators as observed in the previously mentioned study (Irrmischer et al., 2018). Moreover, studies applying a dynamical functional connectivity approach found that individuals with high trait mindfulness transitioned more frequently between brain states at rest (Lim et al., 2018; Marusak et al., 2018).

To sum up, these results demonstrate that experienced meditators can voluntarily alter their whole-brain dynamics when engaged in a meditative state. Furthermore, expertise in meditation leads to increased ignition and metastability at rest. This means that expert meditators are able to regulate the level of exploration of the dynamical repertoire, restricting it during meditation, and enhancing it during rest.

ETHICS STATEMENT

This study was approved by the Clinical Research Ethics Committee of the Bellvitge University Hospital in accordance with the Declaration of Helsinki. All subjects gave written informed consent to participate in the study.

AUTHOR CONTRIBUTIONS

AE and GD designed the study. EC and CG designed the MRI protocol. AE collected the data and wrote the first version of the manuscript. AE and AS pre-processed the fMRI data. AE, AS, and AL-G performed the analyses. AE, AS, GD, and SA interpreted the results. All authors contributed to manuscript revision, read and approved the submitted version.

FUNDING

ACKNOWLEDGMENTS

REFERENCES

Allen, E. A., Damaraju, E., Plis, S. M., Erhardt, E. B., Eichele, T., and Calhoun, V. D. (2014). Tracking whole-brain connectivity dynamics in the resting state. *Cereb. Cortex* 24, 663–676. doi: 10.1093/cercor/bhs352

Atasoy, S., Deco, G., Kringelbach, M. L., and Pearson, J. (2018). Harmonic brain modes: a unifying framework for linking space and time in brain dynamics. *Neuroscientist* 24, 277–293. doi: 10.1177/1073858417728032

Atasoy, S., Roseman, L., Kaelen, M., Kringelbach, M. L., Deco, G., and Carhart-Harris, R. L. (2017). Connectome-harmonic decomposition of human brain activity reveals dynamical repertoire re-organization under LSD. *Sci. Rep.* 7:17661. doi: 10.1038/s41598-017-17546-0

Beggs, J. M., and Plenz, D. (2003). Neuronal avalanches in neocortical circuits. *J. Neurosci.* 23, 11167–11177. doi: 10.1523/JNEUROSCI.23-35-11167.2003

Biswal, B., Yetkin, F. Z., Haughton, V. M., Hyde, J. S., Zerrin Yetkin, F., Haughton, V. M., et al. (1995). Functional connectivity in the motor cortex of resting human brain using echo-planar MRI. *Magn. Res. Med.* 34, 537–541. doi: 10.1002/mrm.1910340409

Brewer, J. a., Worhunsky, P. D., Gray, J. R., Tang, Y.-Y., Weber, J., and Kober, H. (2011). Meditation experience is associated with differences in default mode network activity and connectivity. *Proc. Natl. Acad. Sci. U.S.A.* 108, 20254–20259. doi: 10.1073/pnas.1112029108

Chao-Gan, Y., and Yu-Feng, Z. (2010). DPARSF: a MATLAB toolbox for "Pipeline" data analysis of resting-state fMRI. *Front. Syst. Neurosci.* 4:13. doi: 10.3389/fnsys.2010.00013

Deco, G., Jirsa, V. K., and McIntosh, A. R. (2011). Emerging concepts for the dynamical organization of resting-state activity in the brain. *Nat. Rev. Neurosci.* 12, 43–56. doi: 10.1038/nrn2961

Deco, G., and Kringelbach, M. L. (2017). Hierarchy of information processing in the brain: a novel 'Intrinsic Ignition' framework. *Neuron* 94, 961–968. doi: 10.1016/j.neuron.2017.03.028

Deco, G., Tagliazucchi, E., Laufs, H., Sanjuán, A., and Kringelbach, M. L. (2017). Novel intrinsic ignition method measuring local- global integration characterizes wakefulness and deep sleep. *eNeuro* 4, 106–17. doi: 10.1523/ENEURO.0106-17.2017

Deco, G., Tononi, G., Boly, M., and Kringelbach, M. L. (2015). Rethinking segregation and integration: contributions of whole-brain modelling. *Nat. Rev. Neurosci.* 16, 430–439. doi: 10.1038/nrn3963

Froeliger, B., Garland, E. L., Kozink, R. V., Modlin, L. A., Chen, N. K., McClernon, F. J., et al. (2012). Meditation-state functional connectivity (msFC): Strengthening of the dorsal attention network and beyond. *Eviden. Based Complement. Alternat. Med.* 2012:680407. doi: 10.1155/2012/680407

Gard, T., Taquet, M., Dixit, R., Hölzel, B. K., de Montjoye, Y.-A., Brach, N., et al. (2014). Fluid intelligence and brain functional organization in aging yoga and meditation practitioners. *Front. Aging Neurosci.* 6:76. doi: 10.3389/fnagi.2014.00076

Garrison, K. A., Scheinost, D., Constable, R. T., and Brewer, J. A. (2014). BOLD signal and functional connectivity associated with loving kindness meditation. *Brain Behav.* 4, 337–347. doi: 10.1002/brb3.219

Glerean, E., Salmi, J., Lahnakoski, J. M., Jääskeläinen, I. P., and Sams, M. (2012). Functional magnetic resonance imaging phase synchronization as a measure of dynamic functional connectivity. *Brain Connect.* 2, 91–101. doi: 10.1089/brain.2011.0068

Hart, W. (1987). *The Art of Living: Vipassana Meditation as Taught by S. N. Goenka*. Onalaska, WA: Pariyatti.

Hasenkamp, W., Wilson-Mendenhall, C. D., Duncan, E., and Barsalou, L. W. (2012). Mind wandering and attention during focused meditation: a fine-grained temporal analysis of fluctuating cognitive states. *NeuroImage* 59, 750–760. doi: 10.1016/j.neuroimage.2011.07.008

Hutchison, R. M., Womelsdorf, T., Allen, E. A., Bandettini, P. A., Calhoun, V. D., Corbetta, M., et al. (2013). Dynamic functional connectivity: Promise, issues, and interpretations. *NeuroImage* 80, 360–378. doi: 10.1016/j.neuroimage.2013.05.079

Irrmischer, M., Houtman, S. J., Mansvelder, H. D., Tremmel, M., Ott, U., and Linkenkaer-Hansen, K. (2018). Controlling the Temporal Structure of Brain Oscillations by Focused Attention Meditation. *Hum. Brain Mapp.* 39, 1825–1838. doi: 10.1002/hbm.23971

Jao, T., Li, C.-W., Vértes, P. E., Wu, C. W., Achard, S., Hsieh, C.-H., et al. (2016). Large-scale functional brain network reorganization during taoist meditation. *Brain Connect.* 6, 9–24. doi: 10.1089/brain.2014.0318

Jenkinson, M., Bannister, P., Brady, M., and Smith, S. (2002). Improved optimization for the robust and accurate linear registration and motion correction of brain images. *NeuroImage* 17, 825–41. doi: 10.1006/nimg.2002.1132

Jobst, B. M., Hindriks, R., Laufs, H., Tagliazucchi, E., Hahn, G., Ponce-Alvarez, A., et al. (2017). Increased stability and breakdown of brain effective connectivity during slow-wave sleep: mechanistic insights from whole-brain computational modelling. *Sci. Rep.* 7:4634. doi: 10.1038/s41598-017-04522-x

Kilpatrick, L. A., Suyenobu, B. Y., Smith, S. R., Bueller, J. A., Goodman, T., Creswell, J. D., et al. (2011). Impact of mindfulness-based stress reduction training on intrinsic brain connectivity. *NeuroImage* 56, 290–298. doi: 10.1016/j.neuroimage.2011.02.034

Kyeong, S., Kim, J., Kim, D. J., Kim, H. E., and Kim, J.-J. (2017). Effects of gratitude meditation on neural network functional connectivity and brain-heart coupling. *Sci. Rep.* 7:5058. doi: 10.1038/s41598-017-05520-9

Lim, J., Teng, J., Patanaik, A., Tandi, J., and Massar, S. A. (2018). Dynamic functional connectivity markers of objective trait mindfulness. *NeuroImage* 176, 193–202. doi: 10.1016/j.neuroimage.2018.04.056

Lowe, M., Mock, B., and Sorenson, J. (1998). Functional connectivity in single and multislice echoplanar imaging using resting-state fluctuations. *NeuroImage* 7, 119–132.

Marchand, W. R. (2014). Neural mechanisms of mindfulness and meditation: Evidence from neuroimaging studies. *World J. Radiol.* 6, 471–479. doi: 10.4329/wjr.v6.i7.471

Marusak, H. A., Elrahal, F., Peters, C. A., Kundu, P., Lombardo, M. V., Calhoun, V. D., et al. (2018). Mindfulness and dynamic functional neural connectivity in children and adolescents. *Behav. Brain Res.* 336, 211–218. doi: 10.1016/j.bbr.2017.09.010

Mooneyham, B. W., Mrazek, M. D., Mrazek, A. J., Mrazek, K. L., Phillips, D. T., and Schooler, J. W. (2017). States of mind: characterizing the neural bases of focus and mind-wandering through dynamic functional connectivity. *J. Cogn. Neurosci.* 29, 495–506. doi: 10.1162/jocn-a-01066

Panda, R., Bharath, R. D., Upadhyay, N., Mangalore, S., Chennu, S., and Rao, S. L. (2016). Temporal dynamics of the default mode network characterize meditation-induced alterations in consciousness. *Front. Hum. Neurosci.* 10:372. doi: 10.3389/fnhum.2016.00372

Ricard, M., Lutz, A., and Davidson, R. J. (2014). Mind of the meditator. *Sci. Am.* 311, 38–45. doi: 10.1038/scientificamerican1114-38

Shen, X., Tokoglu, F., Papademetris, X., and Constable, R. (2013). Groupwise whole-brain parcellation from resting-state fMRI data for network node identification. *NeuroImage* 82, 403–415. doi: 10.1016/j.neuroimage.2013.05.081

Sporns, O. (2013). Network attributes for segregation and integration in the human brain. *Curr. Opin. Neurobiol.* 23, 162–171. doi: 10.1016/j.conb.2012.11.015

Tagliazucchi, E., Balenzuela, P., Fraiman, D., and Chialvo, D. R. (2012). Criticality in large-scale brain fMRI dynamics unveiled by a novel point process analysis. *Front. Physiol.* 3:15. doi: 10.3389/fphys.2012.00015

Tagliazucchi, E., Carhart-Harris, R., Leech, R., Nutt, D., and Chialvo, D. R. (2014). Enhanced repertoire of brain dynamical states during the psychedelic experience. *Hum. Brain Mapp.* 35, 5442–5456. doi: 10.1002/hbm.22562

Tagliazucchi, E., and Laufs, H. (2014). Decoding wakefulness levels from typical fMRI resting-state data reveals reliable drifts between wakefulness and sleep. *Neuron* 82, 695–708. doi: 10.1016/j.neuron.2014.03.020

Tang, Y.-Y., Hölzel, B. K., and Posner, M. I. (2015). The neuroscience of mindfulness meditation. *Nat. Rev. Neurosci.* 16, 213–225. doi: 10.1038/nrn3916

Taylor, V. A., Daneault, V., Grant, J., Scavone, G., Breton, E., Roffe-vidal, S., et al. (2013). Impact of meditation training on the default mode network during a restful state. *Soc. Cogn. Affect. Neurosci.* 8, 4–14. doi: 10.1093/scan/nsr087

Yan, C.-G., Craddock, R. C., Zuo, X.-N., Zang, Y.-F., and Milham, M. P. (2013). Standardizing the intrinsic brain: towards robust measurement of inter-individual variation in 1000 functional connectomes. *NeuroImage* 80, 246–62. doi: 10.1016/j.neuroimage.2013.04.081

4.2 Article 2

Title: Whole-brain dynamics in aging: disruptions in functional connectivity and the role of the rich club.

Authors: Escrichs, A., Biarnes, C., Garre-Olmo, J., Fernández-Real, J. M., Ramos, R., Pamplona, R., Brugada, R., Serena, J., Ramio-Torrenta, L., Coll-De-Tuerom G., Gallart, L., Barretina, J., Vilanova, J.C., Mayneris-Perxachs, J., Essig, M., Figley, C.R., Pedraza, S., Puig, J., and Deco, G.

OXFORD

ORIGINAL ARTICLE

Whole-Brain Dynamics in Aging: Disruptions in Functional Connectivity and the Role of the Rich Club

Anira Escrichs[1], Carles Biarnes[2,3], Josep Garre-Olmo[3,4,5], José Manuel Fernández-Real[3,4,6], Rafel Ramos[3,4,7,8], Reinald Pamplona[9], Ramon Brugada[3,4,10], Joaquin Serena[3,4,11], Lluís Ramió-Torrentà[3,4,11], Gabriel Coll-De-Tuero[4,7,12], Luís Gallart[13], Jordi Barretina[3], Joan C. Vilanova[2,3,4], Jordi Mayneris-Perxachs[3,6], Marco Essig[14], Chase R. Figley[14], Salvador Pedraza[2,3,4], Josep Puig[2,3,4] and Gustavo Deco[1,15,16,17]

[1]Computational Neuroscience Group, Center for Brain and Cognition, Department of Information and Communication Technologies, Universitat Pompeu Fabra, Barcelona, Catalonia, Spain, [2]Department of Radiology (IDI), Hospital Universitari de Girona Dr Josep Trueta, Girona, Spain, [3]Girona Biomedical Research Institute (IDIBGI), Hospital Universitari de Girona Dr Josep Trueta, Girona, Spain, [4]Department of Medical Sciences, School of Medicine, University of Girona, Girona, Spain, [5]Institut d'Assistència Sanitària, Salt (Girona), Spain, [6]Department of Diabetes, Endocrinology and Nutrition, IDIBGI, Hospital Universitari de Girona Dr Josep Trueta, and CIBER Fisiopatología de la Obesidad y Nutrición (CIBERobn), Girona, Spain, [7]Vascular Health Research Group of Girona (ISV-Girona), Institut Universitari d'Investigació en Atenció Primària Jordi Gol (IDIAP Jordi Gol), Girona, Spain, [8]Primary Care Services, Catalan Institute of Health (ICS), Girona, Spain, [9]Department of Experimental Medicine, Faculty of Medicine, University of Lleida-IRBLleida, Lleida, Spain, [10]Cardiovascular Genetics Center, IDIBGI, CIBER-CV, Girona, Spain, [11]Department of Neurology, Hospital Universitari de Girona Dr Josep Trueta, Girona, Spain, [12]CIBER of Epidemiology and Public Health (CIBERESP), Madrid, Spain, [13]Biobanc, Girona Biomedical Research Institute (IDIBGI), Girona, Spain, [14]Department of Radiology, University of Manitoba, Winnipeg, Canada, [15]Institucio Catalana de la Recerca i Estudis Avancats (ICREA), Barcelona, Catalonia, Spain, [16]Department of Neuropsychology, Max Planck Institute for human Cognitive and Brain Sciences, Leipzig, Germany and [17]Turner Institute for Brain and Mental Health, Monash University, Melbourne, Victoria, Australia

Address correspondence to Gustavo Deco, Computational Neuroscience Group, Center for Brain and Cognition, Department of Information and Communication Technologies, Universitat Pompeu Fabra, Barcelona, Spain. Email: gustavo.deco@upf.edu; Josep Puig: Girona Biomedical Research Institute (IDIBGI), Hospital Universitari de Girona Dr Josep Trueta, Girona, Spain. Email: jpuigalcantara@idibgi.org.

Abstract

Normal aging causes disruptions in the brain that can lead to cognitive decline. Resting-state functional magnetic resonance imaging studies have found significant age-related alterations in functional connectivity across various networks. Nevertheless, most of the studies have focused mainly on static functional connectivity. Studying the dynamics of resting-state brain activity across the whole-brain functional network can provide a better characterization of

age-related changes. Here, we employed two data-driven whole-brain approaches based on the phase synchronization of blood-oxygen-level-dependent signals to analyze resting-state fMRI data from 620 subjects divided into two groups (middle-age group ($n = 310$); age range, 50–64 years versus older group ($n = 310$); age range, 65–91 years). Applying the intrinsic-ignition framework to assess the effect of spontaneous local activation events on local–global integration, we found that the older group showed higher intrinsic ignition across the whole-brain functional network, but lower metastability. Using Leading Eigenvector Dynamics Analysis, we found that the older group showed reduced ability to access a metastable substate that closely overlaps with the so-called rich club. These findings suggest that functional whole-brain dynamics are altered in aging, probably due to a deficiency in a metastable substate that is key for efficient global communication in the brain.

Key words: aging, metastability, rich-club, resting-state fMRI, whole-brain dynamics

Introduction

Normal aging is associated with changes in the structure and function of the brain that could lead to cognitive decline and worse quality of life (Li et al. 2015). Studying the mechanisms of brain aging may identify interventions to prevent or slow age-related deterioration and improve our understanding of the mechanisms involved in neurodegenerative diseases (Ferreira and Busatto 2013). In recent years, noninvasive resting-state functional magnetic resonance imaging (fMRI) paradigms from spontaneous blood-oxygen-level-dependent (BOLD) signals have proven useful in studying age-related changes in brain function (Ystad et al. 2011). Resting-state fMRI shows coherent spontaneous low-frequency fluctuations across brain regions and the organization of these regions into different functional networks (Zuo et al. 2010). Studies of functional connectivity have suggested age-related alterations in different resting-state networks (Wang et al. 2010; Ferreira and Busatto 2013; Grady et al. 2016), even in cognitively preserved older adults (Damoiseaux et al. 2008; Onoda et al. 2012). Other studies (Li et al. 2015; Grady et al. 2016; Fjell et al. 2017) have suggested that overactivation in functional connectivity across resting-state networks may be related to compensatory mechanisms.

Although functional connectivity studies have demonstrated reliable age-related changes, it remains unclear how brain networks cooperate to handle aging-associated declines, especially considering the effects of averaging on measurements of functional connectivity during rest (Hutchison et al. 2013). In this line, growing evidence indicates that functional connectivity among brain networks is not static over time; rather, different brain regions connect and disconnect from one another in highly complex temporal dynamics (Deco et al. 2011; Hutchison et al. 2013; Sporns 2013; Zalesky et al. 2014; Ponce-Alvarez et al. 2015). In other words, even in the resting state, brain networks fluctuate in response to different contexts or stimuli. Capturing statistical properties of fMRI data beyond classical static functional connectivity can facilitate the interpretation of brain functioning during the resting scan from new perspectives. This approach assumes that mental operations arise from neural communication involving coherent and flexible oscillatory activity between functional groups of neurons (Hutchison et al. 2013; Deco and Kringelbach 2016). The term metastability (Deco and Kringelbach 2016) refers to the temporal variability of the functional connectivity that arises from the underlying structural connectivity (the human connectome) (Sporns et al. 2005). Optimal brain function is thought to occur within a range of metastable patterns that reflects a balance between the synchronization and adaptive reconfiguration of the functional

connections among the different regions that make up the structural network (Cabral et al. 2011).

Dynamic (time-varying) functional connectivity has been explored across the lifespan (Nomi et al. 2017), across different states of consciousness (Deco et al. 2017b; Escrichs et al. 2019; Lord et al. 2019), in patients with brain disorders (Puig et al. 2018), and during healthy aging (Tian et al. 2018; Nobukawa et al. 2019). One study that evaluated resting-state fMRI data from 250 subjects to examine patterns of resting-state functional connectivity over time found that dynamic connectivity patterns are consistent across groups (Abrol et al. 2016). Another study (Yin et al. 2016) found that age-related changes in the functional flexibility of the brain differ in different regions of the cerebral cortex. A recent study in 188 cognitively healthy elderly individuals (Lou et al. 2019) found that frequency-specific brain network diversity decreased with increasing age at both the whole-brain and regional levels. Thus, exploring dynamic functional connectivity promises to enrich our knowledge of the functional organization of the brain, but little is known about changes in dynamic functional connectivity during aging.

In this work, we explored age-related changes in dynamic functional connectivity across the whole-brain network, applying two recently developed data-driven methods based on the phase synchronization of resting-state fMRI BOLD signals to a large dataset from healthy human adults. We studied two aspects of whole-brain functional connectivity in middle-aged subjects versus older subjects: 1) the effects of spontaneously occurring local activation events on local–global integration through the intrinsic-ignition framework (Deco and Kringelbach 2017; Deco et al. 2017b) and 2) recurrent dynamic functional connectivity patterns across time (here, referred to as metastable substates), their duration, and their probability of occurrence through Leading Eigenvector Dynamics Analysis (LEiDA) (Cabral et al. 2017).

Materials and Methods

Subjects

The study population was drawn from the 1030 subjects aged ≥50 years who participated in the population-based Aging Imageomics Study (Puig et al. 2020) from whom data were collected between November 2018 and June 2019. We excluded subjects for whom the full brain imaging dataset was unavailable: those who did not undergo the complete brain imaging protocol including fMRI ($n = 23$), those with MRI acquisition errors ($n = 192$), and those with uncorrectable motion artifacts ($n = 92$; see the Preprocessing section below). Thus, the inclusion criteria were met

Table 1 Demographic and clinical characteristics

	Overall sample (n=620)	Middle-age group (<65 years) (n=310)	Older group (≥ 65 years) (n=310)	p value
Sex (female), n (%)	307 (49.5)	169 (54.5)	138 (44.5)	0.016[a]
Age, mean (SD)	65.9 (7.2)	60.2 (3.7)	71.8 (4.5)	NA
Age groups, n (%)				NA
50–64	310			
65–91	310			
Education level*, n (%)				<0.001[a]
No schooling	18 (2.9)	2 (0.7)	16 (5.2)	
Primary (ISCED 1)	324 (52.8)	133 (43.3)	191 (62.2)	
Secondary (ISCED 2)	90 (14.7)	55 (17.9)	35 (11.4)	
Professional (ISCED 3–4)	107 (17.4)	67 (21.8)	40 (13.0)	
University (ISCED 5–8)	75 (12.2)	50 (16.3)	25 (8.1)	
Body mass index**, n (%)				<0.001[a]
<18.5 kg/m^2	5 (0.8)	5 (1.6)	0 (0.0)	
18.5 kg/m^2–24.9 kg/m^2	156 (25.2)	96 (31.2)	60 (19.4)	
25.0 kg/m^2–29.9 kg/m^2	279 (45.1)	118 (38.3)	161 (51.9)	
≥ 30 kg/m^2	178 (28.8)	89 (28.9)	89 (28.7)	
Physical activity groups (IPAQ), n (%)[†]				0.129[a]
High	303 (51.5)	136 (47.2)	167 (55.7)	
Moderate	248 (42.2)	130 (45.1)	118 (39.3)	
Low	37 (6.3)	22 (7.6)	15 (5.0)	
Weight (kg), mean (SD)	75.6 (14.1)	75.1 (15.5)	76.1 (12.5)	0.338[b]
Height (cm), mean (SD)	164 (9.0)	164 (9.1)	163 (9.1)	0.198[b]
Systolic arterial pressure (mmHg), mean (SD)	138.8 (19.4)	135.1 (19.2)	142.6 (18.8)	<0.001[b]
Diastolic arterial pressure (mmHg), mean (SD)	84.1 (10.6)	85.0 (10.1)	83.1 (11.0)	0.034[b]
Hypertension, n (%)[#]	289 (46.9)	120 (38.8)	169 (55.0)	<0.001[a]
Diabetes mellitus, n (%)[#]	139 (22.5)	47 (15.2)	92 (29.9)	<0.001[a]
Dyslipidemia, n (%)[#]	181 (29.4)	79 (25.5)	102 (33.3)	0.039[a]

Notes: *6 missing values
**2 missing values
[†]32 missing values
[#]4 missing values, IPAQ: International Physical Activity Questionnaire
[a]Chi-square test
[b]Student's t-test

by 723 subjects [310 aged < 65 years (middle-aged group) and 413 aged ≥65 years (older group)]. We established the cutoff age between groups based on the definition of "elderly" people as those aged ≥65 years (WHO 2016; United Nations 2020). To homogenize the size of the samples in the two groups, we randomly selected 310 subjects from those aged ≥65 years. The middle-aged group comprised 310 subjects aged < 65 years (mean age, 60.2 ± 3.7 y), and the older group comprised 310 subjects aged ≥65 years (mean age, 71.8 ± 4.5 y). Table 1 reports details about subjects' social and physical status. The ethics committee at the Dr Josep Trueta University Hospital supervising the study approved the study protocol, and all subjects provided written informed consent.

Image Acquisition

Images were acquired on a mobile 1.5 T scanner (Vantage Elan, Toshiba Medical Systems at the beginning of the study; now Canon Medical Systems) with an 8-channel phased-array head coil with foam padding to restrict head motion and noise-canceling headphones. Brain MRI studies included the acquisition of a high-resolution axial T1-weighted sequence (number of slices = 112; repetition time (TR) = 8 ms; echo time (TE) = 4.5 ms; flip angle = 15°; field of view (FOV) = 235 × 235 mm; and voxel size = 1.3 × 1.3 × 2.5 mm) for structural imaging and

a gradient echo-planar imaging (EPI) sequence (TR = 2500 ms; TE = 40 ms; flip angle = 83°; FOV = 230 × 230 mm; and voxel size = 3.5 × 3.5 × 5 mm without gap) with 122 continuous functional volumes acquired axially for 5 min for resting-state fMRI. Subjects were asked to relax, remain as motionless as possible, remain awake, and keep their eyes closed to minimize stimuli, including visuals (Patriat et al. 2013; Agcaoglu et al. 2019).

Image Preprocessing

T1-weighted and EPI images were automatically oriented using Conn (Whitfield-Gabrieli and Nieto-Castanon 2012). For preprocessing, we used the Data Processing Assistant for Resting-State fMRI (DPARSF) toolbox [(Chao-Gan and Yu-Feng 2010), www.rfmri.org/DPARSF], based on Statistical Parametric Mapping (SPM12) (http://www.fil.ion.ucl.ac.uk/spm). Preprocessing included: 1) discarding the first 5 volumes from each scan to allow for signal stabilization; 2) slice-timing correction; 3) realignment for head motion correction across different volumes; 4) co-registration of the functional image to the T1-weighted image; 5) normalization by using T1 image unified segmentation; 6) nuisance covariates regression: six parameters from the head motion correction, the white matter signal, and the cerebrospinal fluid signal using CompCor
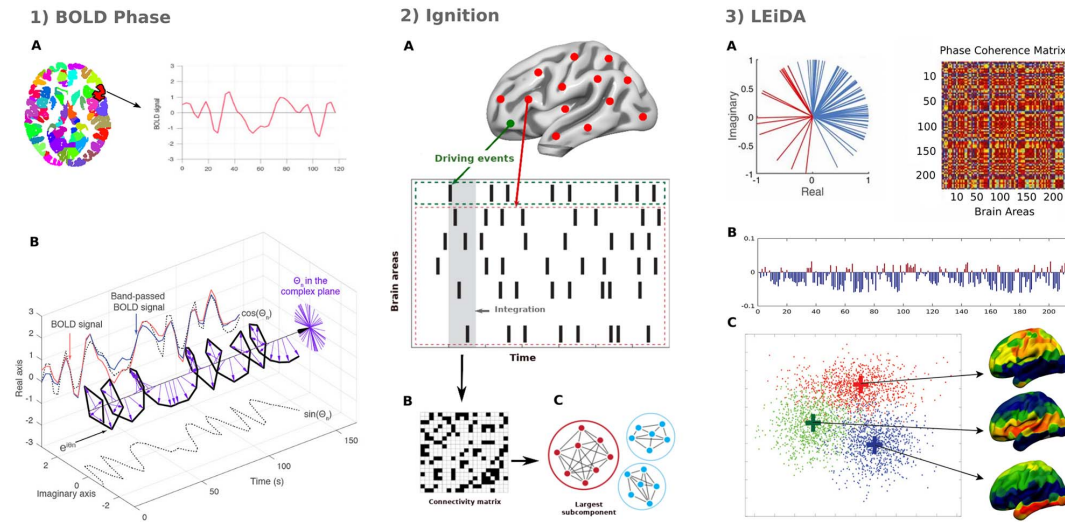
Figure 1. Methods. We applied two data-driven whole-brain methods based on phase synchronization of the BOLD signals. (1) For each of the 214 brain areas, we extracted the BOLD time series and computed the phase space of the BOLD signal. (1A) Specifically, we obtained the time series for each brain area using a resting-state atlas (Shen et al. 2013). (1B) Then, we measured the phase space of the BOLD signal by using the Hilbert transform for each brain area. The BOLD signal (red) was band-pass filtered between 0.04 and 0.07 Hz (blue) and converted with the Hilbert transform into an analytical signal represented by its instantaneous amplitude $A(t)$ and its phase φ (with real and imaginary components). The phase dynamics can be represented in the complex plane as $e^{i\varphi}$ (black bold line), the real part as $\cos\varphi$ (black dotted line), and the imaginary part as $\sin\varphi$ (black dotted line). The purple arrows represent the Hilbert phases at each TR. (2) Measuring intrinsic ignition. (2A) Events were captured by applying a threshold method (Tagliazucchi et al. 2012) (see green area). For each event evoked, the activity in the rest of the network (see red stippled area) was measured in the 4TR time window (gray area). (2B) A binarized phase lock matrix was obtained from the time window. (2C) From this phase lock matrix, we obtained the integration by calculating the largest subcomponent (i.e., by applying the global integration measure (Deco et al. 2017b, 2015)). Repeating the process for each driving event, we obtained the ignition and metastability of the intrinsic-driven integration for each brain area across the whole-brain network. (3) Finally, we applied the LEiDA to characterize differences between groups in dynamic functional connectivity patterns or metastable substates. (3A) The left panel shows the BOLD phases in all 214 brain areas represented in the complex plane. The right panel shows the phase coherence matrix between each pair of brain areas. (3B) The leading eigenvector V1(t) from this matrix was extracted. (3C) We applied a k-means clustering algorithm to detect the metastable substates from all the leading eigenvectors, across timepoints, number of subjects, and groups. Figure adapted from (Deco and Kringelbach 2017; Escrichs et al. 2019; Deco et al. 2019a).

(Behzad et al. 2007); 7) removal of the linear trend in the time series; 8) spatial normalization to the Montreal Neurological Institute standard space; 9) spatial smoothing with 6-mm full width at half-maximum Gaussian kernel; and 10) band-pass temporal filtering (0.01–0.20 Hz)**.** Then, the time series were extracted using a resting-state atlas of 214 brain areas (without the cerebellum), which ensures the functional homogeneity within each brain subunit. The atlas allows parcellating the whole-brain functional network (Shen et al. 2013), as well as parcellating the brain across eight large-scale brain networks (Finn et al. 2015).

We excluded a total of 92 subjects (39 subjects <65 years and 53 subjects ≥65 years) for head rotation or movement (67 for head rotation 2 mm or 2° and 25 for frame-wise displacement (Jenkinson et al. 2002; Yan et al. 2013), defined as head motion >2 standard deviations above the group average in >25% timepoints).

Phase Synchronization

We computed the instantaneous phase of the BOLD signals between each pair of brain areas at each timepoint. First, to avoid artifacts, we band-pass filtered the BOLD time series within the narrowband (0.04–0.07 Hz) (Glerean et al. 2012) (Fig. 1.1A). Then, we obtained the analytic signal, $a(t)$, of the filtered time series of each brain area by computing the Hilbert transform (HT).

The analytic signal represents a narrowband signal in the time domain as a rotating vector, calculated as $\{a(t) = A(t).\cos(\varphi(t))\}$, where $A(t)$ is the time-varying amplitude with carrier frequency expressed by the time-varying phase $\varphi(t)$. The amplitude is determined by the modulus and the phase is determined by the argument of the complex signal, $z(t)$, $\{z(t) = a(t)+i.HT\,[a(t)]\}$, where $HT\,[a(t)]$ is the Hilbert transform of the analytical signal, $a(t)$, and i is the imaginary unit (Glerean et al. 2012; Ponce-Alvarez et al. 2015; Deco et al. 2019a). Figure 1.1B shows the representation of the Hilbert BOLD phase for a brain area over time in the complex plane.

Intrinsic-Ignition Framework

To measure the effect of spontaneous local activation events on whole-brain integration, we applied the intrinsic-ignition framework (Deco and Kringelbach 2017) using the phase space of the signals. This framework has been successfully applied in different resting-state fMRI studies (Deco et al. 2017b; Escrichs et al. 2019; Padilla et al. 2019; Alonso-Martínez et al. 2020). This approach characterizes the spatiotemporal propagation of information by measuring the degree of integration among spontaneous occurring events across the brain over time. Figure 1.2 represents the algorithm used to obtain the ignition value of each brain area evoked by an event within a set time window. Specifically, we averaged across the events the

integration evoked at each time t with the time window set at 4TR. A binary event is defined by transforming the time series into z-scores, $z_i(t)$, and fixing a threshold, θ, given by the sum of the mean and the standard deviation of the signal in each brain area, such that the binary sequence $\sigma(t) = 1$ if $z_i(t) > \theta$ and crosses the threshold from below, and $\sigma(t) = 0$ otherwise (Fig. 1.2A) (Tagliazucchi et al. 2012; Deco et al. 2017b). Different threshold choices show robustness in a reasonable range because the binarization procedure derives from the "Poincaré section" (a method that makes it possible to reduce the dimensionality of a dynamic system) (Tagliazucchi et al. 2012; Deco et al. 2019b). First, we obtained the instantaneous phase in all brain areas as explained in the Phase Synchronization section above and Figure 1.1. Then, we calculated the phase lock matrix $P_{jk}(t)$, which describes the state of pair-wise phase synchronization at time t between regions j and k as:

$$P_{jk}(t) = e^{-3|\varphi_j(t) - \varphi_k(t)|} \quad (1)$$

where $\varphi_j(t)$ and $\varphi_k(t)$ correspond to the obtained phase of the brain areas j and k at time t. Then, the integration is defined by measuring the length of largest connected component in the binarized symmetric phase lock matrix $P_{jk}(t)$ (Fig. 1.2B). That is, given the fixed threshold θ, the matrix is binarized such that (0 if $|P_{jk}| < \theta$, 1 otherwise), and the integration value is computed as the length of the connected component considered as an adjacent graph (i.e., the largest subcomponent) (Fig. 1.2C). The largest subcomponent represents the broadness of communication across the network for each driving event (Deco et al. 2015). Finally, repeating the process for each event in each brain area, the framework returns the mean integration and the standard deviation across the network. The mean integration is called ignition and it represents the spatial diversity; the standard deviation is called metastability, and it represents the variability over time for each brain area. Greater metastability in a brain area means that its activity changes more frequently across time within the network. The framework was computed across the whole-brain functional network (214 brain areas), as well as independently for eight resting-state networks: the frontoparietal, medial frontal, default-mode, subcortical, motor, visual I, visual II, and visual-association networks (Finn et al. 2015).

Leading Eigenvector Dynamics Analysis

To identify differences between groups in recurrent patterns of time-varying connectivity (dynamic functional connectivity) or 'metastable-substates' across all subjects, we used Leading Eigenvector Dynamics Analysis (LEiDA) (Cabral et al. 2017), a k-means clustering analysis based on the phase synchronization of BOLD signals. First, we computed a dynamic phase coherence connectivity matrix (Deco and Kringelbach 2016) with size $N \times N \times T$, where $N = 214$ (total number of brain areas), and $T = 117$ (total number of timepoints), using the Hilbert transform as explained above in the Phase Synchronization section. Then, we calculated the BOLD phase coherence matrix (Fig. 1.3A) at time t between each pair of brain areas n and p by computing the cosine of the phase difference as:

$$dFC(n, p, t) = \cos(\theta(n, t) - \theta(p, t)) \quad (2)$$

Given that the HT expresses any signal in the polar coordinate system (i.e., $a_{(t)} = A(t) \cdot \cos(\varphi_{(t)})$), when the cosine function is applied, two brain areas n and p with similar angles at a given time t will show a phase coherence near 1 (i.e., $\cos(0°) = 1$), whereas two brain areas that are orthogonal at a given time t will show a phase coherence near zero (i.e., $\cos(90°) = 0$) (Cabral et al. 2017; Deco et al. 2019b). Second, to characterize the dynamic functional connectivity patterns across all subjects and timepoints, we obtained a leading eigenvector $V_1(t)$ for each $dFC(t)$ at time t by capturing the dominant functional connectivity pattern rather than the whole set of matrices. This approach allows reducing the dimensionality of the data considerably because it only considers a single $V_1(t)$ for each dynamic functional connectivity matrix. The $V_1(t)$ is an $N \times 1$ vector capturing the principal orientation of the BOLD phase (showing positive or negative values) for each of the 214 brain areas (Fig. 1.3B). Finally, we applied a k-means clustering algorithm using a range from $k = 2$ to 7 clusters to detect metastable substates or dynamic functional connectivity states from all the leading eigenvectors $V_1(t)$ across timepoints, subjects, and groups: 117 timepoints $\times$ 310 subjects $\times$ 2 groups = 72,540 $V_1(t)$. We obtained k cluster centroids, each one as an $N \times 1$ vector, which represent recurrent metastable substates across all subjects. The clustering configuration that best represented the resting-state data of all 620 subjects and distinguished between the two groups was detected at $k = 3$ (Fig. 1.3C). We rendered the resulting cluster centroids onto a surface cortex using Surf Ice (https://www.nitrc.org/projects/surfice/). A complete description of the method can be found in Cabral et al. (2017).

Statistical Analysis

Statistical analyses were done with software MATLAB version R2017a (MathWorks, Natick, MA, USA). We applied a Monte Carlo permutation method to test the results of the Intrinsic-Ignition Framework (ignition and metastability) and to test the results of the LEiDA method (probability of occurrence and duration of each metastable substate). More specifically, we randomly shuffled the labels for each pair of conditions to be tested and created two new simulated conditions (10,000 iterations). Then, we measured how many times the difference between the new simulated conditions was greater than the difference between the real conditions; in other words, we calculated the P-value of the null hypothesis that the two random distributions show a greater difference than the real conditions. Furthermore, we applied the False Discovery Rate (FDR) method (Hochberg and Benjamini 1990) to correct for multiple comparisons when we tested the differences between groups in the eight resting-state networks and the three metastable substates. Finally, for participants' demographic and health characteristics, qualitative variables are expressed as absolute and relative frequencies and quantitative variables as measures of central tendency and dispersion. For bivariate comparisons of these variables between age groups, we used the chi-square test and Student's t-test.

Results

Intrinsic Ignition

We computed the intrinsic-ignition framework across the whole-brain functional network and found that the mean ignition was higher in the older group than in the middle-age group ($P < 0.001$) (Fig. 2a). In the middle-age group, the regions with the highest intrinsic ignition belong to the visual networks (right middle occipital gyrus, lingual gyri, right middle temporal
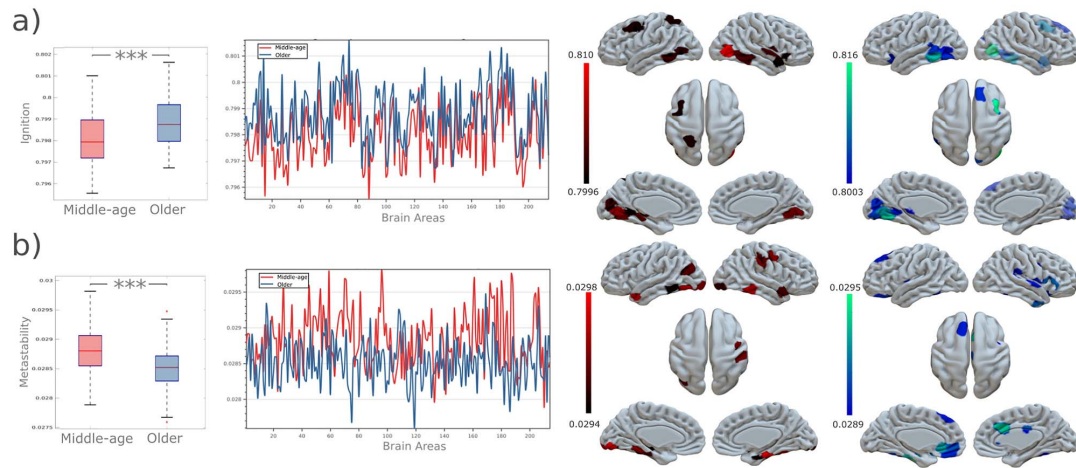
Figure 2. Intrinsic ignition framework. (*a*) Ignition measure. The boxplot shows the mean integration (ignition) for each group (middle-age group and older group). The ignition was higher in the older group (in blue) than in the middle-age group (in red) ($P < 0.001$). The second graph shows ignition plotted across brain areas. Rendered brains represent the 20 regions with the highest ignition for each group (middle age in red and older group in blue). (*b*) Metastability measure. By contrast, the middle-age group showed higher metastability across the whole-brain compared to the older group ($P < 0.001$). P-values are based on Monte–Carlo permutation tests, ∗∗∗ represents $P < 0.001$.

gyrus, fusiform gyri, left calcarine fissure and surrounding cortex), subcortical network (right insula, left hippocampus and parahippocampal gyrus), frontoparietal network (inferior temporal gyri), motor network (superior temporal gyri), and medial-frontal network (left precentral gyrus, left middle frontal gyrus). By contrast, in the older group, the regions showing the highest intrinsic ignition areas belong to the visual networks (right middle occipital gyrus, right middle temporal gyrus, left fusiform gyrus, lingual gyri, calcarine fissure and surrounding cortex in both hemispheres, right cuneus), medial frontal network (left inferior frontal gyrus, middle temporal gyri, superior frontal gyri), frontoparietal network (inferior temporal gyri, right middle frontal gyrus), and subcortical (left insula, left thalamus). Table 2 shows the 20 brain areas with the highest intrinsic-ignition capability for each group.

Metastability was lower in the older group than in the middle-age group ($P < 0.001$) (Fig. 2*b*). In the middle-age group, the brain areas with the highest metastability belong mainly to the default-mode network (parahippocampal gyri, fusiform gyri, left middle occipital gyrus), visual networks (inferior temporal gyri, inferior occipital gyri, left lingual gyrus, fusiform gyri), medial frontal network (left middle temporal gyrus), frontoparietal network (inferior temporal gyrus in both hemispheres), motor network (right precentral gyrus, right postcentral gyrus), and subcortical (left hippocampus). By contrast, in the older group, the brain areas with the highest metastability belong mainly to the motor network (inferior temporal gyri, left insula, bilateral Rolandic opercula, right superior temporal gyrus), subcortical network (right median cingulate gyrus, left parahippocampal gyrus, right insula), default-mode network (left superior frontal gyrus, left anterior cingulate and paracingulate gyri, left rectus gyrus), medial frontal network (inferior frontal gyrus), visual association network (fusiform gyrus), and frontoparietal network (right precentral gyrus, right inferior temporal gyrus). Table 3 shows the 20 brain areas with the highest metastability for each group.

Moreover, we computed the intrinsic ignition and metastability independently for each resting-state network. Figure 3 shows the absolute difference between the middle-age and older groups in the intrinsic-ignition values for each brain area in each network. Compared to the middle-age group, the older group had significantly increased intrinsic ignition in the frontoparietal network (FDR-corrected, $P < 0.001$) and medial frontal network (FDR-corrected, $P < 0.001$). By contrast, the middle-age group had greater intrinsic ignition in the motor network (FDR-corrected, $P < 0.001$). There were no significant differences between groups in intrinsic ignition in the default-mode, subcortical, visual I, visual II, or visual-association networks. Figure 4 shows the absolute difference between the middle-age and older groups in metastability values for each brain area in each network. Compared to the middle-age group, the older group had significantly increased metastability in the frontoparietal network (FDR-corrected, $P < 0.01$) and medial frontal network (FDR-corrected, $P < 0.01$). By contrast, the middle-age group had greater metastability in the default-mode (FDR-corrected, $P < 0.05$), subcortical (FDR-corrected, $P < 0.001$), motor (FDR-corrected, $P < 0.001$), visual association (FDR-corrected, $P < 0.05$), and visual I networks (FDR-corrected, $P < 0.001$). Only the visual II network did not differ significantly between groups.

LEiDA

Clustering across all subjects and timepoints identified three metastable substates. Figure 5*a* compares the probability of occurrence of each metastable substate between groups, and Figure 5*b* compares the duration of these substates between groups. Figure 5*c* shows the three metastable substates rendered onto a surface cortex. The metastable substate that had the highest probability of occurrence (the first metastable substate) closely overlaps with the state of global BOLD coherence

Table 2 Intrinsic ignition capability. The table shows the 20 brain areas with the highest intrinsic-ignition capability for each group. The first column shows the ignition capability of each brain area. The second column indicates the brain area in the resting-state parcellation. The third column corresponds to the overlap between the area of the resting-state atlas with the areas of the AAL structural parcellation. The fourth column shows the resting-state network to which the area belongs

Middle-age group				Senior Group			
Ignition	rs-fMRI atlas	Corresponding AAL-regions	Network	ignition	rs-fMRI atlas	Corresponding AAL-regions	Network
0.80099	74	34% Middle occipital gyrus, right 32% Middle temporal gyrus, right	Visual association	0.80161	74	34% Middle occipital gyrus, right 32% Middle temporal gyrus, right	Visual association
0.80053	185	88% Lingual gyrus, left	Visual	0.80133	181	40% Fusiform gyrus, left 31% Lingual gyrus, left	Visual_I
0.80034	79	78% Lingual gyrus, right	Visual	0.80118	173	63% Inferior temporal gyrus, left	Frontoparietal
0.80028	72	51% Lingual gyrus, right 33% Fusiform gyrus, right	Visual	0.80109	185	88% Lingual gyrus, left	Visual_I
0.80021	181	40% Fusiform gyrus, left 31% Lingual gyrus, left	Visual	0.80104	70	70% Inferior temporal gyrus, right	Frontoparietal
0.80010	205	43% Parahippocampal gyrus, left 24% Hippocampus, left	Subcortical	0.80095	14	85% Middle frontal gyrus, right	Frontoparietal
0.80009	69	51% Inferior temporal gyrus, right 47% Middle temporal gyrus, right	Visual association	0.80077	53	45% Temporal pole: superior, right 34% Temporal pole: middle temporal, right	Medialfrontal
0.80006	70	70% Inferior temporal gyrus, right	Frontoparietal	0.80060	69	51% Inferior temporal gyrus, right 47% Middle temporal gyrus, right	Visual association
0.80003	61	50% Superior temporal gyrus, right 28% Rolandic operculum, right	Motor	0.80058	187	38% Lingual gyrus, left 20% Calcarine fissure and surrounding cortex, left	Visual_II
0.79997	189	67% Calcarine fissure and surrounding cortex, left	Visual_I	0.80056	127	46% Inferior frontal gyrus, orbital part, left 36% Insula, left	Medialfrontal
0.79995	173	63% Inferior temporal gyrus, left	Frontoparietal	0.80053	166	82% Middle temporal gyrus, left	Medialfrontal
0.79991	183	41% Middle temporal gyrus, left 35% Middle occipital gyrus, left	Visual association	0.80053	180	49% Inferior occipital gyrus, left 33% Fusiform gyrus, left	Visual association
0.79987	36	52% Insula, right 36% Inferior frontal gyrus, orbital, right	Subcortical	0.80051	189	67% Calcarine fissure and surrounding cortex, left	Visual_I
0.79980	149	66% Superior parietal gyrus, left	Visual association	0.80049	80	39% Calcarine fissure and surrounding cortex, right 27% Cuneus, right	Visual_I
0.79979	123	84% Middle frontal gyrus, left	Medialfrontal	0.80043	76	48% Lingual gyrus, right 17% Fusiform gyrus, right	Visual_II
0.79976	139	81% Precentral gyrus, left	Medialfrontal	0.80042	12	52% Superior frontal gyrus, dorsolateral, right 41% Superior frontal gyrus, medial, right	Medialfrontal
0.79973	179	57% Lingual gyrus, left 21% Calcarine fissure and surrounding cortex, left	Visual_I	0.80041	179	57% Lingual gyrus, left 21% Calcarine fissure and surrounding cortex, left	Visual_I
0.79971	53	45% Temporal pole: superior, right 34% Temporal pole: middle temporal, right	Medialfrontal	0.80039	212	46% Thalamus, left 1% Lingual gyrus, left	Subcortical
0.79964	162	54% Temporal pole: superior temporal gyrus, left 27% Superior temporal gyrus, left	Motor	0.80037	183	41% Middle temporal gyrus, left 35% Middle occipital gyrus, left	Visual association
0.79964	63	52% Superior temporal gyrus, right 48% Middle temporal gyrus, right	Motor	0.80030	79	78% Lingual gyrus, right	Visual_I

Table 3 Metastability. The table shows the 20 brain areas with the highest metastability for each group (middle-age group and older group). The first column shows the metastability value of each brain area. The second column indicates the brain area in the resting-state parcellation. The third column corresponds to the overlap between the areas of the resting-state atlas with the areas of the AAL structural parcellation. The fourth column shows the resting-state network to which the area belongs

| Middle-age group				Senior group			
Metastability	rs-fMRI atlas	Corresponding AAL-regions	Network	Metastability	rs-fMRI atlas	Corresponding AAL-regions	Network
0.02982	96	60% Parahippocampal gyrus, right 28% Fusiform gyrus, right	Default mode	0.02949	169	46% Inferior temporal gyrus, left 41% Fusiform gyrus, left	Motor
0.02980	59	55% Fusiform gyrus, right 41% Inferior temporal gyrus, right	Visual association	0.02934	15	56% Median cingulate and paracingulate gyri, right 26% Anterior cingulate and paracingulate gyri, right	Subcortical
0.02976	187	38% Lingual gyrus, left 20% Calcarine fissure and surrounding cortex	Visual_II	0.02931	206	55% Fusiform gyrus, left 32% Parahippocampal gyrus, left	Subcortical
0.02971	161	57% Temporal pole: middle temporal gyrus, left 25% Middle temporal gyrus, left	Medialfrontal	0.02926	108	33% Anterior cingulate and paracingulate gyri, left 23% Rectus gyrus, left	Default mode
0.02969	70	70% Inferior temporal gyrus, right	Frontoparietal	0.02917	109	51% Inferior frontal gyrus, orbital part, left 31% Superior frontal gyrus, orbital part, left	Subcortical
0.02967	71	48% Fusiform gyrus, right 29% Inferior temporal gyrus, right	Visual association	0.02914	16	45% Inferior frontal gyrus, triangular part, right 28% Inferior frontal gyrus, orbital, right	Medialfrontal
0.02966	180	49% Inferior occipital gyrus, left 33% Fusiform gyrus, left	Visual association	0.02913	88	42% Median cingulate and paracingulate gyri, right	Subcortical
0.02964	188	25% Inferior occipital gyrus, left 23% Lingual gyrus, left	Visual_II	0.02913	57	67% Inferior temporal gyrus, right	Medialfrontal
0.02963	172	71% Fusiform gyrus, left	Visual_I	0.02910	18	59% Inferior frontal gyrus, orbital, right 20% Insula, right	Subcortical
0.02962	27	81% Precentral gyrus, right	Motor	0.02910	112	54% Superior frontal gyrus, medial orbital, left 31% Anterior cingulate and paracingulate gyri, left	Default mode
0.02960	45	47% Supramarginal gyrus, right 35% Postcentral gyrus, right	Motor	0.02908	174	58% Fusiform gyrus, left 36% Inferior temporal gyrus, left	Visual association
0.02956	206	55% Fusiform gyrus, left 32% Parahippocampal gyrus, left	Subcortical	0.02904	142	59% Insula, left 23% Rolandic operculum, left	Motor
0.02956	177	73% Middle occipital gyrus, left	Default mode	0.02902	175	65% Inferior temporal gyrus, left	Visual association
0.02954	53	45% Temporal pole: superior, right 34% Temporal pole: middle temporal, right	Medialfrontal	0.02901	111	62% Rectus gyrus, left	Medialfrontal
0.02951	81	59% Inferior occipital gyrus, right 23% Lingual gyrus, right	Visual_II	0.02898	122	44% Superior frontal gyrus, medial, left 43% Superior frontal gyrus, dorsolateral, left	Medialfrontal
0.02949	204	46% Hippocampus, left 19% Inferior temporal gyrus, left	Subcortical	0.02898	46	53% Superior temporal gyrus, right 37% Supramarginal gyrus, right	Motor
0.02945	175	65% Inferior temporal gyrus, left	Visual association	0.02897	71	48% Fusiform gyrus, right 29% Inferior temporal gyrus, right	Visual association
0.02944	173	63% Inferior temporal gyrus, left	Frontoparietal	0.02897	61	50% Superior temporal gyrus, right 28% Rolandic operculum, right	Motor
0.02944	97	67% Parahippocampal gyrus, right	Motor	0.02894	31	52% Precentral gyrus, right 22% Inferior frontal gyrus, opercular part, right	Frontoparietal
0.02942	203	55% Hippocampus, left 13% Parahippocampal gyrus, left	Subcortical	0.02893	55	67% Inferior temporal gyrus, right	Frontoparietal
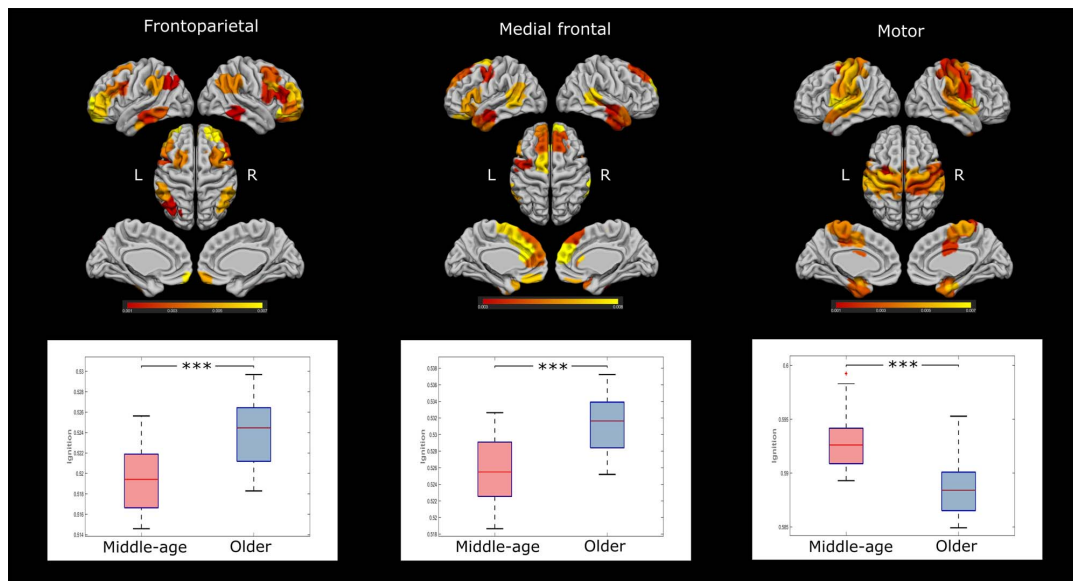
Figure 3. Differences in ignition across resting-state networks. The plots show the differences between groups in each significant resting-state network; rendered brains represent the absolute difference in ignition values for each brain area in each network between the middle-age and older groups (the greatest difference is marked in yellow). Compared to the middle-age group, intrinsic ignition was significantly higher in the older group in the frontoparietal network (FDR-corrected, $P < 0.001$) and medial frontal network (FDR-corrected, $P < 0.001$). By contrast, intrinsic ignition was significantly higher in the middle-age group in the motor network (FDR-corrected, $P < 0.001$). The default-mode, subcortical, visual I, visual II, and visual association networks were not significantly different between groups.

(Cabral et al. 2017). The probability of this substate occurring was higher in the older group [0.476 ± 0.008 (mean $\pm$ standard error) vs. 0.453 ± 0.008 in the middle-age group, FDR-corrected $P = 0.03$], and this substate also lasted longer in the older age group [32.465 ± 0.957 s vs. 30.265 ± 0.791 s in the middle-age group, $P = 0.04$], although the difference in duration was no longer significant after FDR correction. The second metastable substate is especially interesting because it closely overlaps with the so-called rich club (Hagmann et al. 2008; van den Heuvel and Sporns 2011; van den Heuvel et al. 2012; Sporns 2013). In particular, this substate involved the following areas in both hemispheres: the superior frontal cortex, precuneus, insula, and subcortical areas, such as the caudate, putamen, hippocampus, and thalamus (see Fig. 5d and Table 4). The networks most frequently involved in this metastable substate were the subcortical network, visual network, motor network, default-mode network, and medial frontal network. The probability of this substate occurring was greater in the middle-age group [0.288 ± 0.007 vs. 0.269 ± 0.006 in the older group, FDR-corrected $P = 0.026$], and this substate also lasted longer in the middle-age group [16.399 ± 0.605s vs. 14.853 ± 0.414 s in the older group, FDR-corrected $P = 0.01$]. The third metastable substate was not significantly different between groups in its probability of occurrence ($P = 0.35$) or duration ($P = 0.39$).

Intrinsic Ignition Within the Significant Metastable Substate (Functional-Rich Club)

Finally, we computed the intrinsic-ignition framework within the significant metastable substate overlapping with the rich club. In brief, we obtained the brain areas showing positive values in the BOLD phases from the leading eigenvector (Fig. 5d). Then, we computed the intrinsic ignition and metastability within the metastable substate. Figure 5e shows the boxplots for the comparisons. Compared to the older group, the middle-age group had significantly higher intrinsic ignition ($P = 0.0093$) and metastability ($P = 0.0426$) within the substate.

Discussion

Interest in characterizing resting-state functional patterns during aging is growing. Understanding the underlying dynamics across the whole-brain functional network may help us better understand age-related changes. In this line, various methods have been developed to capture statistical properties of resting-state fMRI data beyond classical static functional connectivity, providing a new perspective to interpret brain functioning during the resting scan. To investigate the underlying whole-brain dynamics, we applied two data-driven whole-brain methods based on phase coherence synchronization (Cabral et al. 2017; Deco and Kringelbach 2017) to compare intrinsic ignition, metastability, and metastable substates between middle-aged and older subjects from a large sample of healthy human adults. To characterize the spatiotemporal propagation of information, we used the Intrinsic-Ignition Framework to measure the degree of integration of spontaneously occurring events across the whole-brain during rest. Ignition values across the whole-brain functional network were higher in older subjects than in middle-aged subjects, but older subjects also had less metastability. Applying Leading Eigenvector Dynamics Analysis (LEiDA), we found differences between groups in the probability of occurrence and duration of a metastable substate involving rich-club
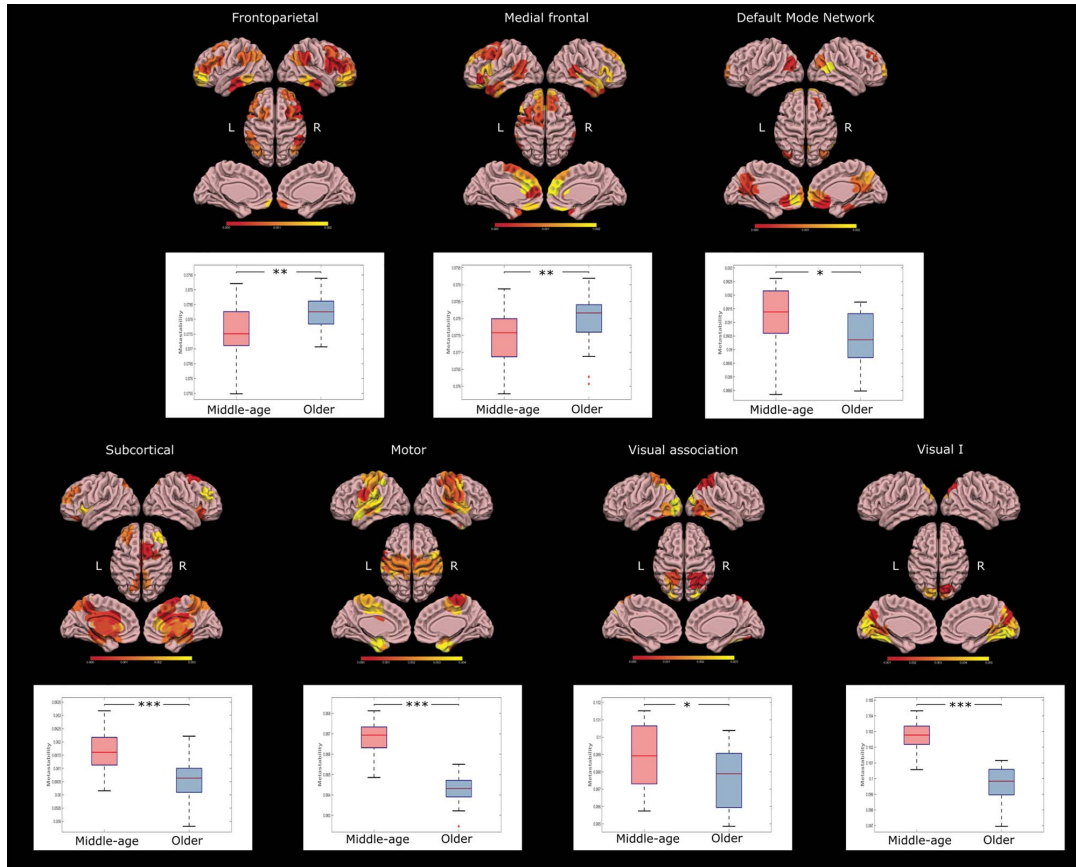
Figure 4. Differences in metastability across resting-state networks. The plots show the differences between groups in each significant resting-state network, whereas rendered brains represent the absolute difference (middle-age and older) between metastability values for each brain area in each network (in yellow the highest difference). The older group showed significantly increased metastability compared to the middle-age group in the frontoparietal network (FDR-corrected, $P < 0.01$) and medial frontal network (FDR-corrected, $P < 0.01$), whereas the middle-age group showed increased metastability in the default-mode network (FDR-corrected, $P < 0.05$), subcortical network (FDR-corrected, $P < 0.001$), motor network (FDR-corrected, $P < 0.001$), visual association network (FDR-corrected, $P < 0.05$), and visual I network (FDR-corrected, $P < 0.001$).

brain areas, as well as in the probability of occurrence of a substate that is related to the global coherence state.

Interestingly, the older group had higher intrinsic ignition across the whole-brain functional network (Fig. 2a); the brain areas with the highest intrinsic-ignition values were mainly distributed across the visual networks, frontoparietal network, and medial frontal network (Fig. 2a and Table 2). The mean intrinsic-ignition value reflects spatial diversity and the broadness of communication across the whole network. These results are in line with previous studies investigating the effects of aging in resting-state networks. Geerligs et al. (2015) reported increased connectivity in older adults between the visual network and somatomotor network as well as between the visual network and cingulo-opercular network. Betzel et al. (2014) found increased functional connectivity between the dorsal attention network and the salience/ventral attention networks in older adults. Similarly, Spreng et al. (2016) found increased between-network functional connectivity across the

default-mode network and dorsal attention networks during both task and rest conditions. We conclude that increased functional connectivity between resting-state networks has a significant impact across the whole-brain functional network as evidenced by the level of intrinsic ignition.

Simple or classical methods do not capture the variability over time (metastability) across the whole-brain network. Here, we explored the spatiotemporal processes that occur across the whole brain during aging. Our results show that metastability was higher in the middle-age group (Fig. 2b and Table 3). This finding is particularly interesting because middle-age adults showed lower intrinsic ignition across the whole-brain functional network compared to older adults, but the underlying dynamics of the middle-age adults seem to be more complex across time. These results are in line with theories on brain dynamics, which suggest that metastability, characterized by a flexible and rapid dynamic repertoire of brain states, is the optimal state of neural activity at rest (Tognoli and Kelso
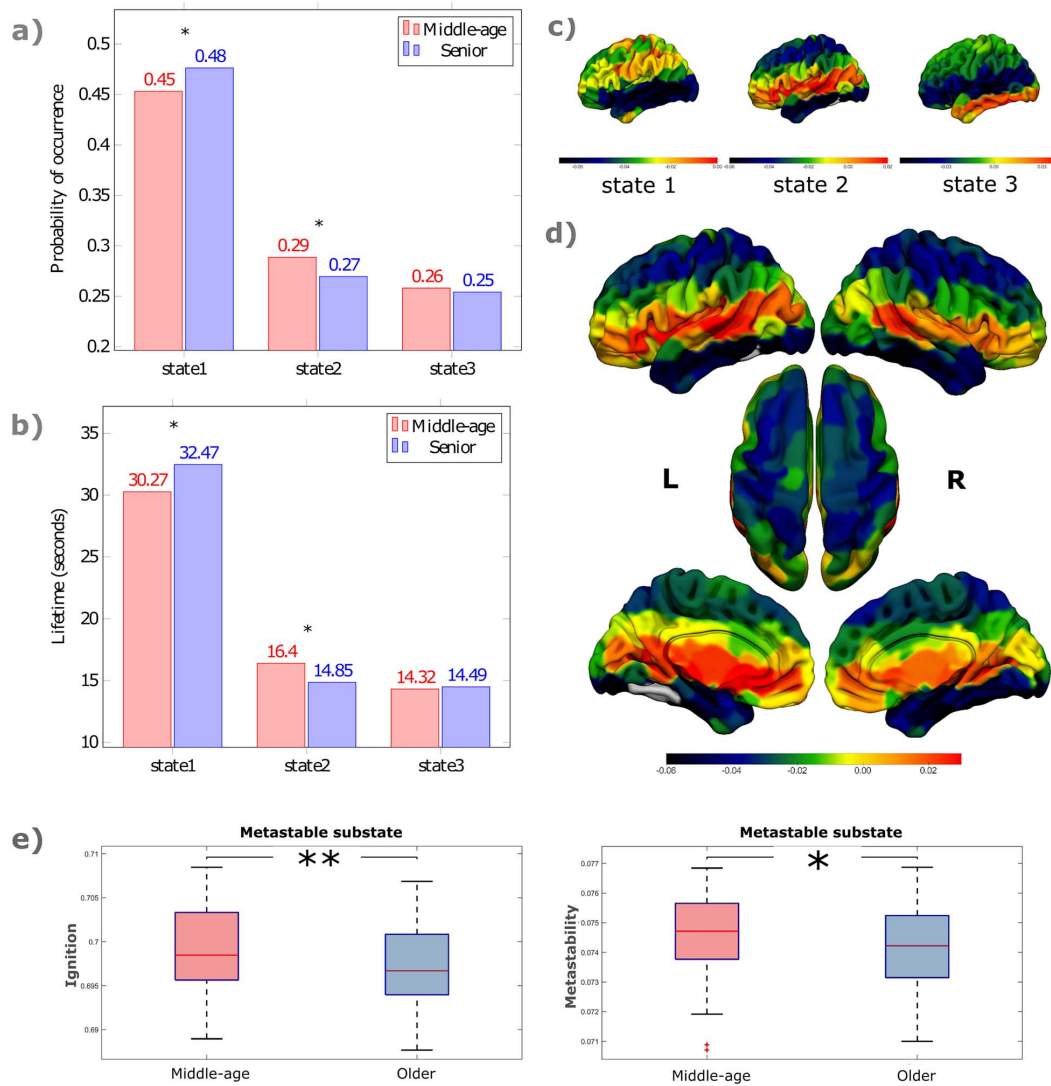
Figure 5. Metastable substates obtained by clustering. We identified three metastable substates that occurred frequently across all subjects during rest. The states are shown from higher to lower probability of occurrence. (*a*) Differences in probability and (*b*) differences in duration of each metastable substate between the middle-age (in red) group and the older group (in blue) during the resting-state scan. (*c*) Metastable substates rendered on the cortex with Surfice. The first metastable substate had the highest probability of occurrence. This state was more likely to occur in subjects in the older group (mean, 0.476 ± 0.008 (s.e.) versus 0.453 ± 0.008 in the middle-age group, FDR-corrected $P = 0.03$); the duration of this state was also higher in the older group (32.465 ± 0.957 s versus 30.265 ± 0.791 in the middle-age group, $P = 0.04$, uncorrected). The second metastable substate is especially interesting because it overlaps with the rich club. The probability of this state occurring was higher in the middle-age group (mean 0.288 ± 0.007 (s.e.) versus 0.269 ± 0.006 in the older group, FDR-corrected $P = 0.026$); the duration of this state was also higher in the middle-age group (mean 16.399 ± 0.605 s versus 14.853 ± 0.414 s in the older group, FDR-corrected $P = 0.01$). The third metastable substate was not significantly difference between groups in its probability of occurrence ($P = 0.35$) or duration ($P = 0.39$). (*d*) Relevant metastable substate overlapping with rich-club regions in both hemispheres (the superior frontal cortex, precuneus, insula, and subcortical areas such as the caudate, putamen, hippocampus, and thalamus). (*e*) Ignition and metastability within the significant metastable substate. The boxplots show the mean integration (ignition) and metastability for each group (middle-age group and older group) within the significant metastable substate. Both ignition ($P = 0.0093$) and metastability ($P = 0.0426$) were higher in in the middle-age group (in red) than in the older group (in blue). P-values are based on Monte–Carlo permutation tests, $*$ represents $P < 0.05$ and $**$ represents $P < 0.01$.

Table 4 Cluster centroids of the significant metastable substate. The table shows the 20 brain areas with the highest BOLD phase of the significant metastable substate

BOLD phase	rs-fMRI atlas	Corresponding AAL-regions	Network
0.03165	37	34% Insula, right/22% lenticular nucleus, putamen, right	Motor
0.03151	201	42% Hippocampus, left/5% thalamus, left	Subcortical
0.02814	144	34% Insula, left/18% superior temporal gyrus, left	Motor
0.02683	211	84% Lenticular nucleus, putamen, left	Subcortical
0.02653	103	84% Lenticular nucleus, putamen, right	Subcortical
0.02534	87	44% Calcarine fissure and surrounding cortex, right/6% lingual gyrus, right	Visual_I
0.02502	65	64% Middle temporal gyrus, right	Medial frontal
0.02415	108	33% Anterior cingulate and paracingulate gyri, left/23% rectus gyrus, left	Default mode
0.02271	102	57% Caudate nucleus, right/11% olfactory cortex, right	Subcortical
0.02262	143	81% Insula, left	Subcortical
0.02246	212	46% Thalamus, left/1% lingual gyrus, left	Subcortical
0.02191	165	62% Middle temporal gyrus, left	Motor
0.02145	93	50% Hippocampus right/9% parahippocampal right	Subcortical
0.02133	190	59% Calcarine fissure and surrounding cortex/7% lingual gyrus, left	Visual_I
0.02053	50	87% Middle temporal gyrus, right	Default mode
0.02036	105	36% Thalamus, right/9% lingual gyrus, right	Subcortical
0.01982	98	49% Lingual gyrus, right/23% precuneus, right	Visual_I
0.01935	209	28% Caudate nucleus, left/15% olfactory cortex, left	Subcortical
0.01870	82	76% Calcarine fissure and surrounding cortex, right	Visual_I
0.01771	54	58% Middle temporal gyrus, right/32% superior temporal gyrus, right	Medial frontal

2014; Córdova-Palomera et al. 2017; Deco et al. 2017b). Greater metastability reflects more complex brain dynamics (i.e., more flexible switching across time), whereas lower metastability suggests a more stable system (Deco and Kringelbach 2017; Jobst et al. 2017; Deco et al. 2017a). Decreased metastability has been related to cognitive and behavioral decline in Alzheimer's disease (Córdova-Palomera et al. 2017), as well as to reduced cognitive ability and damage to structural connectivity in traumatic brain injury (Hellyer et al. 2015). Our findings of lower metastability across the whole-brain network in the older group reflect reductions in brain flexibility and complexity during aging. Thus, this temporal dynamic measure could potentially serve as a biomarker in aging and brain damage. Our findings are in line with previous studies on the effects of aging on brain functional dynamics. For example, the decreased metastability in the older group in our study echoes recent studies that suggest deficient network modulation in the elderly (Turner and Spreng 2015; Damoiseaux 2017). Xia et al. (2019) found that the number of transitions between different metastable substates decreased with age, leading them to conclude that resting mind states may shift faster in young people than in older people. Similarly, variability across large-scale networks decreases linearly with aging over the lifespan (Nomi et al. 2017) and in healthy elderly subjects (Lou et al. 2019). Moreover, our findings that areas in the temporal and occipital regions were the most important for the broadcasting of information in the middle-age group (Fig. 2b and Table 3) is consistent with the results of recent time-varying resting-state fMRI studies (Nomi et al. 2017; Kumral et al. 2019). Similarly, our findings that the frontal and temporal areas were more relevant in the older group (Fig. 2b and Table 3) are consistent with the results of a recent

EEG study that found an enhanced brain dynamics of phase synchronization in the alpha-band frequency, predominantly in frontal areas (Nobukawa et al. 2019), which the authors suggest could reflect a general change in functional connectivity dynamics during aging. Moreover, overactivation in prefrontal brain areas has been previously observed in older adults during fMRI tasks, giving rise to different theories (Cabeza 2002; Davis et al. 2008; Reuter-Lorenz and Cappell 2008).

We also explored intrinsic ignition and metastability across large-scale networks, computing the intrinsic-ignition framework within eight resting-state networks. In the older group, the frontoparietal and medial frontal networks showed higher ignition and metastability (Figs. 3 and 4). These findings are in line with those reported by Lou et al. (2019), who found that the frontal and temporal lobes show a more dynamic pattern with increasing age. A recent meta-analysis pointed out that age-related changes in activation commonly affect the frontoparietal and default-mode networks (Li et al. 2015). The frontoparietal network serves as a flexible hub and plays a vital role in adaptive control and implementation of different responses to demands during tasks (Cole et al. 2013). The frontoparietal network is also involved in selecting relevant information from the environment (Ptak 2012). The default-mode and frontoparietal networks are also thought to be critical in controlling global brain dynamics (Hellyer et al. 2014). Although greater frontal brain activity in older subjects has been interpreted as a compensatory cortical response to delay cognitive decline (Cabeza et al. 2018), recent evidence suggests that increased frontal activity is actually more related to reduced efficiency or specificity than to compensation. Applying a model-based multivariate analysis, Morcom and Henson (2018) found that increased frontal brain

activity was less predictive of the cognitive outcome. Nevertheless, why this frontal overactivation occurs in aging remains unclear.

In the present study, metastability within the default-mode, subcortical, and visual-association networks was higher in the middle-age group (Fig. 4). In a recent study in a large cohort of young subjects, Lee et al. (2019) reported higher metastability in lower-order resting-state networks, such as the visual network and auditory network, which are involved in specialized, mostly externally driven functions. These networks' greater metastability might reflect a greater capacity to change their functional configuration in response to diverse, rapidly changing external inputs (Power et al. 2011). By contrast, higher-order networks such as the default-mode and central executive networks are mostly involved in internal and goal-directed processing (Raichle et al. 2001; Raichle and Snyder 2007), so it would make sense for their functional configurations to last longer. Moreover, the previously mentioned study also found that metastability was strongly associated with various indicators of higher-order cognitive ability and physical well-being (Lee et al. 2019).

One of the most noteworthy results in our study was the identification of a metastable substate overlapping the so-called the 'rich club' of densely interconnected nodes (Hagmann et al. 2008; van den Heuvel and Sporns 2011; van den Heuvel et al. 2012; Sporns 2013; Deco et al. 2017a). This substate involved the superior frontal cortex, precuneus, insula, and subcortical areas (caudate, putamen, hippocampus, and thalamus) in both hemispheres. It is thought that the rich club might also act as a gatekeeper that coordinates interactions with lower-degree regions and the emergence of different functional network configurations (van den Heuvel and Sporns 2011). We found that the metastable substate corresponding to the rich club was less likely to occur in the older group and that when it did occur, it did so for shorter periods of time. Furthermore, we computed the Intrinsic-Ignition Framework within the significant metastable substate and found that both ignition and metastability were significantly lower in the older group than in the middle-age group, demonstrating that in addition to decreased overall ignition capacity and metastability, older subjects have a lower probability of accessing the rich club and spending time in this state. Moreover, the higher ignition and metastability in medial frontal and frontoparietal networks in the older group could be due to the disruption among rich-club nodes rather than to a compensatory shift from posterior to anterior brain activity. Rich-club nodes mediate communication among functional systems. Thus, one possibility could be that older subjects spend more time in frontal networks because these nodes have become less efficient with aging, reducing their brain's ability to switch among functional systems. Damoiseaux (2017) suggested that less-efficient rich-club network might be responsible for the differences in brain dynamics observed in older subjects. Our findings are in line with the hypothesis that the rich club connects different functional modules in the brain that partially overlap with different resting-state networks (Biswal et al. 1995; van den Heuvel and Sporns 2011). Our findings regarding the lower probability of occurrence and shorter duration of this substate in the older group might be due to alterations in the intrinsic dynamics of this particular metastable substate or in any of the brain areas involved. Rich-club regions play a key role in integrating information across the brain network; consequently, damage to a brain area belonging to the rich club can affect global communication and have repercussions

in multiple cognitive domains (van den Heuvel and Hulshoff Pol 2010; Baggio et al. 2015; Deco and Kringelbach 2017). Finally, our results are consistent with the observation that the efficiency of the rich-club network increases during brain development in early life and decreases late in life in a manner that yields an inverted-U when plotted along the lifespan (Cao et al. 2014; Zhao et al. 2015; Damoiseaux 2017).

Our LEiDA analysis also found that the first metastable substate, which has been related to the global signal in fMRI studies, had a higher probability of occurrence and longer duration in the older group (Fig. 3), although this last comparison was no longer significant after correction for multiple comparisons. Like in previous resting-state fMRI studies applying LEiDA (Cabral et al. 2017; Figueroa et al. 2019; Lord et al. 2019), this anti-correlated state of global BOLD phase coherence (i.e., all BOLD phases showing negative values in the leading eigenvector) was the most prevalent. Although the significance of the global signal remains controversial, growing evidence suggests that it could contain valuable neurophysiological information and should not therefore be treated as a nuisance term (Saad et al. 2012; Liu et al. 2017). In a study with simultaneous fMRI and EEG acquisition during rest, Wong et al. (2013) found that increased EEG vigilance induced with caffeine was associated with decreased global signal amplitude and increased anti-correlation between the default-mode network and the task-positive network. Moreover, the global signal amplitude seems to increase during early sleep stages (Fukunaga et al. 2006). However, the role of the global BOLD phase coherence state remains unclear and needs further investigation (Cabral et al. 2017).

This study has several limitations. Although this cross-sectional study analyzed data from a large sample of healthy human adults, it would be very instructive to explore the age-related changes in neuroimaging in the same subjects in a longitudinal study. Data-driven methods alone are insufficient to understand the mechanisms underlying the process of aging or explain the causes of the dynamic changes observed. On the other hand, brain models simulating time series have advanced our understanding of the relationship between structure and function in the brain and the potential repercussions of disrupted connectivity from injury or disease; moreover, in silico simulations open the possibility of discovering potential stimulation targets to shift patients' global brain dynamics toward a healthier state (Deco and Kringelbach 2014; Deco et al. 2019a). Here, we used a resting-state brain atlas that ensures functional homogeneity within nodes and that is consistent at the group level (Shen et al. 2013). However, the results in studies of brain networks can vary depending on the parcellation used (Wang et al. 2009; Zalesky et al. 2010). Moreover, we used a 1.5 T scanner with TR = 2.5; using a higher magnetic field (e.g., 3 T or 7 T) and a lower TR would increase sensitivity and resolution and thus might provide better information about functional brain networks. We did not correlate our findings with age or measures of cognitive function; one line for future studies could focus on assessing the behavioral relevance of intrinsic ignition and metastability through the aging process. Finally, although age is strongly associated with changes in functional connectivity, more studies are needed to further characterize brain functional connectivity in older adults and resolve inconsistent results due to methodological differences among studies.

In conclusion, applying two novel data-driven approaches to examine whole-brain dynamic changes, this work provides new

insights into age-related brain changes. Our findings suggest that, compared to middle-aged subjects, older subjects show higher ignition but lower metastability across the whole-brain network, as well as reduced access to a dynamic functional connectivity pattern that is key for communication in the brain. These findings support the hypothesis that cognitive processing methods differ between middle-aged and older adults. Taken together, these findings suggest that functional whole-brain dynamics are altered in aging, probably due to an imbalance in a metastable subsate that involves brain areas of the so-called rich club. Further investigations will surely improve our understanding of brain changes during aging.

Notes

Funding

References

Abrol A, Chaze C, Damaraju E, Calhoun VD. 2016. The chronnectome: evaluating replicability of dynamic connectivity patterns in 7500 resting fMRI datasets. *Conf Proc IEEE Eng Med Biol Soc.* 5571–5574. https://doi.org/10.1109/embc.2016.7591989.

Agcaoglu O, Wilson TW, Wang YP, Stephen J, Calhoun VD. 2019. Resting state connectivity differences in eyes open versus eyes closed conditions. *Hum Brain Mapp.* 40:2488–2498.

Baggio HC, Segura B, Junque C, de Reus MA, Sala-Llonch R, Van den Heuvel MP. 2015. Rich Club organization and cognitive performance in healthy older participants. *J Cogn Neurosci.* 27:1801–1810.

Behzad Y, Restom K, Liau J, Liu TT. 2007. A component-based noise correction method (CompCor) for BOLD and perfusion-based fMRI. *Neuroimage.* 37:90–101.

Betzel RF, Byrge L, He Y, Goñi J, Zuo XN, Sporns O. 2014. Changes in structural and functional connectivity among resting-state networks across the human lifespan. *Neuroimage.* 102:345–357.

Biswal B, Zerrin Yetkin F, Haughton VM, Hyde JS. 1995. Functional connectivity in the motor cortex of resting human brain using echo-planar MRI. *Magn Reson Med.* 34:537–541.

Cabeza R. 2002. Hemispheric asymmetry reduction in older adults: the HAROLD model. *Psychol Aging.* 17:85–100.

Cabeza R, Albert M, Belleville S, Craik FI, Duarte A, Grady CL, Lindenberger U, Nyberg L, Park DC, Reuter-Lorenz PA *et al.* 2018. Maintenance, reserve and compensation: the cognitive neuroscience of healthy ageing. *Nat Rev Neurosci.* 19:701–710.

Cabral J, Hugues E, Sporns O, Deco G. 2011. Role of local network oscillations in resting-state functional connectivity. *Neuroimage.* 57:130–139.

Cabral J, Vidaurre D, Marques P, Magalhães R, Silva Moreira P, Miguel Soares J, Deco G, Sousa N, Kringelbach ML. 2017. Cognitive performance in healthy older adults relates to spontaneous switching between states of functional connectivity during rest. *Sci Rep.* 7:5135.

Cao M, Wang JH, Dai ZJ, Cao XY, Jiang LL, Fan FM, Song XW, Xia MR, Shu N, Dong Q *et al.* 2014. Topological organization of the human brain functional connectome across the lifespan. *Dev Cogn Neurosci.* 7:76–93.

Chao-Gan Y, Yu-Feng Z. 2010. DPARSF: a MATLAB toolbox for "pipeline" data analysis of resting-state fMRI. *Front Syst Neurosci.* 4:13.

Cole MW, Reynolds JR, Power JD, Repovs G, Anticevic A, Braver TS. 2013. Multi-task connectivity reveals flexible hubs for adaptive task control. *Nat Neurosci.* 16:1348–1355.

Córdova-Palomera A, Kaufmann T, Persson K, Alnæs D, Doan NT, Moberget T, Lund MJ, Barca ML, Engvig A, Brækhus A *et al.* 2017. Disrupted global metastability and static and dynamic brain connectivity across individuals in the Alzheimer's disease continuum. *Sci Rep.* 7:40268.

Damoiseaux J, Beckmann C, Arigita ES, Barkhof F, Scheltens P, Stam C, Smith S, Rombouts S. 2008. Reduced resting-state brain activity in the "default network" in normal aging. *Cereb Cortex.* 18:1856–1864.

Damoiseaux JS. 2017. Effects of aging on functional and structural brain connectivity. *Neuroimage.* 160:32–40.

Davis SW, Dennis NA, Daselaar SM, Fleck MS, Cabeza R. 2008. Que PASA? The posterior-anterior shift in aging. *Cereb Cortex.* 18:1201–1209.

Deco G, Cruzat J, Cabral J, Tagliazucchi E, Laufs H, Logothetis NK, Kringelbach ML. 2019a. Awakening: predicting external stimulation to force transitions between different brain states. *Proc Natl Acad Sci.* 116:18088–18097.

Deco G, Cruzat J, Kringelbach ML. 2019b. Brain songs framework used for discovering the relevant timescale of the human brain. *Nat Commun.* 10:583.

Deco G, Jirsa VK, McIntosh AR. 2011. Emerging concepts for the dynamical organization of resting-state activity in the brain. *Nat Rev Neurosci.* 12:43–56.

Deco G, Kringelbach ML. 2014. Great expectations: using whole-brain computational connectomics for understanding neuropsychiatric disorders. *Neuron.* 84:892–905.

Deco G, Kringelbach ML. 2016. Metastability and coherence: extending the communication through coherence hypothesis using a whole-brain computational perspective. *Trends Neurosci.* 39:125–135.

Deco G, Kringelbach ML. 2017. Hierarchy of information processing in the brain: a novel 'intrinsic ignition' framework. *Neuron.* 94:961–968.

Deco G, Kringelbach ML, Jirsa VK, Ritter P. 2017a. The dynamics of resting fluctuations in the brain: metastability and its dynamical cortical core. *Sci Rep*. 7:3095.

Deco G, Tagliazucchi E, Laufs H, Sanjuan A, Kringelbach ML. 2017b, 2017. Novel intrinsic ignition method measuring local-global integration characterizes wakefulness and deep sleep. *eNeuro*. 4(e0106–17):1–12.

Deco G, Tononi G, Boly M, Kringelbach ML. 2015. Rethinking segregation and integration: contributions of whole-brain modelling. *Nat Rev Neurosci*. 16:430–439.

Escrichs A, Sanjuan A, Atasoy S, López-González A, Garrido C, Càmara E, Deco G. 2019. Characterizing the dynamical complexity underlying meditation. *Front Syst Neurosci*. 13:27.

Ferreira LK, Busatto GF. 2013. Resting-state functional connectivity in normal brain aging. *Neurosci Biobehav Rev*. 37:384–400.

Figueroa CA, Cabral J, Mocking RJT, Rapuano KM, van Hartevelt TJ, Deco G, Expert P, Schene AH, Kringelbach ML, Ruhé HG. 2019. Altered ability to access a clinically relevant control network in patients remitted from major depressive disorder. *Hum Brain Mapp*. 40:2771–2786.

Finn ES, Shen X, Scheinost D, Rosenberg MD, Huang J, Chun MM, Papademetris X, Constable RT. 2015. Functional connectome fingerprinting: identifying individuals using patterns of brain connectivity. *Nat Neurosci*. 18:1664–1671.

Fjell AM, Sneve MH, Grydeland H, Storsve AB, Walhovd KB. 2017. The disconnected brain and executive function decline in aging. *Cereb Cortex*. 27:2303–2317.

Fukunaga M, Horovitz SG, van Gelderen P, de Zwart JA, Jansma JM, Ikonomidou VN, Chu R, Deckers RH, Leopold DA, Duyn JH. 2006. Large-amplitude, spatially correlated fluctuations in BOLD fMRI signals during extended rest and early sleep stages. *Magn Reson Imaging*. 24:979–992.

Geerligs L, Renken RJ, Saliasi E, Maurits NM, Lorist MM. 2015. A brain-wide study of age-related changes in functional connectivity. *Cereb Cortex*. 25:1987–1999.

Glerean E, Salmi J, Lahnakoski JM, Jääskeläinen IP, Sams M. 2012. Functional magnetic resonance imaging phase synchronization as a measure of dynamic functional connectivity. *Brain Connect*. 2:91–101.

Grady C, Sarraf S, Saverino C, Campbell K. 2016. Age differences in the functional interactions among the default, frontoparietal control, and dorsal attention networks. *Neurobiol Aging*. 41:159–172.

Hagmann P, Cammoun L, Gigandet X, Meuli R, Honey CJ, Wedeen VJ, Sporns O. 2008. Mapping the structural core of human cerebral cortex. *PLoS Biol*. 6:e159.

Hellyer PJ, Scott G, Shanahan M, Sharp DJ, Leech R. 2015. Cognitive flexibility through metastable neural dynamics is disrupted by damage to the structural connectome. *J Neurosci*. 35:9050–9063.

Hellyer PJ, Shanahan M, Scott G, Wise RJ, Sharp DJ, Leech R. 2014. The control of global brain dynamics: opposing actions of frontoparietal control and default mode networks on attention. *J Neurosci*. 34:451–461.

Hochberg Y, Benjamini Y. 1990. More powerful procedures for multiple significance testing. *Stat Med*. 9:811–818.

Hutchison RM, Womelsdorf T, Allen EA, Bandettini PA, Calhoun VD, Corbetta M, Della Penna S, Duyn JH, Glover GH, Gonzalez-Castillo J et al. 2013. Dynamic functional connectivity: promise, issues, and interpretations. *Neuroimage*. 80:360–378.

Jenkinson M, Bannister P, Brady M, Smith S. 2002. Improved optimization for the robust and accurate linear registration and motion correction of brain images. *Neuroimage*. 17:825–841.

Jobst BM, Hindriks R, Laufs H, Tagliazucchi E, Hahn G, Ponce-Alvarez A, Stevner ABA, Kringelbach ML, Deco G. 2017. Increased stability and breakdown of brain effective connectivity during slow-wave sleep: mechanistic insights from whole-brain computational modelling. *Sci Rep*. 7:4634.

Kumral D, Şansal F, Cesnaite E, Mahjoory K, Al E, Gaebler M, Nikulin V, Villringer A. 2019. BOLD and EEG signal variability at rest differently relate to aging in the human brain. *Neuroimage*. 207:116373.

Lee WH, Moser DA, Ing A, Doucet GE, Frangou S. 2019. Behavioral and health correlates of resting-state metastability in the human connectome project. *Brain Topogr*. 32:80–86.

Li HJ, Hou XH, Liu HH, Yue CL, Lu GM, Zuo XN. 2015. Putting age-related task activation into large-scale brain networks: a meta-analysis of 114 fMRI studies on healthy aging. *Neurosci Biobehav Rev*. 57:156–174.

Liu TT, Nalci A, Falahpour M. 2017. The global signal in fMRI: nuisance or information? *Neuroimage*. 150:213–229.

Lord LD, Expert P, Atasoy S, Roseman L, Rapuano K, Lambiotte R, Nutt DJ, Deco G, Carhart-Harris RL, Kringelbach ML et al. 2019. Dynamical exploration of the repertoire of brain networks at rest is modulated by psilocybin. *Neuroimage*. 199:127–142.

Lou W, Wang D, Wong A, Chu WC, Mok VC, Shi L. 2019. Frequency-specific age-related decreased brain network diversity in cognitively healthy elderly: a whole-brain data-driven analysis. *Hum Brain Mapp*. 40:340–351.

Martínez SA, Marsman JBC, Kringelbach ML, Deco G, ter Horst GJ. 2020. Reduced spatiotemporal brain dynamics are associated with increased depressive symptoms after a relationship breakup. *NeuroImage Clin*. 27:102299.

Morcom AM, Henson RN. 2018. Increased prefrontal activity with aging reflects non-specific neural responses rather than compensation. *J Neurosci*. 38:7303–7313.

Nobukawa S, Kikuchi M, Takahashi T. 2019. Changes in functional connectivity dynamics with aging: a dynamical phase synchronization approach. *Neuroimage*. 188:357–368.

Nomi JS, Bolt TS, Ezie CEC, Uddin LQ, Heller AS. 2017. Moment-to-moment BOLD signal variability reflects regional changes in neural flexibility across the lifespan. *J Neurosci*. 37:5539–5548.

Onoda K, Ishihara M, Yamaguchi S. 2012. Decreased functional connectivity by aging is associated with cognitive decline. *J Cogn Neurosci*. 24:2186–2198.

Padilla N, Saenger V, van Hartevelt TJ, Fernandes HM, Lennartsson F, Andersson JLR, Kringelbach ML, Deco G, Aden U. 2019. Breakdown of whole-brain dynamics in preterm-born children. *Cereb Cortex*. 30:1159–1170.

Patriat R, Molloy EK, Meier TB, Kirk GR, Nair VA, Meyerand ME, Prabhakaran V, Birn RM. 2013. The effect of resting condition on resting-state fMRI reliability and consistency: a comparison between resting with eyes open, closed, and fixated. *Neuroimage*. 78:463–473.

Ponce-Alvarez A, Deco G, Hagmann P, Romani GL, Mantini D, Corbetta M. 2015. Resting-state temporal synchronization networks emerge from connectivity topology and heterogeneity. *PLoS Comput Biol*. 11:e1004100.

Power JD, Cohen AL, Nelson SM, Wig GS, Barnes KA, Church JA, Vogel AC, Laumann TO, Miezin FM, Schlaggar BL et al. 2011. Functional network Organization of the Human Brain. *Neuron*. 72:665–678.

Ptak R. 2012. The frontoparietal attention network of the human brain. *Neuroscientist*. 18:502–515.

Puig J, Biarnes C, Pedraza S, Vilanova JC, Pamplona R, Fernández-Real JM, Brugada R, Ramos R, Coll-de-Tuero G, Calvo-Perxas L et al. 2020. The aging imageomics study: rationale, design, and baseline characteristics of the study population. *Mech Ageing Dev*. 189:111257.

Puig J, Blasco G, Alberich-Bayarri A, Schlaug G, Deco G, Biarnes C, Navas-Martí M, Rivero M, Gich J, Figueras J et al. 2018. Resting-state functional connectivity magnetic resonance imaging and outcome after acute stroke. *Stroke*. 49:2353–2360.

Raichle ME, MacLeod AM, Snyder AZ, Powers WJ, Gusnard DA, Shulman GL. 2001. A default mode of brain function. *Proc Natl Acad Sci U S A*. 98:676–682.

Raichle ME, Snyder AZ. 2007. A default mode of brain function: a brief history of an evolving idea. *Neuroimage*. 37:1083–1090.

Reuter-Lorenz PA, Cappell KA. 2008. Neurocognitive aging and the compensation hypothesis. *Curr Dir Psychol Sci*. 17:177–182.

Saad ZS, Gotts SJ, Murphy K, Chen G, Jo HJ, Martin A, Cox RW. 2012. Trouble at rest: how correlation patterns and group differences become distorted after global signal regression. *Brain Connect*. 2:25–32.

Shen X, Tokoglu F, Papademetris X, Constable RT. 2013. Group-wise whole-brain parcellation from resting-state fMRI data for network node identification. *Neuroimage*. 82:403–415.

Sporns O. 2013. Network attributes for segregation and integration in the human brain. *Curr Opin Neurobiol*. 23:162–171.

Sporns O, Tononi G, Kötter R, O'Neill M, Young M. 2005. The human connectome: a structural description of the human brain. *PLoS Comput Biol*. 1:e42.

Spreng RN, Stevens WD, Viviano JD, Schacter DL. 2016. Attenuated anticorrelation between the default and dorsal attention networks with aging: evidence from task and rest. *Neurobiol Aging*. 45:149–160.

Tagliazucchi E, Balenzuela P, Fraiman D, Chialvo DR. 2012. Criticality in large-scale brain dynamics unveiled by a novel point process analysis. *Front Physiol*. 3:15.

Tian L, Li Q, Wang C, Yu J. 2018. Changes in dynamic functional connections with aging. *Neuroimage*. 172:31–39.

Tognoli E, Kelso JA. 2014. The metastable brain. *Neuron*. 81:35–48.

Turner GR, Spreng RN. 2015. Prefrontal engagement and reduced default network suppression co-occur and are dynamically coupled in older adults: the default-executive coupling hypothesis of aging. *J Cogn Neurosci*. 27:2462–2476.

United Nations, Department of Economic and Social Affairs, Population Division. 2020. *World Population Ageing 2019 (ST/ESA/SER.A/444)*.

van den Heuvel MP, Hulshoff Pol HE. 2010. Exploring the brain network: a review on resting-state fMRI functional connectivity. *Eur Neuropsychopharmacol*. 20:519–534.

van den Heuvel MP, Kahn RS, Goñi J, Sporns O. 2012. High-cost, high-capacity backbone for global brain communication. *Proc Natl Acad Sci U S A*. 109:11372–11377.

van den Heuvel MP, Sporns O. 2011. Rich-club organization of the human connectome. *J Neurosci*. 31:15775–15786.

Wang J, Wang L, Zang Y et al. 2009. Parcellation-dependent small-world brain functional networks: a resting-state fMRI study. *Hum Brain Mapp*. 30:1511–1523.

Wang L, LaViolette P, O'Keefe K, Putcha D, Bakkour A, Van Dijk KR, Pihlajamäki M, Dickerson BC, Sperling RA. 2010. Intrinsic connectivity between the hippocampus and posteromedial cortex predicts memory performance in cognitively intact older individuals. *Neuroimage*. 51:910–917.

Whitfield-Gabrieli S, Nieto-Castanon A. 2012. Conn: a functional connectivity toolbox for correlated and Anticorrelated brain networks. *Brain Connect*. 2:125–141.

WHO. 2016. *Proposed working definition of an older person in Africa for the MDSProject*. World Heal Organ. https://www.who.int/healthinfo/survey/ageingdefnol.

Wong CW, Olafsson V, Tal O, Liu TT. 2013. The amplitude of the resting-state fMRI global signal is related to EEG vigilance measures. *Neuroimage*. 83:983–990.

Xia Y, Chen Q, Shi L, Li M, Gong W, Chen H, Qiu J. 2019. Tracking the dynamic functional connectivity structure of the human brain across the adult lifespan. *Hum Brain Mapp*. 40:717–728.

Yan CG, Craddock RC, Zuo XN, Zang YF, Milham MP. 2013. Standardizing the intrinsic brain: towards robust measurement of inter-individual variation in 1000 functional connectomes. *Neuroimage*. 80:246–262.

Yin D, Liu W, Zeljic K, Wang Z, Lv Q, Fan M, Cheng W, Wang Z. 2016. Dissociable changes of frontal and parietal cortices in inherent functional flexibility across the human life span. *J Neurosci*. 36:10060–10074.

Ystad M, Hodneland E, Adolfsdottir S, Haász J, Lundervold AJ, Eichele T, Lundervold A. 2011. Cortico-striatal connectivity and cognition in normal aging: a combined DTI and resting state fMRI study. *Neuroimage*. 55:24–31.

Zalesky A, Fornito A, Harding IH, Cocchi L, Yücel M, Pantelis C, Bullmore ET. 2010. Whole-brain anatomical networks: does the choice of nodes matter? *Neuroimage*. 50:970–983.

Zalesky A, Fornito A, Cocchi L, Gollo LL, Breakspear M. 2014. Time-resolved resting-state brain networks. *Proc Natl Acad Sci U S A*. 111:10341–10346.

Zhao T, Cao M, Niu H, Zuo XN, Evans A, He Y, Dong Q, Shu N. 2015. Age related changes in the topological organization of the white matter structural connectome across the human lifespan. *Hum Brain Mapp*. 36:3777–3792.

Zuo XN, Di Martino A, Kelly C, Shehzad ZE, Gee DG, Klein DF, Castellanos FX, Biswal BB, Milham MP. 2010. The oscillating brain: complex and reliable. *Neuroimage*. 49:1432–1445.

4.3 Article 3

Authors: Escrichs, A., Sanz Perl, Y., Martínez-Molina, N., Biarnes, C., Garre-Olmo, J., Fernández-Real, J. M., Ramos, R., Martí, R., Pamplona, R., Brugada, R., Serena, J,. Ramió-Torrentà, L., Coll-De-Tuero, G., Gallart, L., Barretina, J., Vilanova, J. C., Mayneris-Perxachs, J., Saba, L., Pedraza, S., Kringelbach, M. L., Puig, J., and Deco, G.

OXFORD

The effect of external stimulation on functional networks in the aging healthy human brain

Anira Escrichs[1,*], Yonatan Sanz Perl[1], Noelia Martínez-Molina[1], Carles Biarnes[2,3], Josep Garre-Olmo[3,4,5],

José Manuel Fernández-Real[3,4,6], Rafel Ramos[3,4,7,8], Ruth Martí[3,7,8], Reinald Pamplona[9], Ramon Brugada[3,4,10], Joaquin Serena[3,4,11],

Lluís Ramió-Torrentà[3,4,11], Gabriel Coll-De-Tuero[4,7,12], Luís Gallart[13], Jordi Barretina[3], Joan C. Vilanova[2,3,4], Jordi Mayneris-Perxachs[3,6],

Luca Saba[14], Salvador Pedraza[2,3,4], Morten L. Kringelbach[15,16,17], Josep Puig[2,3,4,5], Gustavo Deco[1,18,19,20,*]

[1]Computational Neuroscience Group, Center for Brain and Cognition, Department of Information and Communication Technologies, Universitat Pompeu Fabra, Barcelona, Catalonia, Spain,
[2]Department of Radiology (IDI), Hospital Universitari de Girona Dr Josep Trueta, Girona, Spain,
[3]Girona Biomedical Research Institute (IDIBGI), Hospital Universitari de Girona Dr Josep Trueta, Girona, Spain,
[4]Department of Medical Sciences, School of Medicine, University of Girona, Girona, Spain,
[5]Institut d'Assistència Sanitària, Salt, Girona, Spain,
[6]Department of Diabetes, Endocrinology and Nutrition, IDIBGI, Hospital Universitari de Girona Dr Josep Trueta, and CIBER Fisiopatología de la Obesidad y Nutrición (CIBERobn), Girona, Spain,
[7]Vascular Health Research Group of Girona (ISV-Girona), Institut Universitari d'Investigació en Atenció Primària Jordi Gol (IDIAP Jordi Gol), Girona, Spain,
[8]Primary Care Services, Catalan Institute of Health (ICS), Girona, Spain,
[9]Department of Experimental Medicine, Faculty of Medicine, University of Lleida-IRBLleida, Lleida, Spain,
[10]Cardiovascular Genetics Center, IDIBGI, CIBER-CV, Girona, Spain,
[11]Department of Neurology, Hospital Universitari de Girona Dr Josep Trueta, Girona, Spain,
[12]CIBER of Epidemiology and Public Health (CIBERESP), Madrid, Spain,
[13]Biobanc, Girona Biomedical Research Institute (IDIBGI), Girona, Spain,
[14]Department of Radiology, AOU Cagliari, University of Cagliari, Italy,
[15]Centre for Eudaimonia and Human Flourishing, University of Oxford, Oxford, UK,
[16]Department of Psychiatry, University of Oxford, Oxford, UK,
[17]Center for Music in the Brain, Department of Clinical Medicine, Aarhus University, Aarhus, Denmark,
[18]Institució Catalana de la Recerca i Estudis Avancats (ICREA), Barcelona, Catalonia, Spain,
[19]Department of Neuropsychology, Max Planck Institute for human Cognitive and Brain Sciences, Leipzig, Germany,
[20]Turner Institute for Brain and Mental Health, Monash University, Melbourne, VIC, Australia
*Corresponding author: Corresponding authors: anira.escrichs@upf.edu (AE), gustavo.deco@upf.edu (GD)

Abstract

Understanding the brain changes occurring during aging can provide new insights for developing treatments that alleviate or reverse cognitive decline. Neurostimulation techniques have emerged as potential treatments for brain disorders and to improve cognitive functions. Nevertheless, given the ethical restrictions of neurostimulation approaches, *in silico* perturbation protocols based on causal whole-brain models are fundamental to gaining a mechanistic understanding of brain dynamics. Furthermore, this strategy could serve to identify neurophysiological biomarkers differentiating between age groups through an exhaustive exploration of the global effect of all possible local perturbations. Here, we used a resting-state fMRI dataset divided into middle-aged ($N = 310$, <65 years) and older adults ($N = 310$, ≥65) to characterize brain states in each group as a probabilistic metastable substate (PMS) space. We showed that the older group exhibited a reduced capability to access a metastable substate that overlaps with the rich club. Then, we fitted the PMS to a whole-brain model and applied *in silico* stimulations in each node to force transitions from the brain states of the older- to the middle-aged group. We found that the precuneus was the best stimulation target. Overall, these findings could have important implications for designing neurostimulation interventions for reversing the effects of aging on whole-brain dynamics.

Key words: aging; computational modeling; resting-state fMRI; brain states; *in silico* perturbations.

Introduction

Normal aging causes changes in the brain that can lead to cognitive decline, thereby affecting the quality of life and autonomy of the elderly and their caregivers (Barnes 2011; Li et al. 2015). Longitudinal studies in healthy older adults have shown an association between altered functional connectivity in resting-state and decreased cognitive functions (Persson et al. 2014; Fjell et al. 2017), thus suggesting that the resting-state could be an indicator of age-related cognitive decline. In addition, various neuroimaging studies have described that aging affects several resting-state networks (Wang et al. 2010; Ferreira and Busatto, 2013; Betzel et al. 2014; Grady et al. 2016; Spreng et al. 2016)

and the rich-club organization of the human brain (Cao et al. 2014; Zhao et al. 2015; Damoiseaux 2017; Escrichs et al. 2021a). However, a question that remains to be addressed is whether these effects could be reversed or alleviated with external stimulation protocols that promote transitions from the brain states of the older toward those observed in younger adults.

The study of causal structure-function inferences has enhanced the understanding of the mechanisms underlying human brain dynamics, both through direct neurostimulation techniques (Casali et al. 2013; Ozdemir et al. 2020) and by *in silico* stimulation protocols (Muldoon et al. 2016; Deco et al. 2018, 2019; Bolton et al. 2020; Kringelbach and Deco 2020). Noninvasive neurostimulation techniques such as transcranial electrical stimulation (tES) and transcranial magnetic stimulation (TMS) combined with neuroimaging have provided novel insights into the underlying mechanisms of stimulation-induced effects along with its impact on large-scale functional brain networks (Bestmann and Feredoes 2013). These approaches have emerged as potential treatments for neurological and neurodegenerative disorders (Fox et al. 2014; Kunze et al. 2016) as well as for improving cognitive function in healthy individuals (Clark and Parasuraman 2014). Nevertheless, experimental and ethical constraints limit the exploration of efficient practices that could be improved by the inclusion of whole-brain computational approaches along with *in silico* perturbations. In particular, dynamical models of brain activity have been fitted to different brain states to systematically apply *in silico* perturbations that promote transitions between brain states and, consequently, predict optimal neurostimulation targets (Muldoon et al. 2016; Deco et al. 2019; Ipiña et al. 2020). This strategy allows exploring dynamical brain responses elicited by controlled perturbative protocols, which are not constrained by ethical limitations (Deco et al. 2017).

In this context, we postulate that causal whole-brain modeling along with *in silico* stimulations can promote the transition between brain states of different age groups characterized by their dynamical behavior where the external stimulation represents the perturbation needed to induce that transition. The first step to finding support for this interpretation is to define the brain states associated with aging through their underlying dynamical behavior, thus providing a quantitative characterization. The probability metastable substates (PMS) space emerges as an optimal space to describe this dynamical behavior as the time evolution of a set of metastable states obtained within the Leading Eigenvector Dynamical Analysis (LEiDA) (Cabral et al. 2017; Deco et al. 2019; Kringelbach and Deco 2020). The LEiDA framework has allowed discerning brain states in depression (Figueroa et al. 2019), different states of consciousness (Deco et al. 2019; Lord et al. 2019; Kringelbach and Deco 2020; Kringelbach and Deco, 2020), and healthy aging (Cabral et al. 2017). The second step to support our hypothesis involves the transition

from the older subjects' PMS representation to the youngest one induced by *in silico* perturbations. This can be done through whole-brain models, which link the underlying anatomical connectivity with functional dynamics obtained from neuroimaging data, in which the external stimulation of all brain areas can be systematically explored via *in silico* perturbations by adjusting the parameters of the model (Deco et al. 2018, 2019; Kringelbach and Deco 2020). In other words, the empirical LEiDA approach obtains the PMS of each group, whereas the model-based *in silico* approach allows us to simulate the PMS space of the older group and artificially perturb each brain area to induce transitions towards the PMS of the middle-age group. This mechanistic approach allows for an effective way of perturbing the model by simply changing the bifurcation parameter in a given brain area.

We have recently shown (Escrichs et al. 2021a) significant differences in the PMS space between older- and middle-aged healthy adults. Going radically beyond our previous work, which provided important model-free information on the differences given by the dynamics, here we used a causal whole-brain model to provide mechanistic information on how to reverse age-induced changes in dynamics. We hypothesized that a physiological differentiation of the neuronal substrate underlying the older- and middle-aged groups could be obtained by assessing, through external stimulations, the capability of each brain region to promote a transition from the brain states characterizing the older group towards the brain states characterizing the middle-aged group. Beyond the differentiation, this approach would also allow the selection of optimal stimulation targets to rebalance the underlying brain dynamics in the elderly towards more healthy states. In particular, we fit the PMS of the older group by using a causal mechanistic whole-brain model (Deco et al. 2019; Kringelbach and Deco 2020) and study exhaustively *in silico* , i.e. region by region, how to force a transition from the brain states associated with the older group to the brain states of the middle-aged group.

Materials and methods
Participants
Neuroimaging data were obtained from the Aging Imageomics Study (Puig et al. 2020) and comprised 620 healthy adults divided into two groups. The middle-aged group comprised 310 subjects aged < 65 years (mean age, 60.2±3.7 years), and the older group comprised 310 subjects aged >= 65 years (mean age, 71.8±4.5 years). We set the cut-off age based on the definition of the elderly as those people aged 65 and above (WHO 2016; United Nations, 2019). The experimental protocol was approved by the Ethics Committee of the Dr Josep Trueta University Hospital. Written informed consent was obtained from all participants. A complete description of the neuroimaging data can be consulted in Puig et al. (2020) and Escrichs et al. (2021a).

Resting-state acquisition and preprocessing

Imaging was performed on a mobile 1.5T scanner (Vantage Elan, Toshiba Medical Systems) with an 8-channel phased-array head coil with foam padding and headphones to restrict head motion and scanner noise. The high-resolution T1-weighted images were acquired with 112 slices in the axial plane (repetition time [TR] = 8 ms; echo time [TE] = 4.5 ms; flip angle = 15°; field of view (FOV) = 235 mm; and voxel size = 1.3 × 1.3 × 2.5 mm). Resting-state functional magnetic resonance imaging (fMRI) scans were acquired axially for 5 min using a gradient Echo-planar imaging (EPI) sequence (122 volumes; TR = 2500 ms; TE = 40 ms; flip angle = 83°; FOV = 230 mm; voxel size = 3.5 × 3.5 × 5 mm; no gap). Participants were asked to remain motionless as possible and close their eyes.

T1 and EPI images were automatically oriented using Conn (Whitfield-Gabrieli and Nieto-Castanon 2012). Processing Assistant for Resting-State fMRI (DPARSF) [(Chao-Gan and Yu-Feng 2010), www.rfmri.org/DPARSF], which is based on Statistical Parametric Mapping (SPM12) (http://www.fil.ion.ucl.ac.uk/spm) was used to preprocess the fMRI data. Preprocessing steps included: discarding the first 5 volumes from each scan to allow for signal stabilization; slice-timing correction; realignment for head motion correction across different volumes; T1 co-registration to the functional image; European regularisation segmentation; removal of spurious variance through linear regression: 6 parameters from the head motion correction, the white matter signal, and the cerebrospinal fluid signal using CompCor (Behzadi et al. 2007); removal of the linear trend; spatial normalization to the Montreal Neurological Institute standard space; spatial smoothing with 6-mm Full Width at Half Maximum Gaussian Kernel; and bandpass temporal filtering (0.01–0.020 Hz). Finally, the time series for each subject were extracted using a resting-state atlas of 214 nodes (Shen et al. 2013).

Difussion Tensor Imaging acquisition and preprocessing

For the whole-brain model, we used an average structural connectivity matrix (SC) from a sample of 38 unrelated healthy subjects previously described in De Filippi et al. (2021). MRI images were acquired on a 3T whole-body Siemens TRIO scanner (Hospital Clínic, Barcelona) using a dual spin-echo difussion tensor imaging (DTI) sequence (TR = 680ms; TE = 92ms; FOV = 236mm; 60 contiguous axial slices; isotropic voxel size 2 × 2 × 2 mm; no gap, and 118 × 118 matrix sizes). Diffusion was obtained with 64 optimal noncollinear diffusion directions using a single b value = 1500s/mm^2 interleaved with 9 nondiffusion b0 images. A frequency-selective fat saturation pulse was used to avoid chemical shift misregistration artifacts.

The whole-brain SC matrix was computed following the procedure applied in previous studies (Gong et al. 2009; Cao et al. 2013; Muthuraman et al. 2016;

López-González et al. 2021). For each subject, a 214×214 SC was computed using the processing pipeline of the FMRIB's Diffusion Toolbox (FDT) in FMRIB's Software Library www.fmrib.ox.ac.uk/fsl. Nonbrain tissues were extracted with Brain Extraction Tool (Smith, 2002), eddy current distortions and head motion were corrected using eddy correct (Andersson and Sotiropoulos 2016), and the gradient matrix was reoriented to correct for subject motion (Leemans and Jones, 2009). Crossing fibres were modeled using BEDPOSTX, and the probability of multi-fibre orientations was computed to improve the sensitivity of nondominant fibre populations (Behrens et al. 2003, 2007). The probabilistic tractography analysis was performed for each participant in native diffusion space using PROBTRACKX. The connectivity probability SC_{np} between brain areas n and p was calculated as the total proportion of sampled fibres in all voxels in brain area n that reach any voxel in brain area p. The SC_{np} matrix was then symmetrized by computing their transpose matrix SC_{pn} and averaging both matrices. Finally, averaging the resulting matrices across all participants, a whole-brain SC matrix was obtained, representing a template of healthy adults.

Leading Eigenvector Dynamics Analysis

We characterized the empirical brain states by applying the LEiDA (Cabral et al. 2017; Deco et al. 2019; Kringelbach and Deco 2020). This analysis was described in our previous study using the same resting-state fMRI dataset (Escrichs et al. 2021a). For each participant, we filtered the time series within the narrowband 0.04–0.07 Hz (Glerean et al. 2012) and computed the Hilbert transform to obtain the phase of the BOLD signals in every time-point for all brain areas of the resting-state parcellation (Fig. 1A). Then, we computed a dynamic phase coherence connectivity matrix with size NxNxT, where N=214 is the total brain areas, and T=117 the total time-points. The BOLD phase coherence matrix or dynamic functional connectivity (dFC) (Fig. 1B) in each time t between each pair of brain areas n and p was estimated by computing the cosine of the phase difference as:

$$dFC(n, p, t) = \cos(\theta(n, t) - \theta(p, t)) \tag{1}$$

Given that the Hilbert Transform expresses any signal in the polar coordinate system (i.e. $x_a(t) = A(t) \cdot \cos(\varphi(t))$), applying the cosine function to brain areas n and p with similar angles at a given time t will show a phase coherence close to 1 (i.e. cos(0°)=1), whereas brain areas showing orthogonality will show a phase coherence near zero (i.e. cos(90°) = 0) (Deco et al. 2019). Second, to characterize the dFC patterns across all subjects and time-points, we obtained a leading eigenvector $V_1(t)$ for each dFC(t) at time t by capturing the dominant functional connectivity pattern rather than the whole matrices. This approach allows to reduce dimensionality on the data considerably given that only considers a $V_1(t)$ for each dynamic FC matrix. The $V_1(t)$ is a Nx1
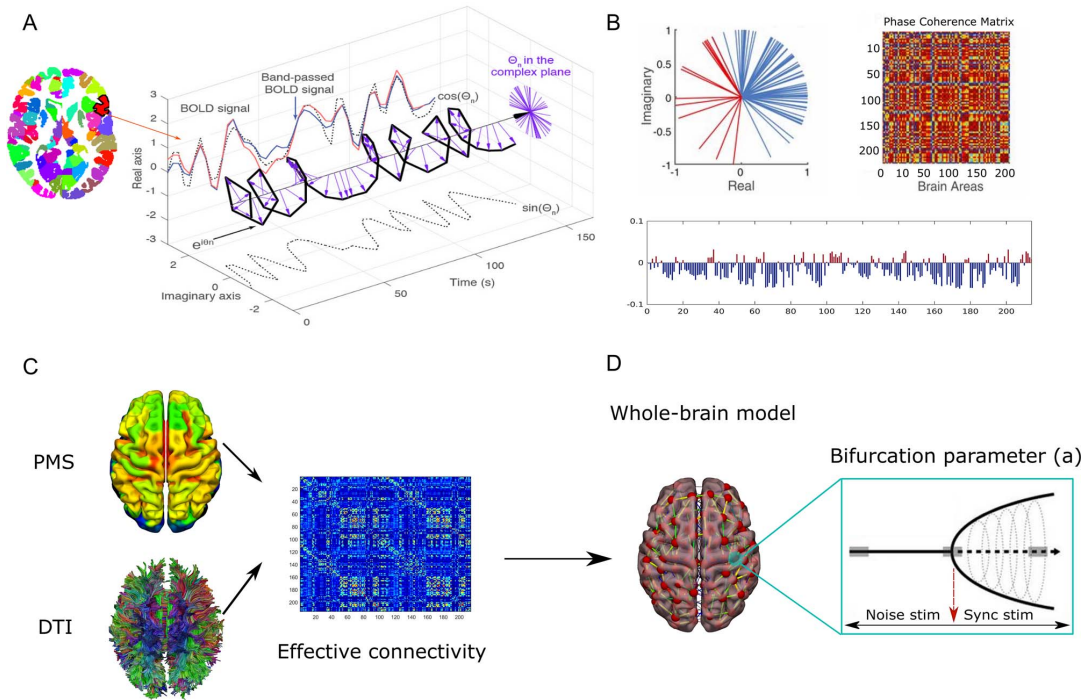
Fig. 1. PMS space, optimizing the model for whole-brain activity and *in silico* stimulations. (A) We extracted the time series using a resting-state atlas of 214 nodes and measured the Hilbert transform for each brain area. The panel shows a complex plane representing the BOLD phases for a given brain area across time. (B) Leading Eigenvector Dynamic Analysis (LEiDA) to identify dynamic functional connectivity patterns across all subjects [i.e. probabilistic metastable substates (PMS)]. The left panel shows the BOLD phases in all 214 brain areas described in the complex plane. The right panel shows the phase coherence matrix between each pair of brain areas in all time points. The vector shows the leading eigenvector $V_1(t)$, capturing the principal orientation of the BOLD phase (showing positive or negative values) for each of the 214 brain areas. (C) Whole-brain PMS model. A whole-brain dynamical model was fitted for the PMS of the older group based on the effective connectivity. (D) Stimulations *in silico* . Each brain area of the whole-brain model was systematically perturbed via *in silico* stimulations through two different protocols (noise and synchronization). The noise protocol shifts the local bifurcation parameter of each brain area to negative values, whereas the synchronization protocol shifts it to positive. Figure A and B adapted from (Deco et al. 2018; Escrichs et al. 2021a).

vector capturing the principal orientation of the BOLD phase (showing positive or negative values) for each of the 214 brain areas (Fig. 1B, lower panel). Next, we applied a k-means clustering algorithm ranged from $k = 2$ to $k = 7$ clusters to detect metastable substates or dynamic FC states from all the leading eigenvectors $V_1(t)$ across time-points, number of subjects, and groups to identify recurrent dynamic FC patterns across subjects. The total of leading eigenvectors were 117 time-points × 310 subjects × 2 groups = 72 540 $V_1(t)$. We obtained k cluster centroids, each one as an Nx1 vector representing recurrent metastable substates across all participants. The resulting k-cluster centroids define the metastable substates among which the brain dynamics are switching across time, and the probability of occurrence of each substate determines the PMS of the brain.

Whole-brain computational model

The whole-brain BOLD activity was simulated using the so-called Hopf computational model, linking the anatomy and function. The model consisted of 214 dynamical cortical and subcortical brain areas coupled with the SC matrix. The local dynamics of each brain area was described by the normal form of a supercritical Hopf bifurcation, which emulates the dynamics for each brain area from noisy to oscillatory dynamics as follows:

$$\frac{dx_n}{dt} = [a_n - x_n^2 - y_n^2]x_n - \omega_n y_n + G\sum_{P=1}^{N} C_{np}(x_p - x_n) + \beta\eta_n(t)$$

$$\frac{dy_n}{dt} = [a_n - x_n^2 - y_n^2]y_n + \omega_n x_n + G\sum_{P=1}^{N} C_{np}(y_p - y_n) + \beta\eta_n(t)$$

$$(2)$$

where $\eta_n(t)$ is additive Gaussian noise with standard deviation $\beta = 0.02$, and C_{np} is the SC that couples the local dynamics of brain area n with p and was normalized to a maximum value of $C = 0.2$. This normal form has a supercritical bifurcation at $a_n = 0$, such that for $a_n > 0$ the system is in a stable limit cycle oscillation with frequency $f_n = \omega_n/2\pi$, whereas for $a_n < 0$ the local dynamics are in a stable point (i.e. noisy state). The frequency ω_n of each brain area was estimated from the data that were given by the applied narrowband (i.e. $0.04 - 0.07 Hz$). The variables x_n emulate the BOLD

signal of each node j. The global coupling factor G (scaled equally for each brain area) is the control parameter that allows adjusting the model to obtain the optimal dynamical working point where the simulations maximally fit the empirical data. We simulated the PMS as a function of the global coupling parameter G through the underlying SC matrix. We improved the fitting of the whole-brain model through the inclusion of the effective connectivity (EC) (Fig. 1C), where the anatomical connectivity was updated by the synaptic weights that take into account the empirical functional connectivity. The effective connections were computed by measuring the distance between the empirical $FC_{ij}^{phases\_emp}$ and the model $FC_{ij}^{phases\_mod}$ grand-averaged phase coherence matrices, and adjusted each structural connection ij separately using a gradient-descent approach. The model initially started computing with the SC matrix obtained from DTI and was run repeatedly with the updated EC matrix until the fit converged toward a stable value using the following procedure:

$$C_{ij} = C_{ij} + \epsilon \left(FC_{ij}^{phases\_emp} - FC_{ij}^{phases\_mod} \right) \tag{3}$$

where $\epsilon = 0.01$, and the grand average phase coherence matrices were defined as:

$$FC_{ij} = \left\langle \cos \left(\varphi_j(t) - \varphi_i(t) \right) \right\rangle \tag{4}$$

where $\varphi(t)$ corresponds to the BOLD signal phase (obtained by the Hilbert transform) of the brain areas j and i at time t, and the brackets correspond to the average across time.

Perturbation of the whole-brain model

The perturbation of the whole-brain model consisted of systematically perturbing the 214 brain areas of the model using two different protocols (noise and synchronization). The perturbations were based on shifting the local bifurcation parameter (a) of the optimized model (Fig. 1D). The noise (synchronization) protocol applies negative (positive) intensities to the local parameter from 0 to -0.3 (0.1).

Comparing empirical and simulated probability metastable space states

The empirical and simulated brain states were compared by using a symmetrized KL distance between the simulated and empirical probabilities as:

$$KL(P_{emp}, P_{sim}) = 0.5 \left(\sum_i P_{emp}(i) \ln \left(\frac{P_{emp}(i)}{P_{sim}(i)} \right) \right.$$
$$\left. + \sum_i P_{sim}(i) \ln \left(\frac{P_{sim}(i)}{P_{emp}(i)} \right) \right) \tag{5}$$

where $P_{emp}(i)$ are the empirical and $P_{sim}(i)$ the simulated probabilities on the same empirical extracted brain states i. The optimal simulated PMS is defined by the minimum KL distance between the empirical and simulated PMS.

Results

Leading Eigenvector Dynamics Analysis

As a proof-of-concept, we show the minimum number of clusters (k) that statistically differed between groups. In particular, the clustering configuration that best represented the resting-state data across all participants and distinguished between both groups was detected at k=3. In Figure 2A, we display the cluster centroid vectors onto the surface cortex. Interestingly, the regions of the second metastable substate showing positive values overlap with the brain's rich-club organization of the human brain (i.e. precuneus, insula, and subcortical areas, such as the caudate, putamen, hippocampus, and thalamus) (Hagmann et al. 2008; Sporns, 2013; van den Heuvel and Sporns, 2011) as found in our previous empirical study (Escrichs et al. 2021a). The probability of occurrence for the PMS of each group is shown in Fig. 2B, left panel. Specifically, the probability of the first metastable substate occurrence was higher in the older group than in the middle-age group [0.476 ± 0.008 (mean ± SE) vs. 0.453 ± 0.008 False discovery rate (FDR)-corrected, P=0.03]. By contrast, the second metastable substate's probability was higher in the middle-age group [0.288 ± 0.007 vs. 0.269 ± 0.006 in the older group, False discovery rate (FDR) P= 0.026].

Finally, we correlated the PMS values of the relevant metastable substate (i.e. rich club) with age. We found a negative correlation showing that the capability to access this state decreases while the age increases [$r(618) = -.08r, P = 0.04$]. However, even though the correlation is significant, the slope value is marginal. This result indicates the effectiveness of our method to find significant differences at the group level but not at the subject level.

Fit whole-brain computational model to the brain states of the older group

For the older group, we constructed a dynamical model of 214 nonlinear oscillators representing the macroscopic dynamical behavior of each brain area of interest (Fig. 2B, middle panel). These oscillators are coupled by a SC matrix among brain areas giving rise to collective dynamics. The local dynamics of each brain area was described by the normal form of a supercritical Hopf bifurcation, and the bifurcation parameters of each oscillator (a) were set in the edge of the bifurcation point, i.e. the optimal point to represent the metastability of brain states (Deco et al. 2017). The coupling strength parameter (G) was optimized to fit the whole-brain model to the PMS of the older group. In particular, we used the centroids of the empirical PMS of the older group and built the model based on the probability of the empirical centers. Then, we estimated the distance between the model and the empirical phase coherence matrices and adjusted
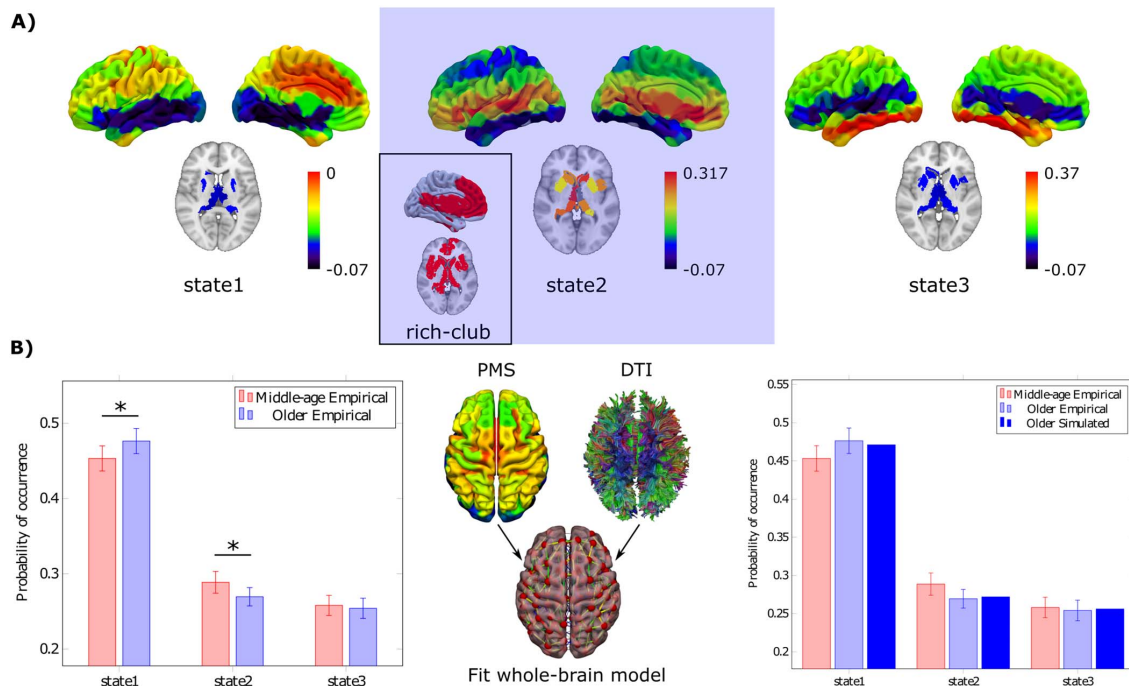
Fig. 2. Empirical PMS and whole-brain model fitting. (A) The clustering configuration that best represented our resting-state fMRI data across subjects was found for 3 states. Rendered brains show the states onto the cortex. State 1 shows negative values in all regions of the leading eigenvector. Regions showing positive values in state 2 overlap with the rich club network (precuneus, insula, caudate, putamen, hippocampus, and thalamus). State 3 was not statistically different between groups. Color bars represent the principal orientation of the BOLD phase from the leading eigenvector (showing positive o negative values). (B) The left panel shows each state and group's mean probability of occurrence, while error bars represent the 95% confidence interval. The probability of occurrence in the first state was higher in the older group. By contrast, the probability of occurrence in the second state was higher in the middle-age group. The whole-brain model was fitted to the empirical PMS of the older group (middle panel). The right panel shows the resulting model (electric blue), remarkably similar to their empirical version (blue). P-values are based on Monte-Carlo permutation tests, ∗ represents P<0.05.

each structural connection separately using a gradient-descent algorithm. The model was run repeatedly with the updated EC until convergence to a stable point. We tested the differences between the empirical and the simulated probabilities by computing the symmetrized Kullback–Leibler (KL) distance (see Material and methods). The optimal working point of the model was found at G=0.02, i.e. where the model fits the empirical PMS data of the older group. The generated model reached an excellent fit between the empirical and the simulated probabilities (Fig. 2B, right panel).

In silico stimulations to force transitions between brain states

We applied two different stimulation protocols (i.e. noise and synchronization) in order to force transitions from the PMS of the older group to the PMS of the middle-aged group. In Figure 3A, we show the schematic procedure to force transitions between brain states. Specifically, we started from the simulated PMS that presented the highest similarity to the empirical PMS of the older group and perturbed the model to force the transition to the empirical PMS of the middle-age group. The stimulation protocols were based on systematically shifting the local

bifurcation parameter (*a*) of the optimized whole-brain model. The noise protocol applies negative intensities to the local parameter, whereas the synchronization applies positive intensities. The strength of the perturbation is linked to the shifting of the local bifurcation parameter. Concretely, we systematically perturbed each of the 214 brain areas of the whole-brain model and compared the distributions with the empirical PMS of the middle-age group. The optimal perturbation is that yields that the first brain state decreases, the second increases and the third brain state remains similar (Fig. 3A, right panel).

Our results show that the KL distances between the empirical PMS of the middle-aged group and the perturbed model were minimal in some brain areas for the noise protocol, and thus a good transition between brain states was obtained (Fig. 3B, left panel). The potential brain areas to achieve a good transition between brain states were the precuneus and lingual gyrus, bilateral middle temporal gyrus, bilateral calcarine sulcus, bilateral inferior gyrus orbitofrontal part, left superior temporal gyrus, left insula, bilateral putamen, bilateral thalamus, and right caudate (Fig. 3B, middle panel). In contrast, the KL distances were higher in the synchronization protocol for all perturbation strengths
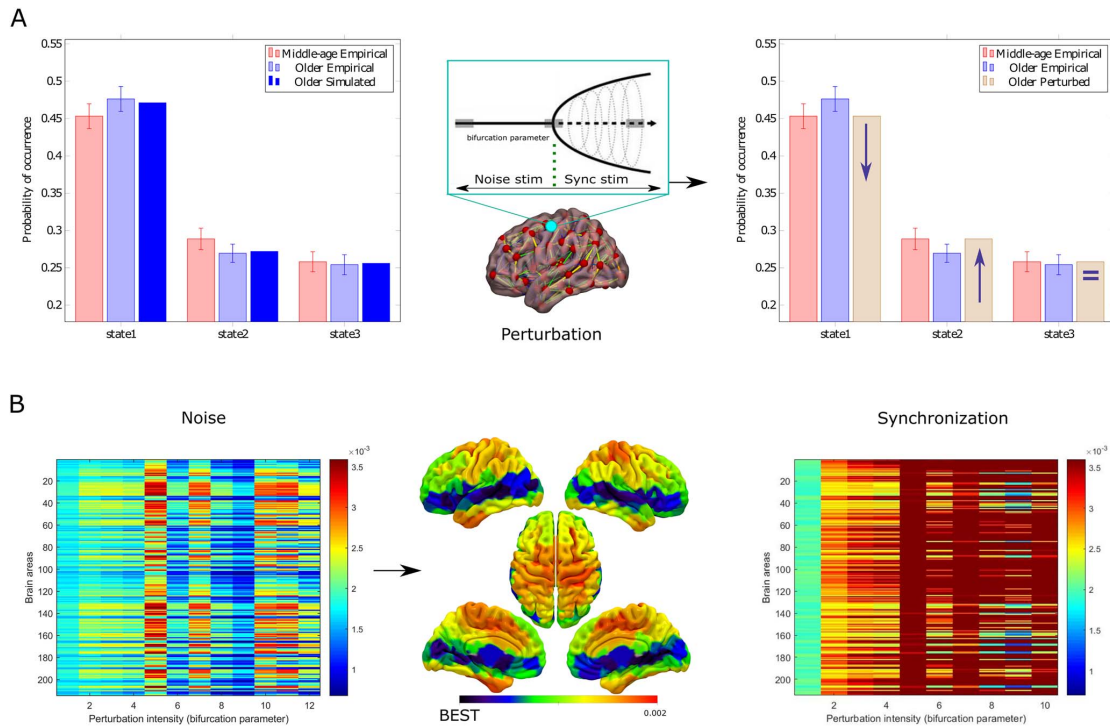
Fig. 3. Noise and synchronization stimulation protocols. (A) Forcing transitions from the model of the older group (electric blue) to the empirical PMS of the middle-age group (red). The whole-brain model was perturbed at the optimal working point using two different protocols (noise and synchronization), which shifted the local bifurcation parameter to negative and positive values, respectively (middle panel). The optimal perturbation is that which achieves the first state decreases, the second state increases, and the third state remains similar (right panel). (B) The left matrix shows the KL-distance value after applying the noise protocol's perturbation intensity (from softer to stronger) in each brain area. This protocol presented the best effectiveness since KL distances were minimal in some brain areas. The brain rendered onto the cortex shows that the optimal brain areas to induce the transitions were the precuneus and lingual gyrus, bilateral middle temporal gyrus, bilateral calcarine sulcus, bilateral inferior gyrus orbitofrontal part, left superior temporal gyrus, left insula, bilateral putamen, bilateral thalamus, and right caudate. The color scale represents the KL distance between the PMS of the middle-age group and the perturbed model using the noise protocol. The right matrix shows that the synchronization protocol presented poor effectiveness given that KL distances were longer than in the noise protocol.

and perturbed brain areas (Fig. 3B, right panel). This result indicates the unsuitability of the synchronization protocol to force the transition.

Finally, in Figure 4 we display the PMS comparison between empirical, modeled, and perturbation conditions. We show the best transition and the worst transition after the perturbation. It is noticeable that after perturbing the precuneus, the probabilities of the empirical PMS of the middle-aged group and perturbed model of the older group are almost the same for the three metastable substates considered (the KL distance was minimal). By contrast, the worst target was the postcentral gyrus, since the probabilities of the states barely changed after the perturbation. These results suggest that the right precuneus is the brain area that induces the best effective transition between brain states.

Discussion

In this work, we used empirical and computational approaches to study the causal dynamical mechanisms allowing the transition between brain states of different age groups. Our empirical approach identified that the older group has a lower probability of accessing a state that overlaps with the rich club. Then, we investigated the effect of perturbing all brain areas to induce optimal transitions from the states of the older aged group to the states of the middle-aged group by using causal whole-brain modeling and *in silico* perturbations. These results illustrated that forcing a shift in the intrinsic local dynamics of the right precuneus and other brain areas belonging to the rich club (insula, putamen, caudate, and thalamus) is suitable for inducing those transitions. Crucially, our model-based *in silico* approach provides causal evidence that external stimulations in specific local brain areas can reshape whole-brain dynamics in the aging brain. Importantly, this could provide new insights into the differential sensitivity of each brain area to *in silico* perturbations as a specific model-based biomarker relating local activity with global brain dynamics.

Understanding the underlying brain changes occurring during normal aging can contribute to developing treatments to reverse cognitive impairment. In this regard, Noninvasive neurostimulation therapies stand as a promising intervention for brain disorders (Clark and Parasuraman 2014; Kunze et al. 2016). Nevertheless,
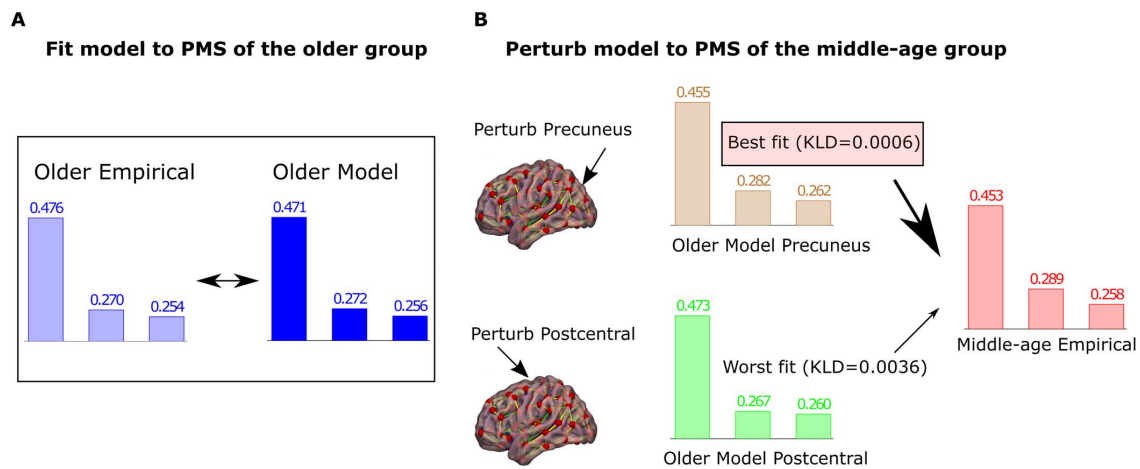
A

Fit model to PMS of the older group

B

Perturb model to PMS of the middle-age group

Fig. 4. PMS comparison between empirical, modeled, and perturbation conditions. (A) Comparison between the probability of occurrence of the empirical and modeled PMS of the older group. (B) We show the best and worst transitions after the perturbation. These results clearly show an optimal transition from the perturbed model towards the PMS of the middle-aged group after changing the bifurcation parameter of the right precuneus with the noise protocol. In particular, this perturbation decreased the probability of occurrence of the first state, increased the probability of the second, and kept the probability of the third similar. By contrast, the postcentral gyrus shows a non-optimal transition since the states' probabilities barely changed after the perturbation.

there are two different but related limitations for the application of such treatments. The first refers to the lack of a consensual definition of a brain state capable of being quantitatively characterized that differentiates the activity of an older from a younger brain. The second issue concerns the limitations to exploring the vast space of possible interventions due to experimental and ethical constraints (Deco et al. 2017). Here, we addressed these 2 issues by applying whole-brain computational models, which allowed us to systematically explore brain responses elicited by *in silico* perturbations of fMRI empirical data of healthy older and middle-aged subjects.

We tested the hypothesis that causal modeling could predict optimal stimulation targets to rebalance the underlying brain dynamics in the elderly. Interestingly, we show that this approach can predict optimal targets to force transitions between brain states of different ages. Previous experimental studies investigated the effects of localized external perturbations during states of reduced awareness in humans (Angelakis et al. 2014; Thibaut et al. 2014; Zhang et al. 2019) and mild cognitive impairment (Hampstead et al. 2017). However, the systematic exploration via perturbations of all brain areas of the human brain can only be performed through computational models that simulate the underlying brain activity (Spiegler et al. 2016). In this direction, recent works have implemented whole-brain models and *in silico* perturbations to explore the elicited responses from external stimulations in different brain states such as sleep, anesthesia, disorders of consciousness and even in altered states such as meditation or the psychedelic state (Deco et al. 2019; Ipiña et al. 2020;

Kringelbach et al. 2020; Sanz Perl et al. 2021; Escrichs et al. 2021b).

Our empirical approach using LEiDA identified PMS differences between older and middle-age groups. In particular, we found differences in a state that closely overlaps with the so-called rich club (Hagmann et al. 2008; van den Heuvel and Sporns, 2011; Sporns, 2013), that in turn, the rich club overlaps with the Default mode network (DMN) (van den Heuvel and Sporns, 2011; Damoiseaux 2017). Our results reveal that, compared with middle-aged subjects, older subjects showed a lower probability of occurrence of this state that can be interpreted as an alteration in the intrinsic dynamics within the rich-club or damage in any of their brain areas involved (Escrichs et al. 2021a). In line with this finding, recent studies have suggested that the alterations in brain dynamics observed in the elderly could be due to a deficiency in the rich-club organization (Cao et al. 2014; Zhao et al. 2015; Damoiseaux 2017). This framework demonstrates that the brain spatiotemporal dynamic, summarized in the PMS, provides crucial information to characterize different aged groups. Furthermore, this result could be related to Northoff and colleagues' proposal about spatiotemporal neuroscience and the common currency between brain and mind (Northoff et al. 2020).

Our model-based *in silico* approach allowed us to test the effectiveness of 2 different stimulation protocols named noise and synchronization. The noise protocol reduces the value of the bifurcation parameter of the stimulated node resulting in noise outweighing oscillatory behavior, whereas the synchronization protocol yields the opposite effect. The fact that the noise protocol

leads to better results means that the local bifurcation parameters must be mostly below or at the edge of bifurcation, thus favoring the local dynamics in the most susceptible regime. Furthermore, this result could be related to brain overactivation that has been largely documented in the elderly. Particularly, older adults show overactivation in frontal brain areas (Davis et al. 2008; Reuter-Lorenz and Cappell, 2008; Cabeza et al. 2018; Yao and Hsieh 2021), and among resting-state networks (Betzel et al. 2014; Geerligs et al. 2015; Spreng et al. 2016; Escrichs et al. 2021a). Thus, one possible mechanism could be that noise stimulation decreases these functional overactivations.

Interestingly, the results show that the brain area that promoted the best transition between brain states was the precuneus. The precuneus plays a central functional role in the DMN (Utevsky et al. 2014) and is involved in complex functions like memory, perception, mental imagery, and responses to pain (Cavanna and Trimble 2006). Furthermore, we found that the other brain areas that promoted an excellent transition are part of the so-called rich club (i.e. the precuneus, insula, putamen, caudate, and thalamus) (van den Heuvel and Sporns, 2011; Van Den Heuvel et al. 2012). Evidence suggests that a disruption in one of these regions can affect network efficiency and global brain function (van den Heuvel and Sporns, 2011).

Lastly, we would like to acknowledge some limitations in the study. One inherent limitation is related to using a cross-sectional approach that, by definition, cannot measure individual changes in brain dynamics. The image acquisition protocol with TR also limits this work = 2.5s in a 1.5T scanner. A protocol with increased spatial and temporal resolution could allow a more accurate representation of the underlying brain dynamics. Furthermore, we did not correlate our empirical PMS results with behavioral or cognitive measures. Future studies could explore the relationship between cognitive assessments with brain dynamics for more clinical relevance. Another limitation concerns the parcellation used, which was based on an atlas of 214 nodes. Using brain atlases with a large number of nodes could produce results with better local sensitivity.

Overall, the model-based *in silico* approach provides causal evidence that external stimulations in specific local brain areas can reshape whole-brain dynamics in aging. From a clinical standpoint, the methods and results presented here suggest optimal targets for neurostimulation techniques to induce transitions toward a healthy regime. This framework could improve the diagnosis, prognosis, and therapeutic responsiveness of aging effects in healthy adults and other conditions such as neuropsychiatry diseases and disorders of consciousness.

Acknowledgments

References

Andersson JL, Sotiropoulos SN. An integrated approach to correction for off-resonance effects and subject movement in diffusion MR imaging. *NeuroImage*. 2016:125:1063–1078.

Angelakis E, Liouta E, Andreadis N, Korfias S, Ktonas P, Stranjalis G, Sakas DE. Transcranial direct current stimulation effects in disorders of consciousness. *Arch Phys Med Rehabil*. 2014:95: 283–289.

Barnes CA. Secrets of aging: what does a normally aging brain look like? *F1000 Biol Rep*. 2011:3:22.

Behrens T, Woolrich M, Jenkinson M, Johansen-Berg H, Nunes R, Clare S, Matthews P, Brady J, Smith S. Characterization and propagation of uncertainty in diffusion-weighted MR imaging. *Magn Reson Med*. 2003:50:1077–1088.

Behrens TEJ, Berg HJ, Jbabdi S, Rushworth MFS, Woolrich MW. Probabilistic diffusion tractography with multiple fibre orientations: What can we gain? *NeuroImage*. 2007:34:144–155.

Behzadi Y, Restom K, Liau J, Liu TT. A component based noise correction method (CompCor) for BOLD and perfusion based fMRI. *NeuroImage*. 2007:37:90–101.

Bestmann S, Feredoes E. Combined neurostimulation and neuroimaging in cognitive neuroscience: Past, present, and future. *Ann N Y Acad Sci*. 2013:1296:11–30.

Betzel RF, Byrge L, He Y, Goñi J, Zuo XNN, Sporns O. Changes in structural and functional connectivity among resting-state networks across the human lifespan. *NeuroImage*. 2014:102: 345–357.

Bolton TA, Morgenroth E, Preti MG, Van De Ville D. Tapping into Multi-Faceted Human Behavior and Psychopathology Using fMRI Brain Dynamics. *Trends Neurosci*. 2020:43:667–680.

Cabeza R, Albert M, Belleville S, Craik FI, Duarte A, Grady CL, Lindenberger U, Nyberg L, Park DC, Reuter-Lorenz PA, et al. Maintenance, reserve and compensation: the cognitive neuroscience of healthy ageing. *Nat Rev Neurosci*. 2018:19:701–710.

Cabral J, Vidaurre D, Marques P, Magalhães R, Silva Moreira P, Miguel Soares J, Deco G, Sousa N, Kringelbach ML. Cognitive performance in healthy older adults relates to spontaneous switching between states of functional connectivity during rest. *Sci Rep*. 2017:7:5135.

Cao Q, Shu N, An L, Wang P, Sun L, Xia MR, Wang JH, Gong GL, Zang YF, Wang YF, et al. Probabilistic diffusion tractography and graph theory analysis reveal abnormal white matter structural connectivity networks in drug-naive boys with attention deficit/hyperactivity disorder. *J Neurosci*. 2013:33: 10676–10687.

Cao M, Wang JHH, Dai ZJJ, Cao XYY, Jiang LLL, Fan FMM, Song XWW, Xia MRR, Shu N, Dong Q, et al. Topological organization of the human brain functional connectome across the lifespan. *Dev Cogn Neurosci*. 2014:7:76–93.

Casali AG, Gosseries O, Rosanova M, Boly M, Sarasso S, Casali KR, Casarotto S, Bruno MA, Laureys S, Tononi G, et al. A theoretically based index of consciousness independent of sensory processing and behavior. *Sci Transl Med*. 2013:5:198ra105–198ra105.

Cavanna AE, Trimble MR. The precuneus: a review of its functional anatomy and behavioural correlates. *Brain*. 2006:129:564–583.

Chao-Gan Y, Yu-Feng Z. DPARSF: A MATLAB toolbox for "pipeline" data analysis of resting-state fMRI. *Front Syst Neurosci*. 2010:4:13.

Clark VP, Parasuraman R. Neuroenhancement: enhancing brain and mind in health and in disease. *NeuroImage*. 2014:85:889–894.

Damoiseaux JS. Effects of aging on functional and structural brain connectivity. *NeuroImage*. 2017:160:32–40.

Davis SW, Dennis NA, Daselaar SM, Fleck MS, Cabeza R. Que PASA? The posterior-anterior shift in aging. *Cereb Cortex*. 2008:18: 1201–1209.

De Filippi E, Escrichs A, Càmara E, Garrido C, Sánchez-Fibla M, Gilson M, Deco G. Meditation-induced effects on whole-brain structural and effective connectivity. *bioRxiv*. 2021 June:10.447903.

Deco G, Kringelbach ML, Jirsa VK, Ritter P. The dynamics of resting fluctuations in the brain: metastability and its dynamical cortical core. *Sci Rep*. 2017:7:3095.

Deco G, Cabral J, Saenger VM, Boly M, Tagliazucchi E, Laufs H, Van Someren E, Jobst B, Stevner A, Kringelbach ML. Perturbation of whole-brain dynamics *in silico* reveals mechanistic differences between brain states. *NeuroImage*. 2018:169:46–56.

Deco G, Cruzat J, Cabral J, Tagliazucchi E, Laufs H, Logothetis NK, Kringelbach ML. Awakening: predicting external stimulation to force transitions between different brain states. *Proc Natl Acad Sci*. 2019:116:18088–18097.

Escrichs A, Biarnes C, Garre-Olmo J, Fernández-Real JM, Ramos R, Pamplona R, Brugada R, Serena J, Ramió-Torrentà L, Coll-De-Tuero G, et al. Whole-brain dynamics in aging: disruptions in functional connectivity and the role of the rich club. *Cereb Cortex*. 2021a:31:2466–2481.

Escrichs A, Perl YS, Uribe C, Camara E, Türker B, Pyatigorskaya N, López-González A, Pallavicini C, Panda R, Annen J, et al. Unifying turbulent dynamics framework distinguishes different brain states. *bioRxiv*. 2021b:14.464380.

Ferreira LK, Busatto GF. Resting-state functional connectivity in normal brain aging. *Neurosci Biobehav Rev*. 2013:37:384–400.

Figueroa CA, Cabral J, Mocking RJT, Rapuano KM, van Hartevelt TJ, Deco G, Expert P, Schene AH, Kringelbach ML, Ruhé HG. Altered ability to access a clinically relevant control network in patients remitted from major depressive disorder. *Hum Brain Mapp*. 2019:40:2771–2786.

Fjell AM, Sneve MH, Grydeland H, Storsve AB, Walhovd KB. The disconnected brain and executive function decline in aging. *Cereb Cortex*. 2017:27:2303–2317.

Fox MD, Buckner RL, Liu H, Chakravarty MM, Lozano AM, Pascual-Leone A. Resting-state networks link invasive and noninvasive brain stimulation across diverse psychiatric and neurological diseases. *Proc Natl Acad Sci*. 2014:111:E4367–E4375.

Geerligs L, Renken RJ, Saliasi E, Maurits NM, Lorist MM. A brain-wide study of age-related changes in functional connectivity. *Cereb Cortex*. 2015:25:1987–1999.

Glerean E, Salmi J, Lahnakoski JM, Jääskeläinen IP, Sams M. Functional magnetic resonance imaging phase synchronization as a measure of dynamic functional connectivity. *Brain Connect*. 2012:2:91–101.

Gong G, Rosa-Neto P, Carbonell F, Chen ZJ, He Y, Evans AC. Age- and gender-related differences in the cortical anatomical network. *J Neurosci*. 2009:29:15684–15693.

Grady C, Sarraf S, Saverino C, Campbell K. Age differences in the functional interactions among the default, frontoparietal control, and dorsal attention networks. *Neurobiol Aging*. 2016:41:159–172.

Hagmann P, Cammoun L, Gigandet X, Meuli R, Honey CJ, Wedeen VJ, Sporns O. Mapping the structural core of human cerebral cortex. *PLoS Biol*. 2008:6:e159.

Hampstead BM, Sathian K, Bikson M, Stringer AY. Combined mnemonic strategy training and high-definition transcranial direct current stimulation for memory deficits in mild cognitive impairment. Alzheimer's dement. *Transl Res Clin Interv*. 2017:3:459–470.

van den Heuvel MP, Sporns O. Rich-club organization of the human connectome. *J Neurosci*. 2011:31:15775–15786.

Ipiña IP, Kehoe PD, Kringelbach M, Laufs H, Ibañez A, Deco G, Perl YS, Tagliazucchi E. Modeling regional changes in dynamic stability during sleep and wakefulness. *NeuroImage*. 2020:215:116833.

Kringelbach ML, Deco G. Brain states and transitions: insights from computational neuroscience. *Cell Rep*. 2020:32:108128.

Kringelbach ML, Cruzat J, Cabral J, Knudsen GM, Carhart-Harris R, Whybrow PC, Logothetis NK, Deco G. Dynamic coupling of whole-brain neuronal and neurotransmitter systems. *Proc Natl Acad Sci U S A*. 2020:117:9566–9576.

Kunze T, Hunold A, Haueisen J, Jirsa V, Spiegler A. Transcranial direct current stimulation changes resting state functional connectivity: a large-scale brain network modeling study. *NeuroImage*. 2016:140:174–187.

Leemans A, Jones DK. The B -matrix must be rotated when correcting for subject motion in DTI data. *Magn Reson Med*. 2009:61:1336–1349.

Li HJ, Hou XH, Liu HH, Yue CL, Lu GM, Zuo XN. Putting age-related task activation into large-scale brain networks: a meta-analysis of 114 fMRI studies on healthy aging. *Neurosci Biobehav Rev*. 2015:57:156–174.

López-González A, Panda R, Ponce-Alvarez A, Zamora-López G, Escrichs A, Martial C, Thibaut A, Gosseries O, Kringelbach ML, Annen J, et al. Loss of consciousness reduces the stability of brain hubs and the heterogeneity of brain dynamics. *Commun Biol*. 2021:4:1–15.

Lord LDD, Expert P, Atasoy S, Roseman L, Rapuano K, Lambiotte R, Nutt DJ, Deco G, Carhart-Harris RL, Kringelbach ML, et al. Dynamical exploration of the repertoire of brain networks at rest is modulated by psilocybin. *NeuroImage*. 2019:199:127–142.

Muldoon S, Pasqualetti F, Gu S, Cieslak M, Grafton ST, Vettel JM. Stimulation-based control of dynamic brain networks. *PLoS Comput Biol*. 2016:12:1005076.

Muthuraman M, Fleischer V, Kolber P, Luessi F, Zipp F, Groppa S. Structural brain network characteristics can differentiate CIS from early RRMS. *Front Neurosci*. 2016:10:14.

Northoff G, Wainio-Theberge S, Evers K. Is temporo-spatial dynamics the "common currency" of brain and mind? in quest of "spatiotemporal neuroscience". *Phys Life Rev*. 2020:33:34–54.

Ozdemir RA, Tadayon E, Boucher P, Momi D, Karakhanyan KA, Fox MD, Halko MA, Pascual-Leone A, Shafi MM, Santarnecchi E. Individualized perturbation of the human connectome reveals reproducible biomarkers of network dynamics relevant to cognition. *Proc Natl Acad Sci*. 2020:117:8115–8125.

Persson J, Pudas S, Nilsson LG, Nyberg L. Longitudinal assessment of default-mode brain function in aging. *Neurobiol Aging*. 2014:35:2107–2117.

Puig J, Biarnes C, Pedraza S, Vilanova JC, Pamplona R, Fernández-Real JM, Brugada R, Ramos R, Coll-de Tuero G, Calvo-Perxas L, et al. The aging imageomics study: rationale, design and baseline characteristics of the study population. *Mech Ageing Dev*. 2020:189:111257.

Reuter-Lorenz PA, Cappell KA. Neurocognitive aging and the compensation hypothesis. *Curr Dir Psychol Sci*. 2008:17:177–182.

Sanz Perl Y, Pallavicini C, Pérez Ipiña I, Demertzi A, Bonhomme V, Martial C, Panda R, Annen J, Ibañez A, Kringelbach M, et al. Perturbations in dynamical models of whole-brain activity dissociate between the level and stability of consciousness. *PLoS Comput Biol*. 2021:17:e1009139.

Shen X, Tokoglu F, Papademetris X, Constable RT. Groupwise whole-brain parcellation from resting-state fMRI data for network node identification. *NeuroImage*. 2013:82:403–415.

Smith SM. Fast robust automated brain extraction. *Hum Brain Mapp.* 2002:17:143–155.

Spiegler A, Hansen EC, Bernard C, McIntosh AR, Jirsa VK. Selective activation of resting-state networks following focal stimulation in a connectome-based network model of the human brain. *Eneuro.* 2016:3:5.

Sporns O. Network attributes for segregation and integration in the human brain. *Curr Opin Neurobiol.* 2013:23:162–171.

Spreng RN, Stevens WD, Viviano JD, Schacter DL. Attenuated anti-correlation between the default and dorsal attention networks with aging: evidence from task and rest. *Neurobiol Aging.* 2016:45: 149–160.

Thibaut A, Bruno MA, Ledoux D, Demertzi A, Laureys S. TDCS in patients with disorders of consciousness: Sham-controlled randomized double-blind study. *Neurology.* 2014:82:1112–1118.

United Nations. *World population ageing 2019.* United Nations: Technical report; 2019

Utevsky AV, Smith DV, Huettel SA. Precuneus is a functional core of the default-mode network. *J Neurosci.* 2014:34:932–940.

Van Den Heuvel MP, Kahn RS, Goñi J, Sporns O. High-cost, high-capacity backbone for global brain communication. *Proc Natl Acad Sci.* 2012:109:11372–11377.

Wang L, LaViolette P, O'Keefe K, Putcha D, Bakkour A, Van Dijk KR, Pihlajamäki M, Dickerson BC, Sperling RA. Intrinsic connectivity between the hippocampus and posteromedial cortex predicts memory performance in cognitively intact older individuals. *NeuroImage.* 2010:51: 910–917.

Whitfield-Gabrieli S, Nieto-Castanon A. Conn : a functional connectivity toolbox for correlated and anticorrelated brain networks. *Brain Connect.* 2012:2:125–141.

WHO. WHO | Proposed working definition of an older person in Africa for the MDS Project. *World Heal Organ.* 2016. https://www.who.int/healthinfo/survey/ageingdefnol.

Yao ZF, Hsieh S. Age differences of the hierarchical cognitive control and the frontal rostro-caudal functional brain activation. *Cereb Cortex.* 2021:1–19.

Zhang D, Li H, Sun J, Hu W, Jin W, Li S, Tong S. Antidepressant-like effect of low-intensity transcranial ultrasound stimulation. *IEEE Trans Biomed Eng.* 2019:66:411–420.

Zhao T, Cao M, Niu H, Zuo XN, Evans A, He Y, Dong Q, Shu N. Age-related changes in the topological organization of the white matter structural connectome across the human lifespan. *Hum Brain Mapp.* 2015:36:3777–3792.

4.4 Article 4

ARTICLE

Unifying turbulent dynamics framework distinguishes different brain states

Anira Escrichs [1,26✉], Yonatan Sanz Perl[1,2,3,26✉], Carme Uribe [4,5], Estela Camara[6,7], Basak Türker[3,8,9], Nadya Pyatigorskaya[3,8,9,10], Ane López-González [1], Carla Pallavicini[11,12], Rajanikant Panda [13,14], Jitka Annen [13,14], Olivia Gosseries [13,14], Steven Laureys [13,14,15,16], Lionel Naccache [3,8,9], Jacobo D. Sitt[3,8,9], Helmut Laufs [17,18], Enzo Tagliazucchi[12,19], Morten L. Kringelbach [20,21,22,27✉] & Gustavo Deco [1,23,24,25,27✉]

Significant advances have been made by identifying the levels of synchrony of the underlying dynamics of a given brain state. This research has demonstrated that non-conscious dynamics tend to be more synchronous than in conscious states, which are more asynchronous. Here we go beyond this dichotomy to demonstrate that different brain states are underpinned by dissociable spatiotemporal dynamics. We investigated human neuroimaging data from different brain states (resting state, meditation, deep sleep and disorders of consciousness after coma). The model-free approach was based on Kuramoto's turbulence framework using coupled oscillators. This was extended by a measure of the information cascade across spatial scales. Complementarily, the model-based approach used exhaustive in silico perturbations of whole-brain models fitted to these measures. This allowed studying of the information encoding capabilities in given brain states. Overall, this framework demonstrates that elements from turbulence theory provide excellent tools for describing and differentiating between brain states.

[1] Computational Neuroscience Group, Center for Brain and Cognition, Department of Information and Communication Technologies, Universitat Pompeu Fabra, Barcelona, Catalonia, Spain. [2] Universidad de San Andrés, Buenos Aires, Argentina. [3] Institut du Cerveau et de la Moelle épinière, ICM Paris, France. [4] Medical Psychology Unit, Department of Medicine, Institute of Neuroscience, University of Barcelona, Barcelona, Catalonia, Spain. [5] Institute of Biomedical Research August Pi i Sunyer (IDIBAPS), Barcelona, Catalonia, Spain. [6] Cognition and Brain Plasticity Unit, Bellvitge Biomedical Research Institute (IDIBELL), L'Hospitalet de Llobregat, Barcelona, Spain. [7] Department of Cognition, Development and Educational Psychology, University of Barcelona, Barcelona, Spain. [8] Inserm U 1127, Paris, France. [9] CNRS UMR 7225, Paris, France. [10] Department of Neuroradiology, AP-HP, Hôpital Pitié-Salpêtrière, Sorbonne Université, Paris, France. [11] Fundación para la Lucha contra las Enfermedades Neurológicas de la Infancia (FLENI), Buenos Aires, Argentina. [12] Department of Physics, University of Buenos Aires, Buenos Aires, Argentina. [13] Coma Science Group, GIGA Consciousness, University of Liège, Liège, Belgium. [14] Centre du Cerveau, University Hospital of Liège, Liège, Belgium. [15] Joint International Research Unit on Consciousness, CERVO Brain Research Centre, U Laval CANADA, Québec, QC, Canada. [16] International Consciousness Science Institute, Hangzhou Normal University, Hangzhou, China. [17] Department of Neurology, Christian Albrechts University, Kiel, Germany. [18] Department of Neurology and Brain Imaging Center, Goethe University, Frankfurt am Main, Germany. [19] Latin American Brain Health Institute (BrainLat), Universidad Adolfo Ibañez, Santiago, Chile. [20] Department of Psychiatry, University of Oxford, Oxford, UK. [21] Center for Music in the Brain, Department of Clinical Medicine, Aarhus University, DK, Jutland, Denmark. [22] Centre for Eudaimonia and Human Flourishing, University of Oxford, Oxford, UK. [23] Institució Catalana de la Recerca i Estudis Avancats (ICREA), Barcelona, Catalonia, Spain. [24] Department of Neuropsychology, Max Planck Institute for human Cognitive and Brain Sciences, Leipzig, Germany. [25] School of Psychological Sciences, Monash University, Melbourne, Australia. [26] These authors contributed equally: Anira Escrichs, Yonatan Sanz Perl. [27] These authors jointly supervised this work: Morten L. Kringelbach, Gustavo Deco. ✉email: anira.escrichs@upf.edu; yonatan.sanz@upf.edu; morten.kringelbach@psych.ox.ac.uk; gustavo.deco@upf.edu

Fundamentally different brain states such as sleep, wakefulness, or coma all emerge from the complex dynamics of self-organised brain activity. Nevertheless, an unanswered question in modern neuroscience is how best to characterise the underlying human brain states acquired with neuroimaging[1,2]. Many challenges remain unsolved, and most importantly, there is a need to arrive at an agreed definition of brain states[2–9]. The most important feature of such a definition would help to create a mechanistic framework for characterising brain states in terms of the underlying causal mechanisms and dynamical complexity. An elegant way of assessing dynamical complexity was proposed by Massimini and colleagues who investigated the perturbation-elicited changes in global brain activity during brain states, including wakefulness, sleep, anaesthesia, and post-coma states[10–12]. They have proposed the perturbational complexity index (PCI), which captures the significant differences in brain-wide spatiotemporal propagation of external stimulation, distinguishing between different brain states[10]. Beyond basic neuroscience, a better definition and description of a brain state could offer novel avenues for translational therapeutic interventions to rebalance disrupted brain states in disease.

In a recent review, Goldman and colleagues[1] showed that at both macroscopic and microscopic scales, unconscious brain states are dominated by synchronous activity[13–17], while conscious states are characterised by asynchronous dynamics[15,18,19]. Equally, they propose that brain signals in unconscious and conscious states vary in their algorithmic complexity[20], entropy[21] and dimensionality[22]. The authors were inspired by the elegant mathematical framework of statistical physics, which provides the tools for uncovering structures of microscopic interactions underlying macroscopic properties. They propose that different brain states may emerge from the interactions between populations of neurons, similar to how different states of matter like solids and liquids emerge from interactions between populations of molecules. In other words, unconscious states are more like a solid-state, with high synchrony and low complexity, while conscious states are more like liquids, with asynchronous activity and high complexity.

This dichotomy is very useful for capturing the fundamental difference between conscious and unconscious states, especially for the microstates, where for example, deep sleep is characterised by slow waves[23]. However, the transition between scales is more subtle and crucially depends on the complex percolation across the whole brain of the synchronous and asynchronous microstates, which gives rise to mixed complex dynamical states[24]. The challenge remains to find a unifying dynamical approach, which can establish the balance between different levels of synchrony and complexity needed to distinguish between brain states.

Here, we show that different brain states are always underpinned by spatiotemporal dynamics, but the mixing across scales gives rise to dissociable dynamical characteristics, beyond simply synchronous and asynchronous signatures. We investigate this using two complementary model-free and model-based frameworks.

For the model-free framework, we profited from the advances in turbulence theory in physics[25–28]. In physical systems, starting with fluid dynamics[25–27], turbulence has been shown to provide the optimal transmission of energy, and at the core of this transmission are the scale-free mixing properties of turbulence. Mathematically, it can be shown that energy is essentially information[29,30]. The essence of turbulence is the efficient transmission of energy/information in fluid dynamics, which was shown by Kolmogorov to be captured by elegant scale-free statistical power laws[26,27]. This shows that rather than using fine-grained Navier-Stokes equations of the billions of molecules in fluid dynamics[31], the extremely high dimensional system of fluid dynamics can be described in a much simpler, lower-dimensional space.

Beyond this fluid dynamics approach to turbulence, Kuramoto showed that coupled oscillators can be used to capture turbulence in many other systems, suggesting that coupled oscillators could sustain optimal information transmission[28]. Specifically, within the framework of coupled oscillators, turbulence can be characterised as the variability across space and time of the *local* level of synchronisation of the coupled oscillators. In fact, this characterisation is a generalisation of the concept of metastability[32–36], which in neuroscience has been measured as the variability across time of the *global* level of synchronisation of the whole system, commonly known as the global Kuramoto order parameter of a dynamical system.

Here, however, as in previous papers, we describe that the human brain operates in a turbulent regime[37,38], in the sense of Kuramoto[38], which confers important information processing advantages, including significantly enhancing the functional role of the anatomically rare long-range connections[39]. We focus on Kuramoto's related concept of a *local* order parameter, defined as the local level of synchronisation in the system[40]. The variability of this local measure across spacetime turns out to be a sensitive and precise description of the level of turbulence. Importantly, the level of local synchronisation can be thought of as analogous to the rotational vortices found in fluid dynamics, where the size of these vortices in 'vortex space' defines the different scales of information processing.

In turbulence many researchers operate in such a 'vortex space' rather than the signal space[29,41], which is the strategy that we also use here, noting that this is the first application of the strategy of measuring information transfer in the brain.

For the model-based framework, it has been shown that emergent collective macroscopic behaviour of brain models only depends weakly on individual neuron behaviour[42]. Here we used whole-brain modelling based on the integration of anatomy and dynamics, which can be used to accurately fit and reproduce many aspects of empirical neuroimaging data[43–46], and specifically to capture the brain turbulent dynamics[38,47]. Over the years, there have been many different whole-brain models with varying degree of biophysical realism, from spiking networks to mean-field to oscillatory Hopf whole-brain model[43,48–52]. However, it has been shown that rather than modelling the complex spiking neuronal and mean field dynamics, very high precision fitting can be achieved by using coupled oscillators, allowing for the capture of the most important features of mesoscopic brain dynamics[49].

Importantly, using a Hopf whole-brain model allows for in silico exhaustive perturbation of the model that can be used to assess many aspects, including the susceptibility and information encoding capability. These two measures have been defined in previous works to successfully demonstrate that the susceptibility is enhanced due to long-range connections in the brain[39] and the information encoding capability is maximal when the brain operates in turbulent regime[38]. In other words, the model-free approach measures the naturally occurring information transmission flow, while the model-based approach allows us to measure the reactivity of the brain to external perturbations.

Furthermore, it has been shown that simply varying the global coupling in the Hopf whole-brain model produces excellent fits not only to normal resting state data but also to other brain states such as psychedelics[45], coma, anaesthesia[53] and sleep[45]. The most parsimonious explanation for this ability to fit multiple brain states is that the turbulence-generating Hopf model varies as function of the global coupling[37–39]. This would provide a causal mechanistic explanation of why turbulence is a sensitive and specific marker of the underlying brain state.

Overall, we hypothesised that the model-free and model-based complementary frameworks will allow us to differentiate between
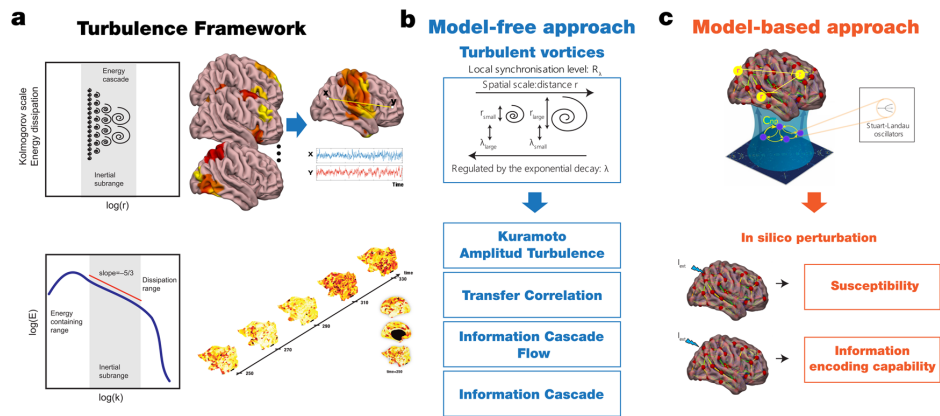
Fig. 1 Overview of framework. a Turbulence in fluids is one the most common dynamical regime where the mixing motion governs (left panel). The energy cascade, i.e., how the energy travels across scale while dissipated and the statistical properties defined as power laws on the energy levels and structure functions (bottom panel) determine the turbulent behaviour of the fluid. The analogy between brain activity and Turbulence has been recently demonstrated using resting state data from a large dataset of 1,003 healthy human participants. **b** Model-free approach. The turbulent behaviour of brain activity is reflected in the similarity between the local level of synchronisation, determined by the local Kuramoto order parameter (R) at different scales (λ), and vortex with different spatial scales in fluid dynamics. The spatial scale (r) of the vortex is inversely related with the exponential decay of the local Kuramoto order parameter (λ). The turbulence regime also endows the brain with an efficient information cascade measured as the correlation of the local level of synchronisation across scales (Information Cascade Flow). The average across scales of the information cascade flow is defined as the Information cascade. The Transfer Correlation quantified as the correlation of local synchronisation across space at different scales also characterises the brain's information processing. **c** In the Hopf whole-brain model, the dynamics of each brain area are described through a Stuart Landau non-linear oscillator. The system of local oscillators is connected through the anatomical connectivity to simulate the global dynamics, capable of reproducing statistical observables from fMRI data. We used as structural connectivity the long-range connections (LR) from human diffusion MRI measurements on top of an exponential distance rule (EDR) to fit the empirical functional connectivity as a function of the Euclidean distance (following the relation between the Kolmogorov's second-order structure-function and the traditional FC). Using whole-brain modelling allows obtaining measures that rise from the in silico perturbative approach. We simulated external stimuli and evaluated the model's reaction for each brain state by quantifying the susceptibility and information capability measures.

different brain states. We found turbulent dynamics (in the sense of Kuramoto[28]) in all the different brain states but, crucially, using the model-free framework, we were able to characterise the different information transmission across spacetime scales in resting state, meditation, deep sleep and post-coma states. Furthermore, the model-based framework showed that different information encoding capabilities[39] characterise different brain states. Thus, according to our hypothesis, the complementary methods are able to not only significantly distinguish between different brain states but also offer a unifying dynamical framework for mechanistically describing the underlying fundamental principles.

Results

We used model-free and model-based frameworks to explore information transmission flow in whole-brain dynamics across different brain states. Specifically, we compared brain measures on three independent resting-state fMRI datasets. The meditation dataset comprised experienced Vipassana meditators ($N = 19$) during both focused attention meditation (M) and resting state (R). The sleep dataset comprised healthy subjects during deep sleep, i.e., stage 3 (DS, $N = 13$) and resting state (R, $N = 13$) states. Finally, the disorders of consciousness (DOC) dataset were acquired in two independent research sites (Liège and Paris), comprised of healthy volunteers (R_{CNT}: $N = 49$) and DOC patients diagnosed in a minimally conscious state (R_{MCS}: $N = 66$) or an unresponsive wakefulness state (R_{UWS}: $N = 39$).

First, we applied the model-free approach to measuring information transmission flow across spacetime scales based on the recent finding demonstrating turbulence in human brain

dynamics (Fig. 1a)[38]. This analysis was based on the local Kuramoto order parameter that describes the local level of synchronisation of a brain area, n, as a function of space, $\bar{x}$, and time, t, at a given scale, λ. The scale of the local synchronisation is defined by the parameter λ, which determines the size of the spatial distances where the synchronisation is evaluated, where high values of λ stand for short distances, and vice versa (Fig. 1b). In particular, we computed for each dataset the amplitude turbulence defined by Kuramoto as the space and time variability of the local level of synchronisation[28,40,54] (referred here as Kuramoto amplitude turbulence), and three measures quantifying the information transmission in terms of scale, space and time correlation of the local level of synchronisation that we defined as transfer correlation, information cascade flow, and information cascade (Fig. 1 and see more details in Methods and ref. [39]).

Second, we applied the model-based approach based on the sensitivity of these models to react to external in silico perturbations (Fig. 1c and Methods). For each brain state, we constructed a whole-brain dynamical model based on the normal form of a supercritical Hopf bifurcation coupled with the dMRI structural connectivity and the exponential distance rule (EDR). Finally, to evaluate how each model fitted reacts to external stimuli, we applied in silico perturbations by quantifying the susceptibility and information encoding capability measures.

Model-free framework. We computed the information transmission flow measures on the three datasets in terms of Kuramoto amplitude turbulence and transfer correlation within the 0.008–0.08 Hz frequency range (see Methods). First, we explored the level of Kuramoto amplitude turbulence over different λ
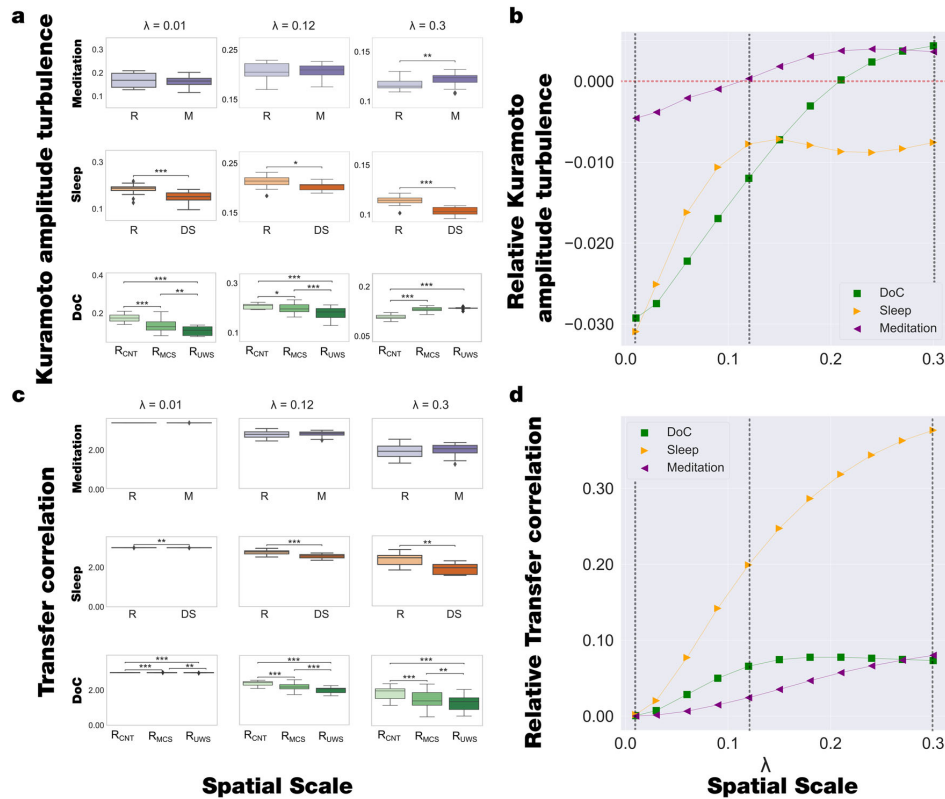
Fig. 2 Model-free framework reveals significant differences in Kuramoto amplitude turbulence and transfer correlation in different brain states. a The plots show the level of Kuramoto amplitude turbulence at different spatial scales, from $\lambda = 0.01$ (100 mm) to $\lambda = 0.3$ (3 mm) in steps of 0.03, and show the comparison between brain states for $\lambda = 0.01$, $\lambda = 0.12$ and $\lambda = 0.3$. The meditation state showed significant increases in Kuramoto amplitude turbulence compared to the resting state only on higher scales. The DS shows significantly lower Kuramoto amplitude turbulence than the resting state across all spatial scales. By contrast, the Kuramoto amplitude turbulence showed significant decreases in R_{MCS} and R_{UWS} states in lower lambda scales but significant increases in higher scales compared to R_{CNT}. **b** The plots were computed as the linear fit of the mean level of Kuramoto amplitude turbulence at each scale for the three brain states for the DOC dataset (i.e., R_{CNT}, R_{MCS}, and R_{UWS}) and two brain states for sleep and meditation datasets (i.e., W, DS, and R, M, respectively). The plots display the obtained slopes as a function of the scale. In particular, DOC showed negative slopes at lower scales and increased with the scales up to positive slopes. The sleep dataset presented negative slopes at lower scales, increased up to $\lambda = 0.12$, and a negative slope value was kept almost constant. The meditation dataset also increased with scale but presented less variability than the other datasets. Dashed vertical lines indicate the scales displayed in A and the horizontal red dashed line highlights the zero slope. **c** We computed the transfer correlation ($|A^\lambda|$), which measures how the information travels across space at different spatial scales, i.e., we show the results as a constant k - $|A^\lambda|$, with $k = 3$ $|A^\lambda|$. The meditation state presents no significant differences on any scale compared to the resting state. In contrast, the transfer correlation significantly decreased for DS and R_{MCS}, R_{UWS} states compared to the resting state across all scales. **d** We performed the same computation as in panel B for the transfer correlation measure. In this case, DOC and sleep datasets presented a similar slope-scale relationship, whereas the meditation dataset presented less variability across scales. In the figure, P-values were assessed using the Wilcoxon rank-sum test and corrected for multiple comparisons, $*P < 0.05$, $**P < 0.01$ and $***P < 0.001$.

values, i.e., from 0.01 (~100 mm) to 0.30 (~3 mm), in steps of 0.03. This measure was defined as the standard deviation across time (t) and space (brain areas, n) of the local Kuramoto order parameter. We found that the meditation state increases Kuramoto amplitude turbulence levels in higher spatial scales, i.e., short distances in the brain, compared to the resting state. On the other hand, the deep sleep state shows lower Kuramoto amplitude turbulence levels than the resting state across all the spatial scales. Finally, the Kuramoto amplitude turbulence levels decrease for DOC patients (R_{MCS} and R_{UWS}) compared to healthy controls during resting state in lower lambda values, i.e., long distances, but increases in higher lambda scales; differentiating, also, between the R_{UWS} and R_{MCS} groups. The results of Kuramoto

amplitude turbulence levels in each state are displayed in Fig. 2a. We included in the supplemental material seven videos (Supplementary Videos 1 to 7) of the full spatiotemporal evolution of Kuramoto amplitude turbulence in one hemisphere across time of the full resting state of a single participant for each brain state within each dataset. Furthermore, to summarise the behaviour of the time and space information transmission measures at different scales, we quantified the Kuramoto amplitude turbulence changes at each λ across brain states. We computed a linear fit to the mean Kuramoto amplitude turbulence of brain states at each λ and obtained the slopes of the corresponding lines, which stands for Kuramoto amplitude turbulence across brain states at a specific scale. Figure 2b shows the relationship between these

slopes and scales for each dataset. The meditation dataset presents similar behaviour but is less sensitive to this measure, i.e., lower variability of the slope values across scales. By contrast, the sleep dataset shows a monotonical increase of slope values from negative values at low scales up to $\lambda = 0.12$, where it remains almost constant for higher scales. Finally, DOC states present the same behaviour: the slopes monotonically increase from negative values at low λ scales towards positive values at high λ. This positive slopes at high λ can be associated with an increase in the short-range information transmission with a lack of a global broadcasting due to the long-range transmission diminution (negative slopes at low λ). It is noticeable that with this quantification it is possible to differentiate between datasets that involve a reduction of consciousness, i.e., despite that sleep and DOC patients present a reduction of the information processing in many scales, the behaviour across scales captures differences between sleep and DOC states.

Secondly, we explored how the information is transferred across space in terms of the time correlation between the level of local synchronisation at each scale (see Methods). This measure indicates how the information travels across space at a given spatial scale, λ. We found that the transfer correlation in the meditation state did not significantly differ across any scale compared to the resting state. By contrast, this measure significantly decreases for deep sleep and DOC states across all λ scales compared to the resting state, and interestingly, differentiating the R_{MCS} and R_{UWS} groups across all scales (Fig. 2c). Furthermore, to summarise the behaviour of transfer correlation at different scales, we quantified the changes at each λ across brain states. Conversely, the evolution of the slopes across scales for the transfer correlation presents the same behaviour across all datasets (Fig. 2d).

We measured how the information travels across scales by defining the information cascade flow, as the predictability in terms of time correlation of a given level of local synchronisation

at scale λ from the level of local synchronisation at scale $\lambda - \Delta\lambda$, in consecutive time steps, t and $t + \Delta t$ (where $\Delta\lambda$ and Δt are the discretisation of scale and time, respectively). This is important, given that the brain is organised as a hierarchy where information flows from bottom to top in a recurrent reciprocal manner, i.e. segregated sensory information is processed first and iteratively more refined and integrated, while a global workspace at the top of the hierarchy integrates information. We found that the meditation state did not significantly changes compared to the resting state, whereas for deep sleep and DOC, the information cascade flow decreases across all scales compared to the resting state (Fig. 3a).

Finally, to summarise the information transmission's whole behaviour across scales, we defined the information cascade as the information cascade flow average across all λ scales. We found that the information cascade in the meditation state presents no significant differences compared to the resting state. In contrast, the deep sleep and DOC states present less transfer correlation across the scales than the resting state, moreover, the information cascade clearly differentiate between R_{CNT} and R_{UWS} states (Fig. 3b).

To assess the regional heterogeneity of the synchronisation time variability at a given scale, we defined the node-level metastability as the standard deviation over time of the local Kuramoto order parameter for each brain state in each dataset. This measure indicates how changes the level of local synchronisation across time. We quantified this difference by computing the Kolmogorov-Smirnov distance (KSD) between the distributions of node-level metastability, where larger values mean more different distributions (see Methods). We found that the KSD for all datasets monotonically decreases between brain states across scales, whereas the value of λ increases. In other words, the KSD is maximal for lower values of λ, i.e., long distances in the brain. In particular, for DOC states, the higher KSD is found between R_{CNT} and R_{UWS} states (Fig. 4a). Furthermore, we show the
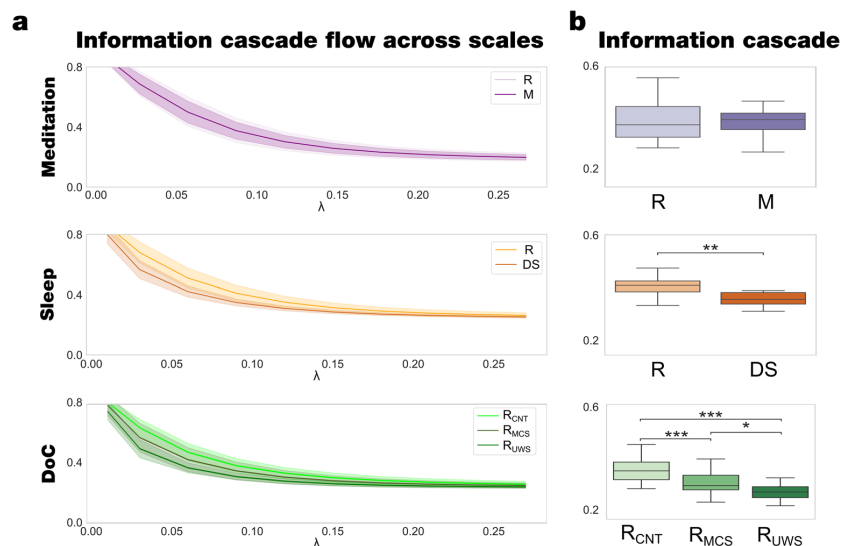

Fig. 3 Model-free framework showed differences in information cascade flow and information cascade in different brain states. a The information cascade flow across scales is the predictability given by the level of synchronisation at a specific scale (λ) from the previous scale $\lambda - \Delta\lambda$ (where $\Delta\lambda = 0.03$ is the discretisation of scale). The meditation state presents no differences across the scales compared to the resting state, the information cascade flow significantly decreases for DS and R_{MCS}, R_{UWS} states compared to the resting across all scales. **b** The information cascade, defined as the average information cascade flow, differentiates R_{MCS}, R_{UWS}, and DS states from the resting state, while the meditation state presents no differences. P-values were assessed using the Wilcoxon rank-sum test and corrected for multiple comparisons, *$P < 0.05$, **$P < 0.01$ and ***$P < 0.001$.
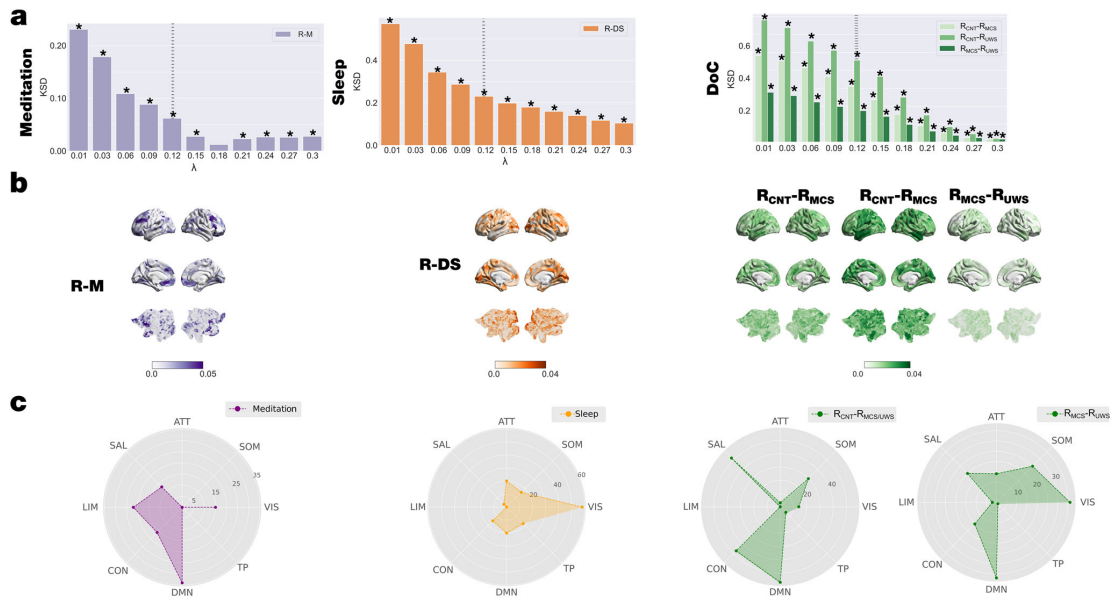
Fig. 4 Local node-level metastability was significantly different between brain states and revealed distinct signatures of network involvement. We computed the node-level metastability as the standard deviation across time of the local Kuramoto order parameter (see Methods). **a** We performed the KSD between distributions of the node-level of metastability of each brain state within each dataset for each scale. The KSD for all datasets monotonically decreases, whereas the value of λ increases for all comparisons. **b** Render brains represent the absolute difference of the node-level metastability between each brain state for scale $\lambda = 0.12$, indicated with vertical dashed lines in panel A. We selected the top 15% quantile of absolute differences between conditions, identified the resting state networks to which they belong and quantified the number of nodes per network. **c** Radar plots represent the number of nodes on the top 15% quantile of the absolute difference by each comparison and resting-state network (CON: control; DMN: default mode; TP: temporal-parietal; VIS; visual; SOM: somatomotor; ATT: attentional; SAL: salience; LIM: limbic). The networks showing the highest differences between resting and meditation states were the limbic and default-mode networks. The comparison between deep sleep and resting state shows that nodes of the visual- and default-mode- networks present the highest difference. Finally, the comparison between R_{CNT} and DOC patients (R_{MCS} and R_{UWS}) shows that the somatomotor-, salience-, control-, and default-mode- networks present the highest differences, whereas, specifically in the comparison between R_{MCS} and R_{UWS} nodes associated with the somatomotor- and control- networks present the highest differences. P-values were assessed using the Kolmogorov–Smirnov test and corrected for multiple comparisons, *$P < 0.001$.

absolute difference between the node-level metastability between brain states in each dataset at $\lambda = 0.12$ rendered onto the brain cortex (Fig. 4b).

Then, we identified the resting state networks to which they mainly belong and quantified the number of nodes per network by selecting the nodes for each comparison of the top 15% quantile. We found that differences between meditation and resting state are mainly in the limbic and default-mode networks. In contrast, the highest differences between deep sleep and resting state are observed in the nodes of the visual- and default-mode-networks. Finally, the highest differences in local synchronisation are found between controls during resting state and DOC patients (R_{MCS} and R_{UWS}) in the somatomotor-, salience-, control-, and default-mode- networks. Conversely, the highest differences between R_{MCS} and R_{UWS} are observed in nodes associated with visual-, somatomotor- and default mode- networks.

Model-based framework. For each brain state, we built a Hopf whole-brain model of coupled dynamical oscillators in an anatomical brain architecture coupling the exponential distance rule (EDR) and the dMRI matrix fitted to the empirical functional data (see more details in Methods). In particular, we exhaustively varied G from 0 to 7 in 0.1 steps and for each G value we repeated 100 simulations for each brain state with the same TR and time duration as the empirical data. Then, we computed the fitting of

the functional connectivity as the Euclidean distance between the empirical and simulated functional connectivity (FC) as a function of distance (r) within the inertial subrange (see Methods). The optimal working point of each model is determined as the minimum of the fitting level (vertical lines in Fig. 5a). We used the respective minima of each condition as the basis of the following perturbative in silico investigations. The G values obtained for meditation, deep sleep, and DOC are lower than those obtained for the resting state. This result can be interpreted as reducing the coupling between areas to represent the global brain dynamics.

Furthermore, we study how the system reacts to external perturbations by perturbing each model at its optimal working point and computing the model-based measures. Specifically, we defined the susceptibility as the ability of a system to be perturbed, and we estimated by measuring the perturbed and non-perturbed modulus of the local Kuramoto order parameter ($\tilde{R}_{\lambda_s}(\bar{x}, t)$ and $R_{\lambda_s}(\bar{x}, t)$, respectively). The perturbation consisted of applying an external periodical force equally for all brain regions. This stimulus was represented as an external additive periodic forcing term, given by $F_j = F_{0j}\cos(\omega_0 t) + iF_{0j}\sin(\omega_0 t)$ with $F_{0j} = 5 \times 10^{-4}$, in the corresponding real and imaginary part of the node j equation (Eqs. 10 and 11 see Methods), with frequency ω_0 equal to the average across node of the empirical node frequency (Fig. 1c). Finally, we computed the susceptibility
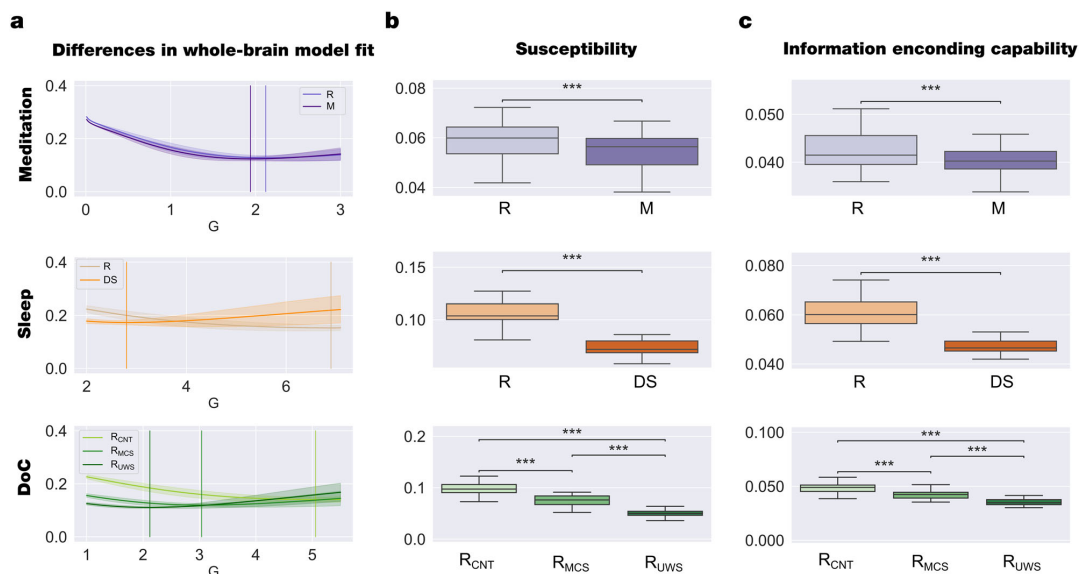
Fig. 5 Model-based framework revealed significant perturbative differences for different brain states. a We show the evolution of the error of the whole-brain model FC fitting to the empirical fMRI data as a function of the global coupling strength, G. The error of the FC fitting was given by the square root of the difference between the simulated and empirical FC matrix. The optimal working point of the model was defined as the minimum value of the FC fitting, i.e., where the model shows maximal similarity to the empirical fMRI data. **b** We show the results of the susceptibility measure, which estimates how these models react to external periodical force perturbations. In all datasets, the resting state was the most susceptible to be perturbed. **c** We show the information encoding capability of the whole-brain models, which captures how different external stimulations are encoded in the dynamics. Similar to the susceptibility measure, the resting state was more susceptible to react to the perturbations. Susceptibility and information capability measures differentiated each brain state and between R_{MCS} and R_{UWS} groups. These results show that each brain state encodes the whole-brain dynamics with a particular complexity. P-values were assessed using the Wilcoxon rank-sum test and corrected for multiple comparisons; ***$P < 0.001$.

as the difference between the perturbed and non-perturbed cases averaged across time, trials, and space. Note that we here define susceptibility as the ability of the system to be externally perturbed, in the same sense found in electromagnetism, where the 'magnetic susceptibility' is determined as the magnetisation of the material as the result of an external field. This general framework was adapted for coupled oscillators by Hiroaki Daido, who defines the susceptibility of a large population of coupled oscillators as the variation of the Kuramoto order parameter under external perturbation[55]. This measure was previously used to demonstrate that the long-range connections enhance the brain responsiveness to external stimulus[39] and also increases is turbulent regime[38]. Here we found that the susceptibility decreases for meditation, deep sleep, and DOC compared to the resting state (Fig. 5b).

Similarly, we computed the information encoding capability (as an extension of the susceptibility) to study how external perturbations are encoded in brain dynamics. This measure was defined as the standard deviation across trials of the difference between the perturbed and unperturbed mean of the modulus of the local Kuramoto order parameter across time, averaged across space. We found that, compared to the resting state, the information encoding capability also decreases for meditation, deep sleep, and DOC (Fig. 5c). To investigate the link between Information encoding capability and complexity well-establish measure, we computed the normalised Lempel-Ziv complexity[56] (LZC) as is described in Casali et al.[10] for each brain state within each data set when it is externally perturbed. We found that the LZC behaves similarly to the Information encoding capability measure but is less sensitive to discriminate between them (see Supplementary Fig. 1).

We replicated the results by randomly changing the bifurcation parameter of each brain area, a_n, within the range $[-0.02:0]$ (see Methods). As shown in Supplementary Fig. 2, we found that the response is the same for both perturbative approaches.

Overall, both perturbative measures show that the capability to react to in silico perturbations decreases for meditation, deep sleep, and DOC compared to the resting state.

Discussion

We were able to significantly distinguish between different brain states based on a unifying framework for defining and measuring the spatiotemporal variability of local synchronisation and information transfer across scales. This research is based on Kuramoto's important research for extending the concept of turbulence in the context of coupled oscillators[28] (for other frameworks used to study turbulence, see[25–27,29]). Using Kuramoto's insight, we have previously shown turbulence-like dynamics in the healthy human brain[37–39]. Here we extended these results by using model-free and model-based frameworks to demonstrate that different brain states exhibit different levels of such turbulent-like dynamics and information transfer across scales. In turbulence, such local level of synchronisation across spatial scales is usually called 'vortex space'. Our model-free framework was able to show the role of information cascade in 'vortex space' as a distinguishing feature between brain states (resting state, meditation, deep sleep, R_{MCS}, and R_{UWS}) as measured by fMRI neuroimaging. As such our results demonstrated that these brain states exhibit significant differences in information cascade across different scales at both the spatial and temporal domains. Equally, our model-based approach fitted a whole-brain model to the

empirical data, which allowed us to exhaustively perturb the system to demonstrate differences in susceptibility and information encoding capabilities between different brain states. The results showed that when inducing a shift in the intrinsic local dynamics of brain areas, the brain responds to the external perturbations less sensitively as the conscious awareness diminishes.

This framework captures the differences in percolation between scales across the whole brain of the different levels of synchrony and complexity associated with different brain states. At the mesoscopic level, the result of this percolation and mixing across scales is always reflected in the brain dynamics determined by the spatiotemporal variability of local synchronisation.

Overall, the proposed unifying framework reconciles the balance between different levels of synchrony and complexity of large population of coupled oscillators for describing and differentiating between brain states. Importantly, both model-free and model-based measures successfully differentiate the minimally conscious state (R_{MCS}) and unresponsive wakefulness syndrome (R_{UWS}) groups.

Previously, it has been shown that the information processing associated with rare long-range (LR) connections is significantly enhanced in the resting state of healthy awake participants[39]. When reducing the level of spatiotemporal variability of local synchronisation, in what we call the turbulent regime, for a model with LR connections, this resulted in a reduced level of long-range information transmission. While we were not explicitly testing a model with and without LR connections, we found that the evolution of Kuramoto amplitude turbulence and information cascade at different spatial scales is significantly different between different brain states. In fact, Fig. 2a and b show that compared to a group of healthy controls, the DOC groups exhibited lower levels of turbulence at higher spatial scales (i.e., lower λ and larger distances) but higher levels of turbulence at lower spatial scales. This dramatic reduction of long-range information transmission in R_{UWS} and R_{MCS} patients (see relevant boxplot for $\lambda = 0.01$ in Fig. 2a) could be a defining feature of the reduction of conscious awareness in these patients. This results is consistent with EEG evidence showing that noncommunicative patients have lower global information sharing[57], and decreased brain complexity[58,59]. This also aligns with the global neuronal workspace theory that postulates that the long-distance connexions globally broadcast the information for different processor brain-wide and this lack of spatially bounded information processing is associated with conscious access[60].

In healthy participants, deep sleep was characterised by lower Kuramoto amplitude turbulence across all spatial scales, demonstrating a reduction in information processing over both short and long distances[61,62]. In contrast, in highly trained meditators, the meditation state presented higher Kuramoto amplitude turbulence only at lower spatial scales (large λ and short distances), suggesting that meditation is a state showing an alteration rather than a reduction of consciousness. Overall, the results demonstrate that each brain state exhibits different turbulent dynamic patterns across spatial scales, allowing us to characterise the brain states based on fluctuations of their underlying information processing. Interestingly, this also allowed us to differentiate between deep sleep and DOC states, thus unveiling specific and unique features of turbulent dynamics underlying low-level states of consciousness, going beyond a simple dichotomy of synchrony and asynchrony.

The results also gave new insights into information processing across scales changes with brain state. Working in 'vortex space', we quantified three different measures of information transfer, information cascade flow and information cascade for each brain state. Figure 2c and d show that information transfer increased significantly with the spatial scale between normal resting state

and the level of awareness in the other brain states (meditation, deep sleep and DOC). This result clearly demonstrates that the measure of information transfer indexes conscious awareness. Interestingly, while this measure increases with the distance between resting and meditation, this difference is not statistically significant. This suggests that meditation is more similar to the resting state but that there are important significant differences which can be revealed by the other information transmission measures.

The information cascade flow monotonically decreased with shorter distances (the increase in spatial scale λ) for all brain states (shown in Fig. 3a). This measure also discriminated *between* conditions within each dataset, i.e., showing lower values for DOC patients than control participants and in the deep sleep stage compared to the resting state in the same participants. The information cascade (i.e., the average of the information flow across scales) was lower in low-levels states of awareness (deep sleep, R_{MCS} and R_{UWS}) than in normal resting state (shown in Fig. 3b). Overall, this demonstrates that the information transmission is altered with conscious access and that this is captured with the global information processing measures of information transmission, information cascade flow and information cascade.

The framework also allowed us to identify local brain regions involved in controlling the turbulent dynamics of different brain states. In particular, we defined a 'local node-level metastability' measure as the regional level of the variability of local synchronisation (see Methods). This measure was able to significantly differentiate between different brain states at different spatial scales. Yet, the node-level metastability for higher λ values, i.e., shorter distances in the brain, was less sensitive in discriminating between brain states (Fig. 4a).

Importantly, this node-level of description allowed us to capture the different signatures of the whole-brain dynamics that changed between brain states. As shown by the renderings in Fig. 4b (at $\lambda = 0.12$) and quantified at the network level in Fig. 4c, we found that brain regions belonging to the somatomotor, salience, control, and default-mode networks present the most critical differences in DOC states, with a more substantial decrease in the R_{UWS} than in the R_{MCS} condition, corresponding to lower levels of conscious awareness.

Specifically, we found the highest difference between R_{UWS} and R_{MCS} in brain regions belonging to default mode-, visual- and somatomotor- networks, which is consistent with previous studies in DOC patients[63–66]. We also found that changes in regions in visual- and default-mode- networks indexed differences between deep sleep and wakeful resting, consistent with other studies of the human wake-sleep cycle[67–69]. In contrast, comparing meditation with resting state in expert meditators revealed regions in limbic- and default-mode- networks, similar to other findings in meditation[70–74].

Please note that the current study is based on human brain fMRI data. Thus, the time and spatial scales analysed here are restricted to the order of millimetres and seconds (low frequencies), respectively. Complementary to this approach, it would be of considerable interest to extend this analysis at different scales by considering different neuroimaging recording modalities capable of representing a much broader range of frequencies, such as Electrocorticography (ECoG), magnetoencephalography/ electroencephalography (MEG/EEG) and circuit level local field potentials.

Given the exciting results of directly perturbing the brain revealed by the pioneering studies of Massimini and colleagues[10–12], we also wanted to explore the causal mechanistic underpinnings of the differences between brain states and ensuing reactivity to external perturbations. To this end, we modelled the empirical fMRI data using Hopf whole-brain models[38,45,51,68].

The question of what level of abstraction to use in the whole-brain model is the focus of much ongoing research. Over the years, there have been many different whole-brain models with varying degree of biophysical realism, from spiking networks to mean-field to oscillatory Hopf models[43,48–52]. The conclusion that we have drawn from this work is that currently, the Hopf model creates the best fitting for fMRI BOLD data[49] with a high level of simplicity, which implies less computational cost but being cautious on the biological interpretations given the level of the abstraction of the model.

We found that the optimal working point of the Hopf whole-brain models for all brain states shifted to a lower global coupling factor compared to the resting state (see Fig. 5a). The global coupling parameter, G, represents the conductivity of the fibre densities among brain regions given by the underlying structural connectivity, which is assumed, for simplicity, to be equal across the brain[49,75]. Importantly, previous research showed that the optimal values of G and a are related by a monotonic function, so that fixing a before model fitting preserves the differences in the coupling strength parameter between states[45]. Thus, a higher coupling, G, allows the propagation of information among brain areas indirectly connected, enhancing the transmission of information across the whole network and vice versa[53]. Overall, this drastic shift toward a lower coupling indicates sub-critical behaviour suggestive of a change in the dynamical complexity underlying the brain state[75].

In other words, simply varying the global coupling, G, in the Hopf model have allowed us to obtain an excellent fit for different brain states such as psychedelics[76], DOC[53,77], anaesthesia[53] and sleep[45]. One can of course add more parameters to the Hopf model, such effective connectivity which creates an even better fit to the empirical data[78]. One can also use more sophisticated biophysical grounded models that provide a set of parameters with a different biological interpretation that could provide new insight into the differences between brain states. Nevertheless, utilising Occam's razor, we went for the minimal Hopf model that can reproduce the differences in brain states.

Using the model-based framework, crucially, we were able to perturb each brain model at its optimal working point to investigate the induced whole-brain dynamics changes caused by the external in silico perturbations in order to obtain complementary measures of information encoding in different brain states. Specifically, our external manipulation consisted of a shift towards the bifurcation point of the intrinsic local dynamics of brain areas. We found that the resting state showed significantly higher susceptibility and information encoding capability than in the pairwise comparison in each dataset, i.e., meditation, deep sleep and DOC. The similar behaviour of both measures (susceptibility and information encoding capability) can be related to the specific features of our perturbative approach. Differences in silico protocols can be assessed to study how different brain states react to external perturbations such as shifting the local dynamics in the opposite direction, node by node perturbation[78,79], non-sustained perturbations[47,80] or perturbing with external strength dependent periodic force[47,77]. Notably, the perturbative approach allows for the exploration of brain responses elicited by in silico protocols which are not limited by ethical constraints of in vivo stimulations[81,82]. Furthermore, the differential sensitivity of each brain state of external perturbations could potentially serve as a specific biomarker that reveals features of their dynamical complexity.

Overall, we have presented a unifying framework that can account for the differences between brain states. The key idea is that the complex dynamics of a brain state result from the percolation across scales of previously demonstrated differences in synchrony and complexity at the microscale. These dynamics present differentiable turbulent dynamics, in terms of spatio-temporal variability of local synchronisation, which our dual model-free and model-based framework can reveal. The main finding is that turbulent dynamics across different spatial scales can distinguish between brain states. Furthermore, these differences are also found as differences in susceptibility and information encoding capability as a result of the reactivity of different external perturbations on the underlying brain state. Given the sensitivity and specificity of the results, long-term, these might help identify potential targets for patients to rebalance and regain consciousness.

Methods
Participants
Meditation. A total of 19 experienced meditators with more than 1000 hours of meditation experience were selected from a dataset previously described in Escrichs et al. (2019)[83]. Meditators were recruited from Vipassana communities of Barcelona, Catalonia, Spain (7 females, mean ± SD, 39.8 ± 10.29 years, 9,526.9 ± 8,619.8 meditation experience). Participants were asked to practice focused attention on breathing (i.e., anapanasati in language Pali). In this meditation technique, meditators focus their attention on natural breathing, and when they realize that the mind is wandering, they must refocus their attention back to natural breathing. All participants reported no history of past neurological disorder and gave written informed consent. The study was approved by the Ethics Committee of the Bellvitge University Hospital according to the Helsinki Declaration on ethical research.

Sleep. A total of 63 healthy subjects (36 females, mean ± SD, 23 ± 43.3 years) were selected from a dataset previously described in Tagliazucchi and Laufs[84]. On the day of the study, participants reported a wake-up time between 5:00 AM and 11:00 AM and a sleep onset time between 10:00 PM and 2:00 AM for the night before the experiment. Within half an hour of 7 PM, participants entered the scanner and were asked to relax, close their eyes, and not fight the sleep onset. Their resting state activity was measured for 52 minutes with a simultaneous combination of EEG and fMRI. According to the rules of the American Academy of Sleep Medicine[85], the scalp potentials measured with EEG determine the classification of sleep into four stages (resting state, N1, N2 and N3 sleep). We selected 13 subjects who reached the deep sleep stage (DS, i.e., N3) and contiguous time series of at least 198 volumes. The local ethics committee approves the experimental protocol (Goethe-Universität Frankfurt, Germany, protocol number: 305/07), and written informed consent was asked to all participants before the experiment. The study was conducted according to the Helsinki Declaration on ethical research.

Disorders of consciousness, Paris. A total of 77 patients who were hospitalised in Paris Pitié-Salpêtrière, suffering from brain injuries, were included in this study. Clinical assessment and trained clinicians carried out the clinical assessment and Coma Recovery Scale-Revised (CRS-R) scoring to determine their state of consciousness. Patients were diagnosed with UWS if they showed arousal (opening their eyes) without any signs of awareness (never exhibiting non-reflex voluntary movements). On the other hand, patients were in a R_{MCS} if they exhibited some behaviours that could be indicative of awareness, such as visual pursuit, orientation to pain, or reproducible command following. We excluded subjects with T1 acquisition errors ($n = 5$), with high levels of motion detected ($n = 7$), registration errors ($n = 4$), and large focal brain lesions ($n = 4$). We thus included 33 patients in MCS (11 females, mean age ± SD, 47.25 ± 20.76 years), and 24 in UWS (10 females, mean age ± SD, 39.25 ± 16.30 years) and 13 healthy controls (7 females, mean age ± SD, 42.54 ± 13.64 years). This research was approved by the local ethics committee Comité de Protection des Personnes Ile de France 1 (Paris, France) under the code 'Recherche en soins courants' (NEURODOC protocol, n° 2013-A01385-40). The patient's family gave their informed consent for the participation of their relative, and all investigations were conducted according to the Declaration of Helsinki and the French regulations.

Disorders of consciousness, Liège. A total of 35 healthy controls (14 females, mean age ± SD, 40 ± 14 years) and 48 patients with disorders of consciousness (DOC) were included in the study based on a dataset previously described in López-González et al[53]. The diagnosis was made after at least 5 CRS-R by trained clinicians. The highest diagnosis of the level of consciousness was taken as the final diagnosis, which was also confirmed with Positron Emission Tomography (PET) (i.e., patients in MCS presented a relatively preserved metabolism in the fronto-parietal network while patients with UWS had a bilateral hypometabolism in this network). We thus included 33 patients in MCS (9 females, mean age ± SD, 45 ± 16 years), and 15 in UWS (6 females, mean age ± SD, 47 ± 16 years). The Ethics Committee of the Faculty of Medicine of the University of Liege approved the study protocol. The study was conducted according to the Helsinki Declaration on ethical research. Written informed consent was obtained from controls and the patients' legal surrogates.

MRI data acquisition

Meditation. MRI images were acquired on a 3 T Siemens Trio scanner (Siemens, Erlangen, Germany) using a 32-channel receiver coil. The high-resolution T1-weighted images were acquired with 208 contiguous sagittal slices; TR/TE = 1970 ms/ 2.34 ms; inversion time (IT) = 1050 ms; flip angle = 9°; FOV = 256 mm; and isotropic voxel size 1 mm. Resting-state and meditation fMRI images were performed by a single shot gradient-echo EPI sequence with a total of 450 volumes (15 min); TR/TE = 2000 ms/29 ms; FOV = 240 mm; in-plane resolution 3 mm; 32 transversal slices with thickness = 4 mm; flip angle = 80°.

Sleep. MRI images were acquired on a 3-T Siemens Trio scanner (Erlangen, Germany). EEG via a cap (modified BrainCapMR, Easycap, Herrsching, Germany) was recorded continuously during fMRI acquisition (1505 volumes of T2-weighted echo planar images, TR/TE = 2080 ms/30 ms, matrix 64 × 64, voxel size 3 × 3 × 2 mm3, distance factor 50%; FOV 192 mm²). An optimised polysomnographic setting was employed (chin and tibial EMG, ECG, EOG recorded bipolarly [sampling rate 5 kHz, low pass filter 1 kHz] with 30 EEG channels recorded with FCz as the reference [sampling rate 5 kHz, low pass filter 250 Hz]. Pulse oxymetry and respiration were recorded via sensors from the Trio [sampling rate 50 Hz]) and MR scanner compatible devices (BrainAmp MR +, BrainAmpExG; Brain Products, Gilching, Germany), facilitating sleep scoring during fMRI acquisition.

Disorders of consciousness, Paris. MRI images were acquired with two different acquisition protocols. In the first protocol, MRI data of 26 patients and 13 healthy controls were acquired on a 3T General Electric Signa System. T2*-weighted whole brain resting state images were acquired with a gradient-echo EPI sequence using axial orientation (200 volumes, 48 slices, slice thickness: 3 mm, TR/TE: 2400 ms/ 30 ms, voxel size: 3.4375 × 3.4375 × 3.4375 mm, flip angle: 90°, FOV: 220 mm²). An anatomical volume was also acquired using a T1-weighted MPRAGE sequence in the same acquisition session (154 slices, slice thickness: 1.2 mm, TR/TE: 7.112 ms/ 3.084 ms, voxel size: 1 × 1 × 1 mm, flip angle: 15°).

In the second protocol, MRI data of 51 patients were acquired on a 3 T Siemens Skyra System. T2*-weighted whole brain resting state images were recorded with a gradient-echo EPI sequence using axial orientation (180 volumes, 62 slices, slice thickness: 2.5 mm, TR/TE: 2000 ms/30 ms, voxel size: 2 × 2 × 2 mm, flip angle: 90°, FOV: 240 mm², multiband factor: 2). An anatomical volume was acquired in the same session using a T1-weighted MPRAGE sequence (208 slices, slice thickness: 1.2 mm, TR/TE: 1800 ms/2.35 ms, voxel size: 0.85 × 0.85 × 0.85 mm, flip angle: 8°).

Disorders of consciousness, Liège. MRI images were acquired on a Siemens 3 T Trio scanner (Siemens Inc, Munich, Germany). MRI acquisition included a gradient echo-planar imaging (EPI) sequence (32 transversal slices, 300 volumes, TR/ TE = 2000 ms/30 ms, flip angle = 78°, voxel size = 3x3x3 mm, FOV = 192 mm); a structural T1 (120 transversal slices, TR = 2300 ms, voxel size = 1.0 × 1.0 × 1.2 mm, flip angle = 9°, FOV = 256 mm).

Brain parcellation.

We used the Schaefer parcellation with 1000 brain areas, based on estimation from a large dataset ($n = 1489$)[86], to extract the time series from each subject. Furthermore, we estimated the Euclidean distances from the Schaefer parcellation in MNI space.

Resting-state pre-processing

For meditation, Paris, Liège datasets. The pre-processing of resting-state data was performed using FSL (http://fsl.fmrib.ox.ac.uk/fsl) as described in our previous study[53]. In brief, resting-state fMRI was computed using MELODIC (Multivariate Exploratory Linear Optimised Decomposition into Independent Components)[87]. Steps included discarding the first five volumes, motion correction using MCFLIRT[88], Brain Extraction Tool (BET)[89], spatial smoothing with 5 mm FWHM Gaussian Kernel, rigid-body registration, high pass filter cutoff = 100.0 s, and single-session ICA with automatic dimensionality estimation. Then, lesion-driven artifacts (for patients) and noise components were regressed out independently for each subject using FIX (FMRIB's ICA-based X-noiseifier)[90]. Finally, FSL tools were used to co-register the images and extract the time-series between 1000 cortical brain areas for each subject in MNI space from the Schaefer parcellation[86].

For the sleep dataset. The pre-processing of resting-state data was performed using FSL (http://fsl.fmrib.ox.ac.uk/fsl). In brief, steps included discarding the first five volumes, motion correction using MCFLIRT[88], BET[89], spatial smoothing with 5 mm FWHM Gaussian Kernel, rigid-body registration, bandpass filtering between 0.01 − 0.1 Hz. Finally, FSL tools were used to co-register the images and extract the time-series between 1000 cortical brain areas for each subject in MNI space from the Schaefer parcellation[86]. Previous publications based on this dataset can be consulted for further details[77].

Probabilistic Tractography analysis.

We used the Human Connectome Project (HCP) database that contains diffusion spectrum and T2-weighted neuroimaging data from 32 participants as reported in Deco and Kringelbach[38]. A complete description of the acquisition parameters for diffusion MRI (dMRI) is described in detail on the HCP website[91]. The freely Lead-DBS software package (https://www.lead-dbs.org/) provides the pre-processing described in detail in Horn et al.[92]. In brief, the data were processed by using a q-sampling imaging algorithm implemented in DSI studio (http://dsi-studio.labsolver.org). A white-matter mask was computed by segmenting the T2-weighted images and co-registering the images to the b0 image of the diffusion data using SPM12. For each HCP participant, 200,000 fibres were sampled within the white-matter mask. Fibres were transformed into MNI space using Lead-DBS Horn and Blankenburg[93]. Finally, we used the standardised methods in Lead-DBS to extract the structural connectomes from the Schaefer 1000 parcellation[86].

Model-free framework

Kuramoto Local order parameter. The amplitude turbulence, $R_\lambda(\bar{x}, t)$, is defined as the modulus of the Kuramoto local order parameter for a given brain area as a function of time:

$$R_\lambda(\bar{x}, t)e^{i\vartheta_\lambda(\bar{x},t)} = k \int_{-\infty}^{\infty} d\bar{x}' G_\lambda(\bar{x} - \bar{x}')e^{i\varphi(\bar{x}',t)} \tag{1}$$

where G_λ is the local weighting kernel $G_\lambda(\bar{x}) = e^{-\lambda|\bar{x}|}$, λ is the spatial scaling and $\varphi(\bar{x}, t)$ are the phases of the spatiotemporal data and k is the normalisation factor $[\int_{-\infty}^{\infty} d\bar{x}' G_\lambda(\bar{x} - \bar{x}')]^{-1}$. The empirical instantaneous phases were computed applying the Hilbert transform to the narrowband of 0.008–0.08 Hz filtered BOLD signals individually. This frequency range was chosen because it has been shown that when mapped to the grey matter, this band contains more reliable and functionally relevant information compared to other frequency bands, and is less affected by noise.[94]

Thus, R_λ defines local levels of synchronisation at a given scale, λ, as function of space, $\bar{x}$, and time, t. This measure captures what we call *brain vortex space, R_λ,* over time, inspired by the rotational vortices found in fluid dynamics, but of course not identical.

Amplitude turbulence. The level of amplitude turbulence, D_λ, is defined as the standard deviation across time and space of the modulus of local Kuramoto order parameter (R):

$$D_\lambda = \sqrt{\langle R_\lambda^2 \rangle_{x,t} - \langle R_\lambda \rangle_{x,t}^2} \tag{2}$$

where the brackets $\langle \rangle_{x,t}$ denotes averages across time and space.

Information cascade flow and Information cascade. The information cascade flow indicates how travels the information from a given scale (λ) to a lower scale ($\lambda - \Delta\lambda$, where $\Delta\lambda$ is a scale step) in consecutive time steps (t and $t + \Delta t$). In this sense, the information cascade flow measures the information transfer across scales computed as the time correlation between the Kuramoto local order parameter in two consecutive scales and times:

$$\mathscr{F}(\lambda) = \langle corr_t(R_\lambda(\bar{x}, t + \Delta t), R_{\lambda - \Delta\lambda}(\bar{x}, t)) \rangle_{\bar{x}} \tag{3}$$

where the brackets $\langle \rangle_{x,t}$ denotes averages across time and space. Then, the information cascade is obtained by averaging the information cascade flow across scales λ, which captures the whole behaviour of the information processing across scales (Fig. 1a, middle panel).

Transfer Correlation. The spatial Transfer Correlation indicates how the information travels across space at a specific scale, λ. This measurement is computed as the slope of a linear fitting in the log-log scale of the time correlation between the Kuramoto local order parameter of two brain areas at the same scale as a function of its Euclidean distance (Fig. 1a, right panel).

$$\log\left(corr_t\left(R_n^\lambda, R_p^\lambda\right)(r)\right) = A^\lambda * \log(r) + B^\lambda \tag{4}$$

Essentially, A^λ and B^λ are the fitting parameters for each scale (λ), where r is the spatial distance in brain. The negative slope (A^λ) stands for the transfer in the spatial direction r of the information in terms of time correlation of the local level of synchronisation. In this sense, when the slope is steeper, the information travels across shorter distances; while a flatter slope indicates that the information is transferred across longer distances. Thus, we define the negative slope as the *spatial transfer correlation.* Please note that in order to represent longer distances of information transmission with higher positive values, we present the results panels of Fig. 2c as a constant value minus $|A^\lambda|$.

Local node-level metastability. We define the 'local node-level metastability' as the brain region variability of the local synchronisation, measured as the standard deviation across time of the local Kuramoto order parameter:

$$NLM(n, \lambda) = \sqrt{\langle R_n^\lambda(t)^2 \rangle_t - \langle R_n^\lambda(t) \rangle_t^2} \tag{5}$$

where the brackets $< >_t$ represent average values across time points.

Here, we used the discrete version of the node-level Kuramoto order parameter, with modulus R and phase v, representing a spatial average of the complex phase factor of the local oscillators weighted by the coupling computed in the following

way:

$$R_n^\lambda(t)e^{i\nu_n(t)} = \sum_p \left[\frac{C_{np}^\lambda}{\sum_q C_{nq}^\lambda}\right] e^{i\varphi_p(t)} \tag{6}$$

where $\phi_p(t)$ are the phases of the spatiotemporal data and C_{nq}^λ is the local weighting kernel between node n and p, and λ defines the spatial scaling:

$$C_{np} = e^{-\lambda(r(n,p))} \tag{7}$$

where $r(n, q)$ is the Euclidean distance between the brain areas n and p in MNI space.

To compare the node-level metastability statistics, we collected the 1000 nodes values for all participants in each condition and generated the distributions. Then, we compared across states the distributions using the Kolmogorov-Smirnov distance between them. The Kolmogorov–Smirnov distance quantifies the maximal difference between the cumulative distribution functions of the two samples, where larger values stand for more significant differences between both distributions.

Model-based framework. We constructed whole-brain dynamical models based on the normal form of a supercritical Hopf bifurcation (also known as Stuart-Landau)[49]. This type of bifurcation can change the qualitative nature of the solutions from a limit cycle that yields self-sustained oscillations towards a stable fixed point in phase space. This whole-brain computational model is characterised by a series of model parameters that rules the global dynamical behaviour. One of them is the multiplicative factor, G, representing the global conductivity of the fibres scaling the structural connectivity between brain areas, which is assumed to be equal across the brain[49,75]. The other relevant parameters are the local bifurcation parameter (a_j), which rules the dynamical behaviour of each area between noise-induced ($a < 0$), self-sustained oscillations ($a > 0$) or a critical behaviour between both ($a \sim 0$) (Fig. 1c). We optimised the model parameters to better fit the empirical functional connectivity as a function of the distance, r, within the inertial subrange. The models consisted of 1000 cortical brain areas from the resting-state atlas mentioned above. The underlying anatomical matrix C_{np} was added to link the brain structure and functional dynamics and was obtained by measuring the exponential distance rule as defined in Eq. (7). The local dynamics of each brain area was described by the normal form of a supercritical Hopf bifurcation, which emulates the dynamics for each brain area from noisy to oscillatory dynamics as follows:

$$\frac{dx_n}{dt} = a_n x_n - [x_n^2 + y_n^2]x_n - \omega_n y_n + \nu\eta_n(t) \tag{8}$$

$$\frac{dy_n}{dt} = a_n y_n - [x_n^2 + y_n^2]y_n + \omega_n x_n + \nu\eta_n(t) \tag{9}$$

where $\eta_n(t)$ is additive Gaussian noise with standard deviation $\nu = 0.01$. This normal form has a supercritical bifurcation at $a_n = 0$, such that for $a_n > 0$, the system is in a stable limit cycle oscillation with frequency $f_n = \omega_n/2\pi$, whereas for $a_n < 0$, the local dynamics are in a stable point (i.e., noisy state). The frequency ω_n of each brain area was estimated from the empirical fMRI data as the peak of the power spectrum.

Finally, the whole-brain dynamics was defined by the following set of coupled equations:

$$\frac{dx_n}{dt} = a_n x_n - [x_n^2 + y_n^2]x_n - \omega_n y_n + G\sum_{p=1}^N C_{np}\left(x_p(t) - x_n\right) + \nu\eta_n(t) \tag{10}$$

$$\frac{dy_n}{dt} = a_n y_n - [x_n^2 + y_n^2]y_n + \omega_n x_n + G\sum_{p=1}^N C_{np}\left(y_p(t) - y_p\right) + \nu\eta_n(t) \tag{11}$$

Where the global coupling factor G, scaled equally for each brain area, represents the input received in region n from every other region p.

For the functional connectivity fitting the Kolmogorov's structure-function of a variable u was applied to the BOLD signal of the data. This measure is based on the functional correlations between each pair of brain areas with equal Euclidean distance and was defined as:

$$S(r) = \left\langle(u(\bar{x} + r) - u(\bar{x}))^2\right\rangle_{x,t} = 2[FC(0) - FC(r)] \tag{12}$$

where $FC(r)$ is the spatial correlations of two points separated by a Euclidean distance r, which is given by:

$$FC(r) = \left\langle u(\bar{x} + r)u(\bar{x})\right\rangle_{\bar{x},t} \tag{13}$$

where the symbol $\langle\rangle_{x,t}$ refers to the average across the spatial location x of the brain areas and time. Thus, the structure functions characterise the evolution of the functional connectivity (FC) as a function of the Euclidean distance between equally distant nodes, which is different from the usual definition of FC that does not include distance. We then compute the fitting as the Euclidean distance between simulated and empirical FC(r) within the inertial range as defined in Deco et al.[38].

The main implementation consists of an external perturbation represented as an external additive periodical forcing term in the Hopf brain model for each brain states as follows:

$$\frac{dx_n}{dt} = a_n x_n - [x_n^2 + y_n^2]x_n - \omega_n y_n + G\sum_{p=1}^N C_{np}\left(x_p(t) - x_n\right) + F_{0j}\cos\left(\omega_{0j}t\right) + \nu\eta_n(t) \tag{14}$$

$$\frac{dy_n}{dt} = a_n y_n - [x_n^2 + y_n^2]y_n + \omega_n x_n + G\sum_{p=1}^N C_{np}\left(y_p(t) - y_p\right) + F_{0j}\sin\left(\omega_{0j}t\right) + \nu\eta_n(t) \tag{15}$$

where ω_0 average empirical node frequency equal to all the nodes. The strength of the external periodical force was fixed at $F_{0j} = 5 \times 10^{-4}$ equally for all nodes based on previous results presented in Perl et al.[47].

In the alternative implementation we perturb the Hopf whole-brain model at each brain state by randomly changing the local bifurcation parameter, a_n, in the range $[-0.02:0]$. Note that this perturbation is carefully defined to keep the dynamical scenario in the subcritical regime of each oscillator. For further detail in this approach see Deco et al.[78].

The susceptibility measure of the whole-brain model was defined as the brain's sensitivity to react to external stimulations as it was defined in previous works[38,39]. We computed the sensitivity of the perturbations on the spatiotemporal dynamics extended the definition of previous work, which determines the susceptibility in a system of coupled oscillators based on the response of the Kuramoto order parameter[55]. The Hopf model was perturbed for each G by randomly changing the local bifurcation parameter, a_m, in the range $[-0.02: 0]$. The sensitivity of the perturbations on the spatiotemporal dynamics was calculated by measuring the modulus of the local Kuramoto order parameter as:

$$\chi = \left\langle\left\langle\left(\left\langle\widetilde{R}_{\lambda_s}(\bar{x}, t)\right\rangle_t - \left\langle R_{\lambda_s}(\bar{x}, t)\right\rangle_t\right)\right\rangle_{trials}\right\rangle_{\bar{x}} \tag{16}$$

where $\widetilde{R}_{\lambda_s}(\bar{x}, t)$ corresponds to the perturbed case, the $R_{\lambda_s}(\bar{x}, t)$ to the unperturbed case, and $\langle\rangle_t$, $\langle\rangle_{trials}$ and $\langle\rangle_x$ to the average across time, trials, and space, respectively.

The information encoding capability measures the ability of the system to encode external inputs, and such is closer related to complexity measures such as Lempel-Ziv (LZ) (used in Massimini seminal works[10,12]) or automatic complexity evaluator (ACE), and synchrony coalition entropy (SCE) (used and defined in[95]). The information capability, I, was defined as the standard deviation across trials of the difference between the perturbed $\widetilde{R}_{\lambda_s}(\bar{x}, t)$ and unperturbed $R_{\lambda_s}(\bar{x}, t)$ mean of the modulus of the local Kuramoto order parameter across time t, averaged across all brain areas n as:

$$I = \sqrt{\left\langle\left\langle\left(\left\langle\widetilde{R}_{\lambda_s}(\bar{x}, t)\right\rangle_t - \left\langle R_{\lambda_s}(\bar{x}, t)\right\rangle_t\right)^2\right\rangle_{trials}\right\rangle_{\bar{x}} - \left\langle\left\langle\left(\left\langle\widetilde{R}_{\lambda_s}(\bar{x}, t)\right\rangle_t - \left\langle R_{\lambda_s}(\bar{x}, t)\right\rangle_t\right)\right\rangle_{trials}^2\right\rangle_{\bar{x}}} \tag{17}$$

where the brackets $\langle\rangle_t$, $\langle\rangle_{trials}$ and $\langle\rangle_x$ denote the averages defined as above.

Statistical analyses. We applied the Wilcoxon rank-sum method to test the differences between conditions in Kuramoto amplitude turbulence, information capacity, transfer correlation, and perturbative measures. For the node-level analysis, we applied the Kolmogorov–Smirnov test to compare between conditions. Additionally, we applied the False Discovery Rate (FDR) at the 0.05 level of significance to correct multiple comparisons[96].

Reporting summary. Further information on research design is available in the Nature Research Reporting Summary linked to this article.

Data availability
Sleep and meditation time-series are publicly available on https://github.com/aescrichs/brainstates-turbulence/releases. The disorders of consciousness datasets contain information from a clinical population and are not publicly available due to constraints imposed by the currently approved ethics protocol, however the data can be requested to the Authors.

Code availability
All code written in support of this is publicly available on https://github.com/aescrichs/brainstates-turbulence.

References

1. Goldman, J. S. et al. Bridging single neuron dynamics to global brain states. *Front. Syst. Neurosci.* **13**, 75 (2019).
2. Kringelbach, M. L. & Deco, G. Brain states and transitions: insights from computational neuroscience. *Cell Rep.* **32**, 108128 (2020).
3. Gervasoni, D. et al. Global forebrain dynamics predict rat behavioral states and their transitions. *J. Neurosci.* **24**, 11137–11147 (2004).
4. Deco, G., Tononi, G., Boly, M. & Kringelbach, M. L. Rethinking segregation and integration: contributions of whole-brain modelling. *Nat. Rev. Neurosci.* **16**, 430–439 (2015).
5. Carhart-Harris, R. L. et al. Neural correlates of the LSD experience revealed by multimodal neuroimaging. *Proc. Natl Acad. Sci.* **113**, 4853–4858 (2016).
6. McCormick, D. A., Nestvogel, D. B. & He, B. J. Neuromodulation of brain state and behavior. *Annu. Rev. Neurosci.* **43**, 391–415 (2020).
7. Northoff, G. What the brain's intrinsic activity can tell us about consciousness? A tri-dimensional view. *Neurosci. Biobehav. Rev.* **37**, 726–738 (2013).
8. Tagliazucchi, E., Crossley, N., Bullmore, E. T. & Laufs, H. Deep sleep divides the cortex into opposite modes of anatomical–functional coupling. *Brain Struct. Funct.* **221**, 4221–4234 (2016).
9. Tononi, G., Sporns, O. & Edelman, G. M. A measure for brain complexity: relating functional segregation and integration in the nervous system. *Proc. Natl Acad. Sci.* **91**, 5033–5037 (1994).
10. Casali, A. G. et al. A theoretically based index of consciousness independent of sensory processing and behavior. *Sci. Transl. Med.* **5**, 198ra105–198ra105 (2013).
11. Ferrarelli, F. et al. Breakdown in cortical effective connectivity during midazolam-induced loss of consciousness. *Proc. Natl Acad. Sci.* **107**, 2681–2686 (2010).
12. Massimini, M. et al. Breakdown of cortical effective connectivity during sleep. *Science* **309**, 2228–2232 (2005).
13. Steriade, M., Nunez, A. & Amzica, F. A novel slow (<1 Hz) oscillation of neocortical neurons in vivo: depolarizing and hyperpolarizing components. *J. Neurosci.* **13**, 3252–3265 (1993).
14. Brown, E. N., Lydic, R. & Schiff, N. D. General anesthesia, sleep, and coma. *N. Engl. J. Med.* **363**, 2638–2650 (2010).
15. Sanchez-Vives, M. V. & McCormick, D. A. Cellular and network mechanisms of rhythmic recurrent activity in neocortex. *Nat. Neurosci.* **3**, 1027–1034 (2000).
16. Fox, M. The human brain is intrinsically organized into dynamics, anticorrelated functional networks. *Proc. Natl Acad. Sci. USA* **102**, 9673–9678 (2005).
17. Henry, J. C. Electroencephalography: basic principles, clinical applications, and related fields, fifth edition. *Neurology* **67**, 2092–2092-a (2006).
18. Raichle, M. E. et al. A default mode of brain function. *Proc. Natl Acad. Sci.* **98**, 676–682 (2001).
19. Boly, M. et al. Intrinsic brain activity in altered states of consciousness: how conscious is the default mode of brain function? *Ann. N. Y. Acad. Sci.* **1129**, 119 (2008).
20. Tononi, G. & Edelman, G. M. Consciousness and complexity. *Science* **282**, 1846–1851 (1998).
21. Sitt, J. D. et al. Large scale screening of neural signatures of consciousness in patients in a vegetative or minimally conscious state. *Brain* **137**, 2258–2270 (2014).
22. El Boustani, S. & Destexhe, A. Brain dynamics at multiple scales: can one reconcile the apparent low-dimensional chaos of macroscopic variables with the seemingly stochastic behavior of single neurons? *Int. J. Bifurc. Chaos* **20**, 1687–1702 (2010).
23. Steriade, M. Corticothalamic resonance, states of vigilance and mentation. *Neuroscience* **101**, 243–276 (2000).
24. Huber, R., Felice Ghilardi, M., Massimini, M. & Tononi, G. Local sleep and learning. *Nature* **430**, 78–81 (2004).
25. Frisch, U. Turbulence: The Legacy of A. N. Kolmogorov. *Cambridge Univ. Press* (1995).
26. Kolmogorov, N. A. Dissipation of energy in the locally isotropic turbulence. *C. R. Acad. Sci. URSS* **32**, 16–18 (1941).
27. Kolmogorov, N. A. The local structure of turbulence in incompressible viscous fluid for very large Reynolds numbers. *C. R. Acad. Sci. URSS* **30**, 301–305 (1941).
28. Kuramoto, Y. *Chemical Oscillations, Waves, and Turbulence.* (Springer-Verlag, 1984).
29. Cross, M. C. & Hohenberg, P. C. Pattern formation outside of equilibrium. *Rev. Mod. Phys.* **65**, 851 (1993).
30. Oono, Y. & Yeung, C. A cell dynamical system model of chemical turbulence. *J. Stat. Phys. 1987 483* **48**, 593–644 (1987).
31. Landau, L. D. & Lifshitz, E. M. *Fluid mechanics, vol. Course of Theoretical Physics Volume 6 (2nd revised ed.).* (Pergamon Press, ISBN 978-0-08-033932-0, OCLC 15017127, 1987).
32. Tognoli, E. & Kelso, J. A. S. The metastable brain. *Neuron* **81**, 35–48 (2014).
33. Wildie, M. & Shanahan, M. Metastability and chimera states in modular delay and pulse-coupled oscillator networks. *Chaos Interdiscip. J. Nonlinear Sci.* **22**, 043131 (2012).
34. Cabral, J. et al. Exploring mechanisms of spontaneous functional connectivity in MEG: How delayed network interactions lead to structured amplitude envelopes of band-pass filtered oscillations. *Neuroimage* **90**, 423–435 (2014).
35. Shanahan, M. Metastable chimera states in community-structured oscillator networks. *Chaos Interdiscip. J. Nonlinear Sci.* **20**, 013108 (2010).
36. Kitzbichler, M. G., Smith, M. L., Christensen, S. R. & Bullmore, E. Broadband criticality of human brain network synchronization. *PLOS Comput. Biol.* **5**, e1000314 (2009).
37. Deco, G., Kemp, M. & Kringelbach, M. L. Leonardo da Vinci and the search for order in neuroscience. *Curr. Biol.* **31**, R704–R709 (2021).
38. Deco, G. & Kringelbach, M. L. Turbulent-like dynamics in the human brain. *Cell Rep.* **33**, 108471 (2020).
39. Deco, G. et al. Rare long-range cortical connections enhance human information processing. *Curr. Biol.* https://doi.org/10.1016/J.CUB.2021.07.064 (2021).
40. Kawamura, Y., Nakao, H. & Kuramoto, Y. Noise-induced turbulence in nonlocally coupled oscillators. *Phys. Rev. E.* **75**, 036209. https://doi.org/10.1103/PhysRevE.75.036209 (2007).
41. Hunt, J. C. R. & Vassilicos, J. C. *Turbulence Structure and Vortex Dynamics.* (Cambridge University Press, 2001).
42. Breakspear, M., Jirsa, V. & Deco, G. Computational models of the brain: from structure to function. *Neuroimage* **52**, 727–730 (2010).
43. Honey, C. J., Kötter, R., Breakspear, M. & Sporns, O. Network structure of cerebral cortex shapes functional connectivity on multiple time scales. *Proc. Natl Acad. Sci. USA* **104**, 10240–10245 (2007).
44. Ghosh, A., Rho, Y., McIntosh, A. R., Kötter, R. & Jirsa, V. K. Cortical network dynamics with time delays reveals functional connectivity in the resting brain. *Cogn. Neurodyn* **2**, 115–120 (2008).
45. Jobst, B. M. et al. Increased stability and breakdown of brain effective connectivity during slow-wave sleep: mechanistic Insights from whole-brain computational modelling. *Sci. Rep.* **7**, 1–16 (2017).
46. Breakspear, M. Dynamic' connectivity in neural systems: theoretical and empirical considerations. *Neuroinformatics* **2**, 205–224 (2004).
47. Perl, Y. S., Escrichs, A., Tagliazucchi, E., Kringelbach, M. L. & Deco, G. On the edge of criticality: strength-dependent perturbation unveils delicate balance between fluctuation and oscillation in brain dynamics. https://doi.org/10.1101/2021.09.23.461520 (2021).
48. Deco, G. & Jirsa, V. K. Ongoing cortical activity at rest: criticality, multistability, and ghost attractors. *J. Neurosci.* **32**, 3366–3375 (2012).
49. Deco, G., Kringelbach, M. L., Jirsa, V. K. & Ritter, P. The dynamics of resting fluctuations in the brain: metastability and its dynamical cortical core. *Sci. Rep.* **7**, 1–14 (2017).
50. Freyer, F., Roberts, J. A., Ritter, P. & Breakspear, M. A canonical model of multistability and scale-invariance in biological systems. *PLOS Comput. Biol.* **8**, e1002634 (2012).
51. Ghosh, A., Rho, Y., McIntosh, A. R., Kötter, R. & Jirsa, V. K. Noise during rest enables the exploration of the brain's dynamic repertoire. *PLoS Comput. Biol.* **4**, e1000196 (2008).
52. Deco, G. et al. How local excitation–inhibition ratio impacts the whole brain dynamics. *J. Neurosci.* **34**, 7886–7898 (2014).
53. López-González, A. et al. Loss of consciousness reduces the stability of brain hubs and the heterogeneity of brain dynamics. *Commun. Biol.* **4**, 1–15 (2021).
54. Nakao, H. Complex Ginzburg-Landau equation on networks and its non-uniform dynamics. *Eur. Phys. J. Spec. Top.* **223**, 2411–2421 (2014).
55. Daido, H. Susceptibility of large populations of coupled oscillators. *Phys. Rev. E* **91**, 012925 (2015).
56. Lempel, A. & Ziv, J. On the complexity of finite sequences. *IEEE Trans. Inf. Theory* **22**, 75–81 (1976).
57. King, J. R. et al. Information sharing in the brain indexes consciousness in noncommunicative patients. *Curr. Biol.* **23**, 1914–1919 (2013).
58. Casarotto, S. et al. Stratification of unresponsive patients by an independently validated index of brain complexity. *Ann. Neurol.* **80**, 718–729 (2016).
59. Bodart, O. et al. Measures of metabolism and complexity in the brain of patients with disorders of consciousness. *NeuroImage Clin.* **14**, 354–362 (2017).
60. Dehaene, S. & Changeux, J. P. Experimental and theoretical approaches to conscious processing. *Neuron* **70**, 200–227 (2011).
61. Tagliazucchi, E. & van Someren, E. J. W. The large-scale functional connectivity correlates of consciousness and arousal during the healthy and pathological human sleep cycle. *Neuroimage* **160**, 55–72 (2017).
62. Tagliazucchi, E. et al. Breakdown of long-range temporal dependence in default mode and attention networks during deep sleep. *Proc. Natl Acad. Sci.* **110**, 15419–15424 (2013).
63. Qin, P. et al. How are different neural networks related to consciousness? *Ann. Neurol.* **78**, 594–605 (2015).
64. Bodien, Y. G., Chatelle, C. & Edlow, B. L. Functional networks in disorders of consciousness. *Semin. Neurol.* **37**, 485–502 (2017).
65. Demertzi, A. et al. Intrinsic functional connectivity differentiates minimally conscious from unresponsive patients. *Brain* **138**, 2619–2631 (2015).

66. Fernández-Espejo, D. et al. A role for the default mode network in the bases of disorders of consciousness. *Ann. Neurol.* **72**, 335–343 (2012).

67. Horovitz, S. G. et al. Decoupling of the brain's default mode network during deep sleep. *Proc. Natl Acad. Sci.* **106**, 11376–11381 (2009).

68. Ipiña, I. P. et al. Modeling regional changes in dynamic stability during sleep and wakefulness. *Neuroimage* **215**, 116833 (2020).

69. Stevner, A. B. A. et al. Discovery of key whole-brain transitions and dynamics during human wakefulness and non-REM sleep. *Nat. Commun.* **10**, 1–14 (2019).

70. De Filippi, E. et al. Meditation-induced effects on whole-brain structural and effective connectivity. *Brain Struct. Funct.* **1**, 1–16 (2022).

71. Tang, Y.-Y., Hölzel, B. K. & Posner, M. I. The neuroscience of mindfulness meditation. *Nat. Rev. Neurosci.* **16**, 213–225 (2015).

72. Taylor, V. A. et al. Impact of meditation training on the default mode network during a restful state. *Soc. Cogn. Affect. Neurosci.* **8**, 4–14 (2013).

73. Hasenkamp, W. & Barsalou, L. W. Effects of meditation experience on functional connectivity of distributed brain networks. *Front. Hum. Neurosci.* **0**, 38 (2012).

74. Hasenkamp, W., Wilson-Mendenhall, C. D., Duncan, E. & Barsalou, L. W. Mind wandering and attention during focused meditation: A fine-grained temporal analysis of fluctuating cognitive states. *Neuroimage* **59**, 750–760 (2012).

75. Deco, G., Tagliazucchi, E., Laufs, H., Sanjuán, A. & Kringelbach, M. L. Novel intrinsic ignition method measuring local-global integration characterizes wakefulness and deep sleep. *eNeuro* **4**, 1–12 (2017).

76. Cruzat, J. et al. Effects of classic psychedelic drugs on turbulent signatures in brain dynamics. *Netw. Neurosci.* 1–21 https://doi.org/10.1162/NETN_A_00250 (2022).

77. Perl, Y. S. et al. Perturbations in dynamical models of whole-brain activity dissociate between the level and stability of consciousness. *PLOS Comput. Biol.* **17**, e1009139 (2021).

78. Deco, G. et al. Awakening: Predicting external stimulation to force transitions between different brain states. *Proc. Natl Acad. Sci. USA* **116**, 18088–18097 (2019).

79. Escrichs, A. et al. The effect of external stimulation on functional networks in the aging healthy human brain. *Cereb. Cortex* https://doi.org/10.1093/CERCOR/BHAC064 (2022).

80. Deco, G. et al. Perturbation of whole-brain dynamics in silico reveals mechanistic differences. *Neuroimage* **169**, 46–56 (2018).

81. Clausen, J. Ethical brain stimulation – neuroethics of deep brain stimulation in research and clinical practice. *Eur. J. Neurosci.* **32**, 1152–1162 (2010).

82. Kringelbach, M. L., Jenkinson, N., Owen, S. L. F. & Aziz, T. Z. Translational principles of deep brain stimulation. *Nat. Rev. Neurosci.* **8**, 623–635 (2007).

83. Escrichs, A. et al. Characterizing the dynamical complexity underlying meditation. *Front. Syst. Neurosci.* **13**, 27 (2019).

84. Tagliazucchi, E. & Laufs, H. Decoding wakefulness levels from typical fMRI resting-state data reveals reliable drifts between wakefulness and sleep. *Neuron* **82**, 695–708 (2014).

85. Berry, R. B. et al. AASM | Scoring Manual Version 2.2. The AASM manual for the scoring of sleep and associated events. Rules, terminology and technical specifications. *Am. Acad. Sleep Med.* **176**, 16–31 (2015).

86. Schaefer, A. et al. Local-global parcellation of the human cerebral cortex from intrinsic functional connectivity MRI. *Cereb. Cortex* **28**, 3095–3114 (2018).

87. Beckmann, C. F. & Smith, S. M. Probabilistic independent component analysis for functional magnetic resonance imaging. *IEEE Trans. Med. Imaging* **23**, 137–152 (2004).

88. Jenkinson, M., Bannister, P., Brady, M. & Smith, S. Improved optimization for the robust and accurate linear registration and motion correction of brain images. *Neuroimage* **17**, 825–841 (2002).

89. Smith, S. M. Fast robust automated brain extraction. *Hum. Brain Mapp.* **17**, 143–155 (2002).

90. Griffanti, L. et al. ICA-based artefact removal and accelerated fMRI acquisition for improved resting state network imaging. *Neuroimage* **95**, 232–247 (2014).

91. Setsompop, K. et al. Pushing the limits of in vivo diffusion MRI for the Human Connectome Project. *Neuroimage* **80**, 220–233 (2013).

92. Horn, A., Neumann, W. J., Degen, K., Schneider, G. H. & Kühn, A. A. Toward an electrophysiological "Sweet spot" for deep brain stimulation in the subthalamic nucleus. *Hum. Brain Mapp.* **38**, 3377–3390 (2017).

93. Horn, A. & Blankenburg, F. Toward a standardized structural–functional group connectome in MNI space. *Neuroimage* **124**, 310–322 (2016).

94. Glerean, E., Salmi, J., Lahnakoski, J. M., Jääskeläinen, I. P. & Sams, M. Functional magnetic resonance imaging phase synchronization as a measure of dynamic functional connectivity. *Brain Connect.* **2**, 91–101 (2012).

95. Schartner, M. M. et al. Global and local complexity of intracranial EEG decreases during NREM sleep. *Neurosci. Conscious.* **2017**, 1–12 (2017).

96. Hochberg, Y. & Benjamini, Y. More powerful procedures for multiple significance testing. *Stat. Med.* **9**, 811–818 (1990).

Author contributions

Conceptualisation: A.E., Y.S., M.L.K. and G.D. Methodology: A.E., Y.S., M.L.K. and G.D. Data analysis: A.E. and Y.S. Visualisation: A.E., Y.S., M.L.K. and G.D. Supervision: M.L.K. and G.D. Data preprocessing: A.E., C.P., A.L.G. and M.L.K. Data curation: E.C., B.T., N.P., R.P., J.A., O.G., S.L., L.N., J.D.S., H.L., E.T. and M.L.K. Writing—original draft: A.E., Y.S., M.L.K. and G.D. Writing—review & editing: C.U., E.C., A.L.G., J.D.S., E.T., O.G. and L.N.

Competing interests

E.T. is an Editorial Board Member for *Communications Biology*, but was not involved in the editorial review of, nor the decision to publish this article. The remaining authors declare no competing interests.

Additional information

Supplementary information The online version contains supplementary material available at https://doi.org/10.1038/s42003-022-03576-6.

Correspondence and requests for materials should be addressed to Anira Escrichs, Yonatan Sanz Perl, Morten L. Kringelbach or Gustavo Deco.

Peer review information *Communications Biology* thanks the anonymous reviewers for their contribution to the peer review of this work. Primary Handling Editors: Karli Montague-Cardoso and Christina Karlsson Rosenthal.

Reprints and permission information is available at http://www.nature.com/reprints

Publisher's note Springer Nature remains neutral with regard to jurisdictional claims in published maps and institutional affiliations.

Chapter 5

DISCUSSION

We have proposed and tested whole-brain computational frameworks for characterising and distinguishing different brain states. Specifically, we have used model-free and model-based approaches combined with resting state fMRI and DTI neuroimaging techniques to demonstrate that different brain dynamics levels differentiate between brain states, whether in health or disease. We have shown that different brain states can be characterised by their underlying dynamical complexity. Furthermore, using tools from turbulence theory, we have demonstrated that turbulent dynamics over different spatial scales differentiate between brain states. Significantly, we were able to differentiate low-level states of consciousness, specifically between deep sleep and DoC states. Such states revealed distinct and unique features in their underlying turbulent brain dynamics. Moreover, we show that a whole-brain model can be fitted to different brain states and can be used to study *in silico* the sensitivity and capacity of each brain area to promote a transition, e.g., from disease to health. Finally, *in silico* perturbations of this model can be used to measure the brain's reactivity under different conscious and unconscious brain states.

5.1 Brain states can be characterised by their underlying dynamical complexity

In Article 1, we applied a model-free approach (i.e., the intrinsic ignition framework) to study dynamical complexity differences among meditators and healthy controls during resting state and meditation using fMRI. We found that the spatiotemporal dynamics across the whole-brain functional network for the meditation state showed less complexity than during the resting state in expert meditators but not in healthy controls. This result aligns with recent meditation studies on information propagation across the brain. For example, a study using electroencephalography (EEG) revealed a transition from more complex brain dynamics at rest to a state of reduced propagation of information during meditation, notably, only in expert meditators [Irrmischer et al., 2018]. Similarly, Toutain and colleagues found that the evolution of the topological patterns in the functional networks of experienced meditators is more stable in the meditative state than in the resting state [Toutain et al., 2020].

In addition, we showed that meditators exhibited higher metastability at rest than the control group, indicating that the underlying brain dynamics are more complex in expert meditators than in controls when they are not engaged in a specific task. This result is congruent with the increased temporal complexity of oscillations during rest in meditators reported using EEG [Irrmischer et al., 2018]. Moreover, it has been shown that individuals with high trait mindfulness transitioned more frequently between brain states at rest [Lim et al., 2018, Marusak et al., 2018]. These results are in line with brain dynamics theories, which suggest that metastability (characterised by a flexible and fast dynamic repertoire of brain states) is the optimal state of neural activity at rest [Tognoli and Kelso, 2014].

Altogether, we demonstrated that the meditation state operates in a different dynamical regime than the resting state. Furthermore, we show that experienced meditators can alter whole-brain dynamics when immersed in a meditative state and that expertise in meditation leads to increased ignition and metastability at rest. These results indicate

that expert meditators can modulate the brain's dynamical repertoire, restricting it during meditation and enhancing it during rest.

In *Article 2*, we used a large resting state fMRI dataset of healthy participants to study the dynamical complexity in different age groups by applying two model-free approaches (i.e., the intrinsic ignition and PMS frameworks). First, we computed the intrinsic ignition framework to characterise the spatiotemporal dynamics of each group across the whole-brain network. We found that the older participants exhibited higher ignition but lower metastability across the whole-brain functional network, indicating that the brain network is more integrated, slower, and less flexible in older participants than in middle-aged participants. These results are in line with previous investigations reporting increased connectivity in older adults between resting state networks [Geerligs et al., 2015, Betzel et al., 2014, Spreng et al., 2016]. Here, though, we postulate that increased functional connectivity between resting state networks in ageing significantly impacts the whole-brain functional network, as evidenced by the level of intrinsic ignition.

We also measured the intrinsic ignition and metastability within eight well-known resting state networks (DMN, frontoparietal, medial frontal, motor, subcortical and visual networks). We found that the older group showed higher ignition and metastability in the frontoparietal and medial frontal networks. This result is in line with previous studies revealing that frontal and temporal lobes show a more dynamic pattern with increasing age [Lou et al., 2019, Li et al., 2015]. Overactivation in prefrontal brain areas has often been observed in older adults, giving rise to different theories [Cabeza et al., 2018, Davis et al., 2008, Naik et al., 2017] such as, for example, a compensatory mechanism to delay cognitive decline [Cabeza et al., 2018]. However, recent evidence suggests that increased frontal activity can be related to reduced efficiency more than to compensation [Morcom and Henson, 2018]. Nevertheless, why this overactivation occurs remains unknown.

Secondly, we applied the PMS framework and identified a metastable substate overlapping with the so-called 'rich club' [Hagmann et al., 2008, van den Heuvel and Sporns, 2011, van den Heuvel et al., 2012, Sporns, 2013]. We show that this metastable substate was less likely to occur in the older group than in the middle-aged group and that when it did

occur, it did so for shorter periods of time. The rich club mediates communication and information transmission among functional networks, and it is thought that it coordinates interactions with lower-degree regions as well as the emergence of different functional resting state network configurations [van den Heuvel and Sporns, 2011]. The lower probability of occurrence and duration of this state in the older group could be due to disruptions in its underlying dynamics or any of their brain areas. Rich club regions play a crucial role in transmitting information across the brain network. Consequently, a disruption in one of these key areas can affect global communication across the functional network that could impact cognitive domains [van den Heuvel and Sporns, 2011, Baggio et al., 2015]. Our results are consistent with the previous findings showing that the efficiency of the rich club architecture increases during development and decreases with age, showing an inverted U when plotted across the lifespan [Cao et al., 2014, Zhao et al., 2015, Damoiseaux, 2017].

Going radically beyond the characterisation of the empirical PMS, which provides essential model-free information on the differences given by the dynamics, in *Article 3*, we simulate the PMS of the older group with a causal whole-brain model to provide mechanistic information on how to reverse age-induced changes in brain dynamics. This result is explained in *section 5.3* of this chapter.

Finally, we combined the intrinsic ignition and PMS frameworks by computing the ignition and metastability within the metastable substate (i.e., rich club) and found that the older group showed lower values in ignition and metastability than the middle-aged group. This demonstrated that even if older subjects present overactivation in frontal areas and frontoparietal and medial frontal networks, they show reduced capacity, integration and metastability in a state which is crucial for efficient transmission of information in the brain. We hypothesise that overactivation found in older subjects could be due to disruption among rich club nodes rather than a compensatory mechanism, as previously reported in the literature. Thus, one possibility could be that older subjects spend more time in frontal networks because these nodes have become less efficient with ageing, reducing their brain's ability to switch among functional networks.

Altogether, using model-free frameworks, we have extracted specific local-global and spatiotemporal features from empirical resting state fMRI

data. Furthermore, we have shown that different states can be characterised by their underlying dynamical complexity, showing higher or lower levels of complexity across the whole-brain network and within resting state networks.

5.2 Different brain states show dissociable turbulent dynamics across space-time scales

In *Article 4*, we measured the dynamics of information transmission across spacetime scales using the turbulence model-free framework. This framework allowed us to describe and characterise different brain states, whether they are naturally occurring (sleep, awake), temporarily induced (meditation) or caused by brain injuries (unresponsive wakefulness and minimally consciousness states).

We demonstrated that the measure of turbulence is highly sensitive for discerning between brain states. Specifically, in DoC patients (i.e., MCS and UWS), we observed lower levels of turbulence at lower spatial scales λ (i.e., long distances in the brain) but higher levels of turbulence at higher spatial scales (i.e., short distances in the brain) compared to the resting state **(Figure 5.1)**. Furthermore, the turbulence measure distinguished between MCS and UWS patients. These results are consistent with EEG evidence showing that non-communicative patients have lower global information sharing [King et al., 2013] and decreased brain complexity [Casarotto et al., 2016, Bodart et al., 2017]. This also aligns with the global neuronal workspace theory, which proposes that long-distance connections globally broadcast the information for different processors brain-wide, and this lack of spatially bounded information processing is associated with conscious access [Dehaene and Changeux, 2011]. Here, we extended these findings by showing that DoC patients exhibit higher turbulence levels over short distances in the brain. In healthy participants, deep sleep was characterised by lower turbulence across all spatial scales compared to the resting state; that is, it showed reduced information processing over short and long distances [Tagliazucchi et al.,
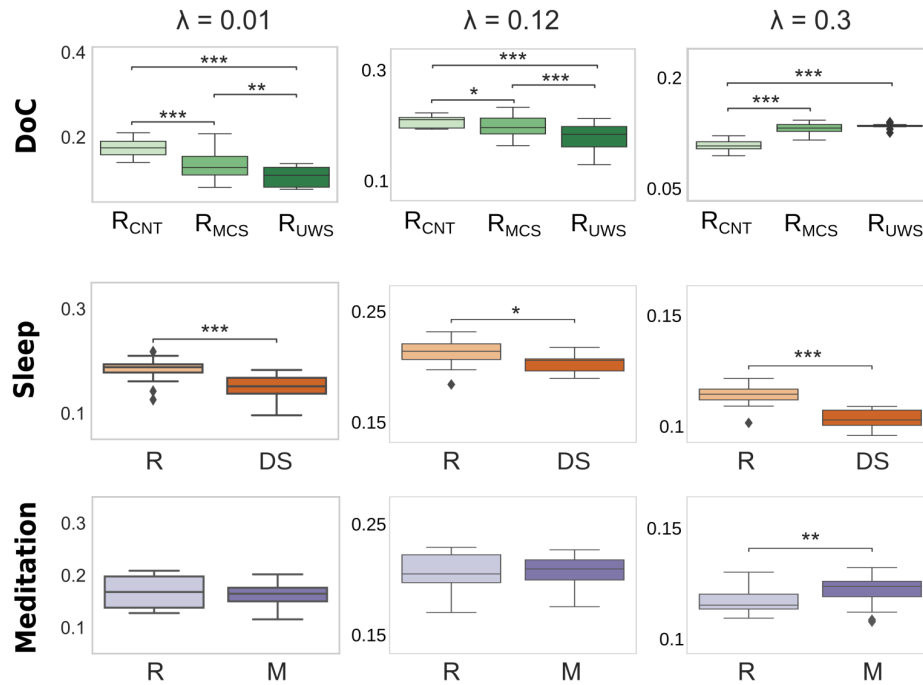
Figure 5.1: Evolution of turbulence on different brain states. The plots show the level of turbulence at different spatial scales ($\lambda = 0.01$, $\lambda = 0.12$ and $\lambda = 0.3$). The level of turbulence showed significant decreases in MCS and UWS states at lower lambda scales but significant increases at higher scales compared to controls. Deep sleep showed significantly lower turbulence levels than the resting state across all spatial scales. By contrast, the meditation state showed significant increases in turbulence compared to the resting state only at higher scales.

2013]. In contrast, the meditation state presented higher turbulence levels only at lower spatial scales (short distances in the brain and higher λ values) compared to the resting state.

One of the most noteworthy results of this study was that we observed specific and unique features of turbulent dynamics underlying low-level states of consciousness. Specifically, the measure of turbulence differentiated between deep sleep and DoC states over shorter distances in the brain.

78

In particular, the deep sleep state showed lower turbulence than the resting state across all the spatial scales. In contrast, for DoC states, turbulence decreased over long distances but increased over short distances.

Furthermore, working in the 'vortex space', we assessed three additional measures for each brain state: information transfer, information cascade flow and information cascade (see Methods chapter). We found that information transfer rose significantly with the spatial scale between the resting state and the level of awareness in the other brain states (meditation, deep sleep, MCS and UWS). The information cascade flow monotonically declined with short distances (the increase in the spatial scale λ) for all brain states. This measure also discriminated between conditions, i.e., showing lower values for DoC patients than for control participants and in the deep sleep stage compared to the resting state in the same participants. The information cascade (i.e., the average of the information flow across scales) is lower in low-level states of awareness (deep sleep, MCS and UWS) than in the normal resting state. This demonstrates that the information transmission is altered with conscious access and that this is captured with the global information processing measures of information transmission, information cascade flow and information cascade.

Overall, using tools from turbulence theory applied to empirical fMRI data, we have demonstrated that each brain state exhibits different turbulent dynamic patterns across spatial scales, allowing us to characterise the brain states from their underlying information processing fluctuations.

5.3 *In silico* perturbation protocols based on causal whole-brain models

Previous studies using TMS combined with EEG have successfully shown that different conscious and unconscious brain states react in a significantly different way after perturbing the cerebral cortex [Massimini et al., 2005, Ferrarelli et al., 2010, Casali et al., 2013]. However, given the ethical constraints of experimental neurostimulation in humans, *in silico* perturbation protocols based on causal whole-brain computational models are essential to obtaining a mechanistic understanding of brain dynamics. Thus, we sought to study how different brain states react to external

artificial perturbations from a mechanistic point of view, which allows us to systematically assess the induced whole-brain dynamics changes caused by these perturbations. To this end, we modelled the empirical fMRI data for different brain states using Hopf whole-brain models and then tested two types of external perturbations (previously described in the Methods chapter). On the one hand, in *Article 3*, we applied *in silico* perturbations in order to predict optimal stimulation targets to force a transition from the states of the older group to the states of the middle-aged group. On the other hand, in *Article 4*, we used *in silico* perturbations to measure the brain's reactivity to external perturbations in conscious and unconscious brain states.

Forcing a brain state transition

In *Article 3*, we used the Hopf model to provide mechanistic information on how to reverse age-induced changes in brain dynamics. We aimed to determine the causal mechanisms capable of explaining how to force a transition between brain states of different age groups. This strategy allowed us to address the fundamental question in modern neuroscience of how the brain transitions between different states and, in addition, to find optimal stimulation targets to rebalance the underlying brain dynamics in the elderly towards more healthy states.

We fitted the brain states of the older group (i.e., the PMS) to the Hopf model to study exhaustively *in silico*, i.e., region by region, how to force a transition from the brain states associated with the older group to the brain states of the middle-aged group. This theoretical framework allowed us to force a transition using external stimulation, similar to deep brain stimulation (DBS) or transcranial magnetic stimulation (TMS) [Deco et al., 2019].

We tested two different stimulation protocols, namely synchronisation and noise. The synchronisation protocol increases the value of the bifurcation parameter of the stimulated node, resulting in oscillatory behaviour, whereas the noise protocol yields the opposite effect. We found that the noise protocol led to better results **(Figure 5.2)**. This effect could be related to brain overactivation in the elderly, widely reported in the literature. Notably, it has been shown that older adults exhibit overactivation
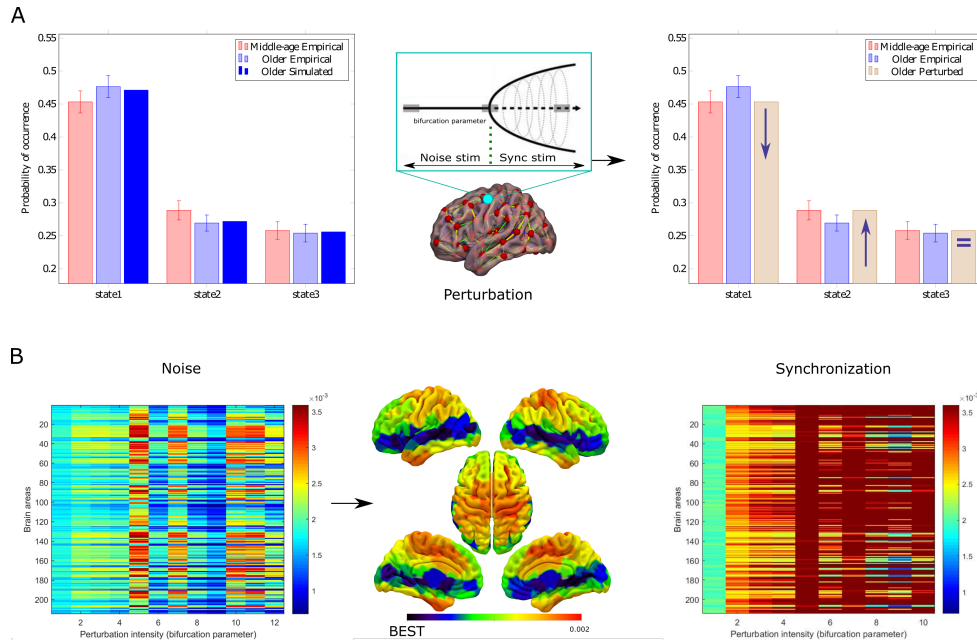
Figure 5.2: Forcing transitions between brain states. **A)** Forcing transitions from the model of the older group (electric blue) to the empirical PMS of the middle-aged group (red). The whole-brain model was perturbed using two different protocols (noise and synchronisation), which shifted the local bifurcation parameter of each brain area to negative and positive values, respectively (middle panel). The optimal perturbation is that which causes the first state to decrease, the second state to increase, and the third state to remain similar (right panel). **B)** The left matrix shows the KL-distance value after applying the noise protocol's perturbation intensity in each brain area (from softer to stronger). This protocol presented the best usefulness since KL distances were minimal in some brain areas. The brain rendered onto the cortex shows in blue the optimal brain areas to induce the transitions. The colour scale represents the KL distance between the PMS of the middle-aged group and the perturbed model using the noise protocol. The right matrix shows that the synchronisation protocol presented poor effectiveness given that KL distances were longer than in the noise protocol.

in frontal brain areas and among resting state networks [Davis et al., 2008, Reuter-Lorenz and Cappell, 2008, Betzel et al., 2014, Geerligs et al.,

2015, Spreng et al., 2016, Cabeza et al., 2018, Escrichs et al., 2022b]. Thus, one possible explanation could be that adding noise in specific brain areas decreases these functional overactivations. Finally, we found that forcing a shift in the intrinsic local dynamics of the right precuneus as well as other brain areas belonging to the rich club (insula, putamen, caudate, and thalamus) was suitable for forcing an optimal transition to the middle-aged regime.

Overall, we provide causal evidence that external stimulations in specific local brain areas can reshape whole-brain dynamics in the normal ageing process. This strategy can contribute to developing neurostimulation treatments to reverse or slow down cognitive decline. Furthermore, the differential sensitivity of each brain area to external perturbations serves not only for the design of neurostimulation therapies but crucially as a more specific model-biomarker relating local brain activity with global brain dynamics.

Measuring the brain's reactivity for different brain states

In *Article 4*, we used the Hopf model to study the susceptibility and information encoding capability measures to assess the reactivity of the brain to external perturbations. We fitted a Hopf whole-brain model for each brain state (wakefulness, meditation, deep sleep, MCS and UWS) and found that the optimal working point of the models for all brain states shifted to a lower global coupling parameter compared to the resting state **(Figure 5.3.A)**. The global coupling factor, G, represents the global conductivity of the fibre densities among brain areas given by the underlying structural connectivity matrix, which is here, for simplicity, scaled uniformly across the brain [Deco et al., 2017b, Deco et al., 2017a].

Then, we perturbed each brain model at its optimal working point (i.e., the optimal model fitting G) to investigate the induced whole-brain dynamics changes caused by the external perturbations. Specifically, the perturbation consisted of shifting towards the bifurcation point of the intrinsic local dynamics of all brain areas. We found that the resting state showed significantly higher susceptibility and information encoding capability than the other brain states studied, i.e., meditation, deep sleep
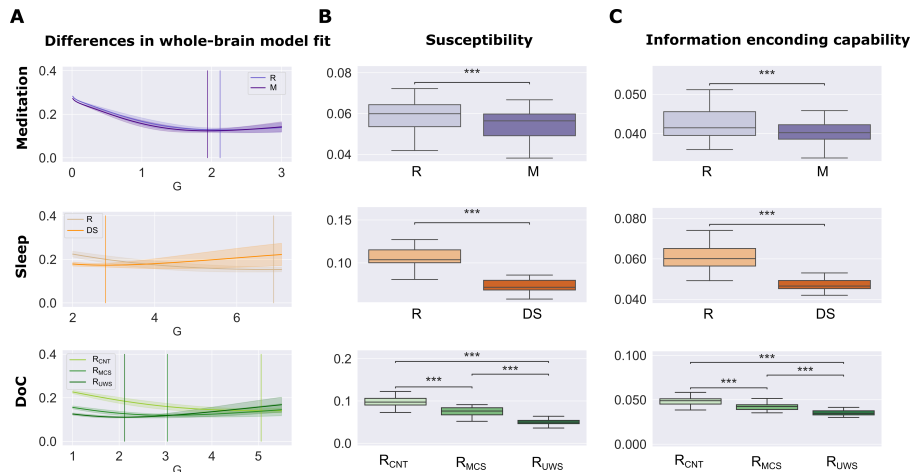
Figure 5.3: Information encoding capabilities of brain states. **A)** The optimal working point of the model was defined as the minimum value of the FC fitting, i.e., where the model shows maximal similarity to the empirical fMRI data. **B)** The susceptibility measure, which estimates how these models react to external artificial perturbations, showed that the resting state was most susceptible to being perturbed. **C)** The information encoding measure of the whole-brain models captures how different external stimulations are encoded in the dynamics. As in the susceptibility measure, the resting state was most susceptible to reacting to the perturbations. Both susceptibility and information encoding measures significantly differentiated between brain states. $\star\star\star$ represents $P < 0.001$.

and DoC (**Figure 5.3.BC**). Furthermore, both measures differentiated between MCS and UWS groups. These results are in line with previous studies showing that, compared to the resting state, the spatiotemporal dynamics in meditative states [Escrichs et al., 2019, Toutain et al., 2020], in DoC patients [Demertzi et al., 2019, López-González et al., 2021], and during deep sleep [Jobst et al., 2017, Deco et al., 2018, Ipiña et al., 2020] are reduced across the brain network.

Overall, we show that each brain state encodes the whole-brain dynamics with a particular complexity. Notably, the differential sensitivity of each brain state to external artificial perturbations can serve as a specific model-biomarker revealing features of their dynamical complexity.

5.4 Conclusion

Applying model-free and model-based approaches, the current thesis shows that whole-brain dynamics are fundamental for describing and characterising different brain states in health and disease. We demonstrate that different brain states show unique complex dynamics across spacetime scales. Furthermore, we show that causal whole-brain models can represent brain states in health and disease, including levels of consciousness, ageing, and neurological disorders. From a clinical standpoint, given the sensitivity and specificity of the results, in the long term, these methods may open new windows for developing efficient treatments for neurostimulation interventions by identifying potential targets to revert the effects of ageing or even to rebalance the level of consciousness in DoC patients.

Chapter 6

APPENDIX

6.1 Datasets

6.1.1 Meditation

The meditator group was recruited from Vipassana centres of Barcelona, Catalonia (7 females; mean age=39.8 years ($SD = 10.29$) and meditation experience=9,526.9 hours ($SD = 8,619.8$). Meditators maintained the daily practice (>1 hour/day) and had more than 1,000 hours of meditation experience. Healthy controls were well-matched participants for age, gender, and education years, with no previous experience in meditation (7 females; mean age= 39.75 years (SD=10.13); education=13.8 years). All participants reported no history of past neurological disorder and gave informed consent. The study was approved by the Ethics Committee of the Bellvitge University Hospital according to the Helsinki Declaration.

MRI images were acquired on a 3T Siemens Trio scanner using a 32-channel receiver coil. The T1-weighted images were acquired with 208 contiguous sagittal slices; TR/TE= 1970 ms/ 2.34 ms; inversion time (IT) = 1050 ms; flip angle = 9°; FOV = 256 mm; and isotropic voxel size 1 mm. Resting state and meditation fMRI images were performed by a single shot gradient-echo EPI sequence with a total of 450 volumes (15 min); TR/TE = 2000 ms/29 ms; FOV = 240 mm; in-plane resolution 3 mm; 32 transversal slices with thickness = 4 mm; flip angle = 80°. Diffusion

MRI images were acquired using a dual spin-echo DTI sequence (TR/TE= 680ms/92ms; FOV = 236mm; 60 contiguous axial slices; isotropic voxel size 2x2x2 mm; no gap, and 118 x118 matrix sizes). Diffusion was obtained with 64 optimal non-collinear diffusion directions using a single b value = 1,500s/mm2 interleaved with 9 non-diffusion b0 images.

6.1.2 Disorders of consciousness

Liège

Thirty-five healthy controls and 48 patients with disorders of consciousness (DoC) were included. The diagnosis was made after at least 5 CRS-R by trained clinicians. The highest level of consciousness was taken as the final diagnosis, which was also confirmed with Positron Emission Tomography (PET). Patients in MCS presented a relatively preserved metabolism in the frontoparietal network, whilst patients with UWS had a bilateral hypometabolism in this network. Thus, we included 33 patients in MCS and 15 in UWS. The Ethics Committee of the Faculty of Medicine of the University of Liege approved the study protocol. Written informed consent was obtained from patients' legal surrogates and healthy participants.

MRI images were acquired on a Siemens 3T Trio scanner (Siemens Inc, Munich, Germany). MRI acquisition included a gradient echo-planar imaging (EPI) sequence (32 transversal slices, 300 volumes, TR = 2000 ms, TE=30 ms, flip angle = 78°, voxel size = 3x3x3 mm, FOV = 192 mm); T1 (120 transversal slices, TR = 2300 ms, voxel size = 1.0x1.0x1.2 mm, flip angle = 9°, FOV = 256 mm).

Paris

Thirteen healthy controls, 27 patients in the MCS, and 21 in UWS were included in the final cohort. This research was approved by the local ethics committee Comité de Protection des Personnes Ile de France 1 (Paris, France) under the code 'Recherche en soins courants' (NEURODOC protocol, n° 2013-A01385-40). The patient's family gave informed consent for the participation of their relative, and all investigations were conducted according to the Declaration of Helsinki and the French regulations.

MRI data were acquired on a 3T General Electric Signa System (Milwaukee, WI). T2*-weighted resting state images were acquired with a gradient-echo EPI sequence using axial orientation (200 volumes, eight slices, slice thickness: 3 mm, TR=2400 ms, TE=30 ms, voxel size: 3.4375 × 3.4375 × 3.4375 mm, flip angle: 90°, FOV: 192 mm2). In the same acquisition session, an anatomical volume was acquired using a T1-weighted MPRAGE sequence (236 slices, TR=7156 ms, TE=3.672 ms, voxel size: 0.4883 × 0.4883 × 0.4883 mm, flip angle: 15°).

6.1.3 Sleep

Sixty-three healthy subjects (36 females, mean ± SD age of 23 ± 43.3 years) were selected from a dataset previously described in [Tagliazucchi and Laufs, 2014, Perl et al., 2021b]. Their resting state activity was measured during 52 minutes with a simultaneous combination of EEG and fMRI. We selected 13 subjects who reached the deep sleep stage (N3) and contiguous time series of at least 200 volumes. The experimental protocol was approved by the ethics committee (Goethe-Universität Frankfurt, Germany, protocol number: 305/07), and written informed consent was obtained for all participants before the study. The study was conducted according to the Helsinki Declaration on ethical research.

MRI images were acquired on a 3 T Siemens Trio scanner (Erlangen, Germany). EEG via a cap (modified BrainCapMR, Easycap, Herrsching, Germany) was recorded continuously during fMRI acquisition (1505 volumes of T2*-weighted echo-planar images, TR/TE = 2080 ms/30 ms, matrix 64×64, voxel size 3×3×2 mm^3, distance factor 50%; FOV 192 mm^2). An optimised polysomnographic setting was employed (chin and tibial EMG, ECG, EOG recorded bipolarly [sampling rate 5 kHz, low pass filter 1 kHz] with 30 EEG channels recorded with FCz as the reference [sampling rate 5 kHz, low pass filter 250 Hz]. Pulse oxymetry and respiration were recorded via sensors from the Trio [sampling rate 50 Hz]) and MR scanner compatible devices (BrainAmp MR+, BrainAmpExG; Brain Products, Gilching, Germany), facilitating sleep scoring during fMRI acquisition.

6.1.4 Ageing

Neuroimaging data were obtained from the Aging Imageomics Study [Puig et al., 2020] and comprised 620 healthy adults divided into two groups. The middle-aged group consisted of 310 subjects aged < 65 years (mean age, 60.2±3.7 years), and the older group consisted of 310 subjects aged >= 65 years (mean age, 71.8±4.5 years). The study was approved by the Ethics Committee of the Dr Josep Trueta University Hospital. Written informed consent was obtained from all participants. A complete description of the neuroimaging data can be consulted in [Puig et al., 2020, Escrichs et al., 2021, Escrichs et al., 2022b].

Images were acquired on a mobile 1.5 T scanner (Vantage Elan, Toshiba Medical Systems) with an 8-channel phased-array head coil. T1-weighted sequence (number of slices=112, TR/TE=8 ms/4.5 ms, flip angle=15º, FOV =235×235 mm and voxel size=1.3×1.3×2.5 mm) for structural imaging and a gradient echo-planar imaging (EPI) sequence (TR=2500 ms; TE=40 ms; flip angle=83°; FOV=230×230 mm; and voxel size=3.5×3.5×5 mm without gap) 122 volumes were acquired axially during five min for resting state fMRI. Subjects were asked to relax, stay motionless and remain awake.

6.2 Restin state preprocessing

Meditation, Paris, Liège

The pre-processing of resting state fMRI datasets of Meditation, Paris and Liège were performed using MELODIC (Multivariate Exploratory Linear Optimized Decomposition into Independent Components) [Beckmann and Smith, 2004], which is part of FSL (`http://fsl.fmrib.ox.ac.uk/fsl`). Steps included discarding the first five volumes, motion correction using MCFLIRT [Jenkinson et al., 2002], BET (Brain Extraction Tool) [Smith, 2002], spatial smoothing with 5 mm FWHM Gaussian Kernel, rigid-body registration, high pass filter cutoff = 100.0 s, and single-session ICA with automatic dimensionality estimation. Lesion-driven artefacts (for patients) and noise components were regressed out independently for each subject using FIX (FMRIB's ICA-based X-noiseifier) [Griffanti et al.,

2014]. FSL tools were used to co-register the images and extract the time series between 1000 cortical brain areas for each subject in MNI space from the Schaefer resting state parcellation [Schaefer et al., 2018].

Sleep

The preprocessing of resting state fMRI data was performed using FSL (`http://fsl.fmrib.ox.ac.uk/fsl`). Steps included discarding the first five volumes, motion correction using MCFLIRT [Jenkinson et al., 2002], BET (Brain Extraction Tool) [Smith, 2002], spatial smoothing with 5 mm FWHM Gaussian Kernel, rigid-body registration, bandpass filtering between $0.01 - 0.1\ Hz$. Finally, FSL tools were used to co-register the images and extract the time series between 1000 cortical brain areas for each subject in MNI space from the Schaefer resting state parcellation [Schaefer et al., 2018].

Ageing

T1 and EPI images were automatically oriented using Conn [Whitfield-Gabrieli and Nieto-Castanon, 2012]. Processing Assistant for Resting-State fMRI (DPARSF) [Chao-Gan and Yu-Feng, 2010], which is based on Statistical Parametric Mapping (SPM12), was used to preprocess the resting state fMRI data. Preprocessing steps included: discarding the first five volumes, slice-timing correction, realignment for head motion correction across volumes, T1 co-registration to the functional image, European regularisation segmentation, removal of spurious variance through linear regression: six parameters from the head motion correction, the white matter (WM) signal, and the cerebrospinal fluid signal (CSF) using CompCor [Behzadi et al., 2007], removal of the linear trend, spatial normalisation to MNI standard space, spatial smoothing with 6 mm FWHM Gaussian Kernel, and band-pass temporal filtering (0.01-0.020 Hz). The time series for each subject were extracted using a resting state atlas [Shen et al., 2013].

6.3 Difussion Tensor Imaging preprocessing

Meditation

The whole-brain structural connectivity matrix (SC) was computed following the procedure applied in previous studies [Gong et al., 2009, Cao et al., 2013, Muthuraman et al., 2016]. An SC was computed for each subject using the FMRIB's Diffusion Toolbox (FDT). Steps: Brain Extraction Tool (BET) [Smith, 2002], eddy current distortions and head motion were corrected using eddy correct [Andersson and Sotiropoulos, 2016], and the gradient matrix was reoriented to correct for subject motion [Leemans and Jones, 2009]. Crossing fibres were modelled using BEDPOSTX, and the probability of multi-fibre orientations was computed to improve the sensitivity of non-dominant fibre populations [Behrens et al., 2003, Behrens et al., 2007]. The probabilistic tractography analysis was performed for each participant in the native diffusion space using PROBTRACKX. The connectivity probability SC_{np} between brain areas n and p was calculated as the total proportion of sampled fibres in all voxels in brain area n that reach any voxel in brain area p. The SC_{np} matrix was then symmetrised by computing their transpose matrix SC_{pn} and averaging both matrices. Finally, averaging the resulting matrices across all participants, a whole-brain SC matrix was obtained, representing a template of healthy adults.

HCP

Diffusion spectrum and T2-weighted neuroimaging data for 32 participants were obtained from the Human Connectome Project (HCP) database, as described in Deco and Kringelbach [Deco and Kringelbach, 2020]. A complete description of the acquisition parameters for diffusion MRI (dMRI) is described in detail on the HCP website [Setsompop et al., 2013]. The freely Lead-DBS software package (`https://www.lead-dbs.org/`) provides the pre-processing described in detail in [Horn et al., 2017]. The data were processed using a q-sampling imaging algorithm implemented in DSI studio (`http://dsi-studio.labsolver.org`). A white-matter mask was calculated by segmenting the T2-weighted images and co-registering the

images to the b0 diffusion data by using SMP12. For each HCP partici-
pant, 200,000 fibres were sampled within the white-matter mask. Fibres
were transformed into MNI space using Lead-DBS [Horn and Blanken-
burg, 2016], and standardised methods in Lead-DBS were used to extract
the structural connectomes from the Schaefer 1000 parcellation [Schaefer
et al., 2018].

Bibliography

[Adhikari et al., 2017] Adhikari, M. H., Hacker, C. D., Siegel, J. S., Griffa, A., Hagmann, P., Deco, G., and Corbetta, M. (2017). Decreased integration and information capacity in stroke measured by whole brain models of resting state activity. *Brain*, 140(4):1068–1085.

[Allen et al., 2014] Allen, E. A., Damaraju, E., Plis, S. M., Erhardt, E. B., Eichele, T., and Calhoun, V. D. (2014). Tracking whole-brain connectivity dynamics in the resting state. *Cereb. Cortex*, 24(3):663–76.

[Andersson and Sotiropoulos, 2016] Andersson, J. L. and Sotiropoulos, S. N. (2016). An integrated approach to correction for off-resonance effects and subject movement in diffusion MR imaging. *Neuroimage*, 125:1063–1078.

[Baggio et al., 2015] Baggio, H. C., Segura, B., Junque, C., de Reus, M. A., Sala-Llonch, R., and Van den Heuvel, M. P. (2015). Rich Club Organization and Cognitive Performance in Healthy Older Participants. *J. Cogn. Neurosci.*, 27(9):1801–1810.

[Beckmann et al., 2005] Beckmann, C. F., DeLuca, M., Devlin, J. T., and Smith, S. M. (2005). Investigations into resting-state connectivity using independent component analysis. *Philos. Trans. R. Soc. Lond. B. Biol. Sci.*, 360(1457):1001–1013.

[Beckmann and Smith, 2004] Beckmann, C. F. and Smith, S. M. (2004). Probabilistic Independent Component Analysis for Functional Magnetic Resonance Imaging. *IEEE Trans. Med. Imaging*, 23(2):137–152.

[Behrens et al., 2003] Behrens, T., Woolrich, M., Jenkinson, M., Johansen-Berg, H., Nunes, R., Clare, S., Matthews, P., Brady, J., and Smith, S. (2003). Characterization and propagation of uncertainty in diffusion-weighted MR imaging. *Magn. Reson. Med.*, 50(5):1077–1088.

[Behrens et al., 2007] Behrens, T. E. J., Berg, H. J., Jbabdi, S., Rushworth, M. F. S., and Woolrich, M. W. (2007). Probabilistic diffusion tractography with multiple fibre orientations: What can we gain? *Neuroimage*, 34(1):144–155.

[Behzadi et al., 2007] Behzadi, Y., Restom, K., Liau, J., and Liu, T. T. (2007). A component based noise correction method (CompCor) for BOLD and perfusion based fMRI. *Neuroimage*, 37(1):90–101.

[Betzel et al., 2014] Betzel, R. F., Byrge, L., He, Y., Goñi, J., Zuo, X.-N. N., and Sporns, O. (2014). Changes in structural and functional connectivity among resting-state networks across the human lifespan. *Neuroimage*, 102(P2):345–357.

[Biswal et al., 1995] Biswal, B., Zerrin Yetkin, F., Haughton, V. M., and Hyde, J. S. (1995). Functional connectivity in the motor cortex of resting human brain using echo-planar mri. *Magn. Reson. Med.*, 34(4):537–541.

[Bodart et al., 2017] Bodart, O., Gosseries, O., Wannez, S., Thibaut, A., Annen, J., Boly, M., Rosanova, M., Casali, A. G., Casarotto, S., Tononi, G., Massimini, M., and Laureys, S. (2017). Measures of metabolism and complexity in the brain of patients with disorders of consciousness. *NeuroImage Clin.*, 14:354–362.

[Bolton et al., 2020] Bolton, T. A., Morgenroth, E., Preti, M. G., and Van De Ville, D. (2020). Tapping into Multi-Faceted Human Behavior and Psychopathology Using fMRI Brain Dynamics. *Trends Neurosci.*, 43(9):667–680.

[Cabeza et al., 2018] Cabeza, R., Albert, M., Belleville, S., Craik, F. I., Duarte, A., Grady, C. L., Lindenberger, U., Nyberg, L., Park, D. C., Reuter-Lorenz, P. A., Rugg, M. D., Steffener, J., and Rajah, M. N.

(2018). Maintenance, reserve and compensation: the cognitive neuroscience of healthy ageing.

[Cabral et al., 2017] Cabral, J., Vidaurre, D., Marques, P., Magalhães, R., Silva Moreira, P., Miguel Soares, J., Deco, G., Sousa, N., and Kringelbach, M. L. (2017). Cognitive performance in healthy older adults relates to spontaneous switching between states of functional connectivity during rest. *Sci. Rep.*, 7(1):5135.

[Calhoun et al., 2014] Calhoun, V. D., Miller, R., Pearlson, G., and Adalı, T. (2014). The Chronnectome: Time-Varying Connectivity Networks as the Next Frontier in fMRI Data Discovery. *Neuron*, 84(2):262–274.

[Cao et al., 2014] Cao, M., Wang, J.-H. H., Dai, Z.-J. J., Cao, X.-Y. Y., Jiang, L.-L. L., Fan, F.-M. M., Song, X.-W. W., Xia, M.-R. R., Shu, N., Dong, Q., Milham, M. P., Castellanos, F. X., Zuo, X.-N. N., and He, Y. (2014). Topological organization of the human brain functional connectome across the lifespan. *Dev. Cogn. Neurosci.*, 7:76–93.

[Cao et al., 2013] Cao, Q., Shu, N., An, L., Wang, P., Sun, L., Xia, M.-R., Wang, J.-H., Gong, G.-L., Zang, Y.-F., Wang, Y.-F., and He, Y. (2013). Probabilistic diffusion tractography and graph theory analysis reveal abnormal white matter structural connectivity networks in drug-naive boys with attention deficit/hyperactivity disorder. *J. Neurosci.*, 33(26):10676–87.

[Carhart-Harris et al., 2016] Carhart-Harris, R. L., Muthukumaraswamy, S., Roseman, L., Kaelen, M., Droog, W., Murphy, K., Tagliazucchi, E., Schenberg, E. E., Nest, T., Orban, C., Leech, R., Williams, L. T., Williams, T. M., Bolstridge, M., Sessa, B., McGonigle, J., Sereno, M. I., Nichols, D., Hellyer, P. J., Hobden, P., Evans, J., Singh, K. D., Wise, R. G., Curran, H. V., Feilding, A., and Nutt, D. J. (2016). Neural correlates of the LSD experience revealed by multimodal neuroimaging. *Proc. Natl. Acad. Sci.*, 113(17):4853–4858.

[Casali et al., 2013] Casali, A. G., Gosseries, O., Rosanova, M., Boly, M., Sarasso, S., Casali, K. R., Casarotto, S., Bruno, M. A., Laureys, S., Tononi, G., and Massimini, M. (2013). A theoretically based index

of consciousness independent of sensory processing and behavior. *Sci. Transl. Med.*, 5(198):198ra105–198ra105.

[Casarotto et al., 2016] Casarotto, S., Comanducci, A., Rosanova, M., Sarasso, S., Fecchio, M., Napolitani, M., Pigorini, A., G. Casali, A., Trimarchi, P. D., Boly, M., Gosseries, O., Bodart, O., Curto, F., Landi, C., Mariotti, M., Devalle, G., Laureys, S., Tononi, G., and Massimini, M. (2016). Stratification of unresponsive patients by an independently validated index of brain complexity. *Ann. Neurol.*, 80(5):718–729.

[Chao-Gan and Yu-Feng, 2010] Chao-Gan, Y. and Yu-Feng, Z. (2010). DPARSF: A MATLAB Toolbox for "Pipeline" Data Analysis of Resting-State fMRI. *Front. Syst. Neurosci.*, 4:13.

[Clare Kelly et al., 2008] Clare Kelly, A. M., Uddin, L. Q., Biswal, B. B., Castellanos, F. X., and Milham, M. P. (2008). Competition between functional brain networks mediates behavioral variability. *Neuroimage*, 39(1):527–537.

[Clausen, 2010] Clausen, J. (2010). Ethical brain stimulation – neuroethics of deep brain stimulation in research and clinical practice. *Eur. J. Neurosci.*, 32(7):1152–1162.

[Cruzat et al., 2022] Cruzat, J., Perl, Y. S., Escrichs, A., Vohryzek, J., Timmermann, C., Roseman, L., Luppi, A. I., Ibañez, A., Nutt, D., Carhart-Harris, R., Tagliazucchi, E., Deco, G., and Kringelbach, M. L. (2022). Effects of classic psychedelic drugs on turbulent signatures in brain dynamics. *Netw. Neurosci.*, pages 1–42.

[Damoiseaux, 2017] Damoiseaux, J. S. (2017). Effects of aging on functional and structural brain connectivity. *Neuroimage*, 160:32–40.

[Damoiseaux et al., 2006] Damoiseaux, J. S., Rombouts, S. A., Barkhof, F., Scheltens, P., Stam, C. J., Smith, S. M., and Beckmann, C. F. (2006). Consistent resting-state networks across healthy subjects. *Proc. Natl. Acad. Sci.*, 103(37):13848–13853.

[Davis et al., 2008] Davis, S. W., Dennis, N. A., Daselaar, S. M., Fleck, M. S., and Cabeza, R. (2008). Que PASA? The posterior-anterior shift in aging. *Cereb. Cortex*, 18(5):1201–9.

[De Filippi et al., 2022] De Filippi, E., Escrichs, A., Càmara, E., Garrido, C., Marins, T., Marti Sánchez-Fibla, ·., Gilson, ·. M., and Deco, G. (2022). Meditation-induced effects on whole-brain structural and effective connectivity. *Brain Struct. Funct. 2022*, 1:1–16.

[Deco et al., 2018] Deco, G., Cabral, J., Saenger, V. M., Boly, M., Tagliazucchi, E., Laufs, H., Van Someren, E., Jobst, B., Stevner, A., and Kringelbach, M. L. (2018). Perturbation of whole-brain dynamics in silico reveals mechanistic differences between brain states. *Neuroimage*, 169:46–56.

[Deco et al., 2019] Deco, G., Cruzat, J., Cabral, J., Tagliazucchi, E., Laufs, H., Logothetis, N. K., and Kringelbach, M. L. (2019). Awakening: Predicting external stimulation to force transitions between different brain states. *Proc. Natl. Acad. Sci.*, 116(36):18088–18097.

[Deco and Jirsa, 2012] Deco, G. and Jirsa, V. K. (2012). Ongoing Cortical Activity at Rest: Criticality, Multistability, and Ghost Attractors. *J. Neurosci.*, 32(10):3366–3375.

[Deco et al., 2011] Deco, G., Jirsa, V. K., and McIntosh, A. R. (2011). Emerging concepts for the dynamical organization of resting-state activity in the brain. *Nat. Rev. Neurosci.*, 12(1):43–56.

[Deco et al., 2013] Deco, G., Jirsa, V. K., and McIntosh, A. R. (2013). Resting brains never rest: Computational insights into potential cognitive architectures.

[Deco et al., 2021a] Deco, G., Kemp, M., and Kringelbach, M. L. (2021a). Leonardo da Vinci and the search for order in neuroscience. *Curr. Biol.*, 31(11):R704–R709.

[Deco and Kringelbach, 2016] Deco, G. and Kringelbach, M. L. (2016). Metastability and Coherence: Extending the Communication through Coherence Hypothesis Using A Whole-Brain Computational Perspective. *Trends Neurosci.*, 39(3):125–135.

[Deco and Kringelbach, 2017] Deco, G. and Kringelbach, M. L. (2017). Hierarchy of Information Processing in the Brain: A Novel 'Intrinsic Ignition' Framework. *Neuron*, 94(5):961–968.

[Deco and Kringelbach, 2020] Deco, G. and Kringelbach, M. L. (2020). Turbulent-like Dynamics in the Human Brain. *Cell Rep.*, 33(10):108471.

[Deco et al., 2017a] Deco, G., Kringelbach, M. L., Jirsa, V. K., and Ritter, P. (2017a). The dynamics of resting fluctuations in the brain: metastability and its dynamical cortical core. *Sci. Rep.*, 7(1):3095.

[Deco et al., 2021b] Deco, G., Perl, Y. S., Vuust, P., Tagliazucchi, E., Kennedy, H., and Kringelbach, M. L. (2021b). Rare long-range cortical connections enhance human information processing. *Curr. Biol.*

[Deco et al., 2017b] Deco, G., Tagliazucchi, E., Laufs, H., Sanjuán, A., and Kringelbach, M. L. (2017b). Novel Intrinsic Ignition Method Measuring Local- Global Integration Characterizes Wakefulness and Deep Sleep. *eneuro*, 4(5):ENEURO.0106–17.2017.

[Deco et al., 2015] Deco, G., Tononi, G., Boly, M., and Kringelbach, M. L. (2015). Rethinking segregation and integration: contributions of whole-brain modelling. *Nat. Rev. Neurosci.*, 16(7):430–439.

[Dehaene and Changeux, 2011] Dehaene, S. and Changeux, J. P. (2011). Experimental and Theoretical Approaches to Conscious Processing. *Neuron*, 70(2):200–227.

[Demertzi et al., 2019] Demertzi, A., Tagliazucchi, E., Dehaene, S., Deco, G., Barttfeld, P., Raimondo, F., Martial, C., Fernández-Espejo, D., Rohaut, B., Voss, H. U., Schiff, N. D., Owen, A. M., Laureys, S., Naccache, L., and Sitt, J. D. (2019). Human consciousness is supported by dynamic complex patterns of brain signal coordination. *Sci. Adv.*, 5(2):eaat7603.

[Demirtaş et al., 2017] Demirtaş, M., Falcon, C., Tucholka, A., Gispert, J. D., Molinuevo, J. L., and Deco, G. (2017). A whole-brain computational modeling approach to explain the alterations in resting-state functional connectivity during progression of Alzheimer's disease. *NeuroImage Clin.*

[Drysdale et al., 2016] Drysdale, A. T., Grosenick, L., Downar, J., Dunlop, K., Mansouri, F., Meng, Y., Fetcho, R. N., Zebley, B., Oathes,

D. J., Etkin, A., Schatzberg, A. F., Sudheimer, K., Keller, J., Mayberg, H. S., Gunning, F. M., Alexopoulos, G. S., Fox, M. D., Pascual-Leone, A., Voss, H. U., Casey, B., Dubin, M. J., and Liston, C. (2016). Resting-state connectivity biomarkers define neurophysiological subtypes of depression. *Nat. Med.*, 23(1):28–38.

[Escrichs et al., 2021] Escrichs, A., Biarnes, C., Garre-Olmo, J., Fernández-Real, J. M., Ramos, R., Pamplona, R., Brugada, R., Serena, J., Ramió-Torrentà, L., Coll-De-Tuero, G., Gallart, L., Barretina, J., Vilanova, J. C., Mayneris-Perxachs, J., Essig, M., Figley, C. R., Pedraza, S., Puig, J., and Deco, G. (2021). Whole-Brain Dynamics in Aging: Disruptions in Functional Connectivity and the Role of the Rich Club. *Cereb. Cortex*, 31(5):2466–2481.

[Escrichs et al., 2022a] Escrichs, A., Perl, Y. S., Uribe, C., Camara, E., Türker, B., Pyatigorskaya, N., López-González, A., Pallavicini, C., Panda, R., Annen, J., Gosseries, O., Laureys, S., Naccache, L., Sitt, J. D., Laufs, H., Tagliazucchi, E., Kringelbach, M. L., and Deco, G. (2022a). Unifying turbulent dynamics framework distinguishes different brain states. *Commun. Biol.*, 5(1):1–13.

[Escrichs et al., 2019] Escrichs, A., Sanjuán, A., Atasoy, S., López-González, A., Garrido, C., Càmara, E., and Deco, G. (2019). Characterizing the Dynamical Complexity Underlying Meditation. *Front. Syst. Neurosci.*, 13:27.

[Escrichs et al., 2022b] Escrichs, A., Sanz Perl, Y., Martínez-Molina, N., Biarnes, C., Garre-Olmo, J., Fernández-Real, J. M., Ramos, R., Martí, R., Pamplona, R., Brugada, R., Serena, J., Ramió-Torrentà, L., Coll-De-Tuero, G., Gallart, L., Barretina, J., Vilanova, J. C., Mayneris-Perxachs, J., Saba, L., Pedraza, S., Kringelbach, M. L., Puig, J., and Deco, G. (2022b). The effect of external stimulation on functional networks in the aging healthy human brain. *Cereb. Cortex*.

[Fernández-Espejo and Owen, 2013] Fernández-Espejo, D. and Owen, A. M. (2013). Detecting awareness after severe brain injury. *Nat. Rev. Neurosci.*, 14(11):801–809.

99

[Ferrarelli et al., 2010] Ferrarelli, F., Massimini, M., Sarasso, S., Casali, A., Riedner, B. A., Angelini, G., Tononi, G., and Pearce, R. A. (2010). Breakdown in cortical effective connectivity during midazolam-induced loss of consciousness. *Proc. Natl. Acad. Sci.*, 107(6):2681–2686.

[Fox and Greicius, 2010] Fox, M. D. and Greicius, M. (2010). Clinical applications of resting state functional connectivity. *Front. Syst. Neurosci.*, 4(June):19.

[Fox and Raichle, 2007] Fox, M. D. and Raichle, M. E. (2007). Spontaneous fluctuations in brain activity observed with functional magnetic resonance imaging. *Nat. Rev. Neurosci.*, 8(9):700–711.

[Fox et al., 2005] Fox, M. D., Snyder, A. Z., Vincent, J. L., Corbetta, M., Van Essen, D. C., and Raichle, M. E. (2005). The human brain is intrinsically organized into dynamic, anticorrelated functional networks. *Proc. Natl. Acad. Sci. U. S. A.*, 102(27):9673–9678.

[Frisch, 1995] Frisch, U. (1995). *Turbulence: The Legacy of A. N. Kolmogorov.* Cambridge University Press.

[García-Morales and Krischer, 2012] García-Morales, V. and Krischer, K. (2012). The complex Ginzburg–Landau equation: an introduction. *http://dx.doi.org/10.1080/00107514.2011.642554*, 53(2):79–95.

[Geerligs et al., 2015] Geerligs, L., Renken, R. J., Saliasi, E., Maurits, N. M., and Lorist, M. M. (2015). A Brain-Wide Study of Age-Related Changes in Functional Connectivity. *Cereb. Cortex*, 25(7):1987–1999.

[Ghosh et al., 2008] Ghosh, A., Rho, Y., McIntosh, A. R., Kötter, R., and Jirsa, V. K. (2008). Cortical network dynamics with time delays reveals functional connectivity in the resting brain. *Cogn. Neurodyn.*, 2(2):115.

[Glerean et al., 2012] Glerean, E., Salmi, J., Lahnakoski, J. M., Jääskeläinen, I. P., and Sams, M. (2012). Functional magnetic resonance imaging phase synchronization as a measure of dynamic functional connectivity. *Brain Connect.*, 2(2):91–101.

[Goldman et al., 2019] Goldman, J. S., Tort-Colet, N., di Volo, M., Susin, E., Bouté, J., Dali, M., Carlu, M., Nghiem, T.-A., Górski, T., and

Destexhe, A. (2019). Bridging Single Neuron Dynamics to Global Brain States. *Front. Syst. Neurosci.*, 0:75.

[Gong et al., 2009] Gong, G., Rosa-Neto, P., Carbonell, F., Chen, Z. J., He, Y., and Evans, A. C. (2009). Age- and gender-related differences in the cortical anatomical network. *J. Neurosci.*, 29(50):15684–93.

[Greicius et al., 2003] Greicius, M. D., Krasnow, B., Reiss, A. L., and Menon, V. (2003). Functional connectivity in the resting brain: a network analysis of the default mode hypothesis. *Proc. Natl. Acad. Sci. U. S. A.*, 100(1):253–8.

[Greicius et al., 2009] Greicius, M. D., Supekar, K., Menon, V., and Dougherty, R. F. (2009). Resting-state functional connectivity reflects structural connectivity in the default mode network. *Cereb. Cortex*, 19(1):72–78.

[Griffanti et al., 2014] Griffanti, L., Salimi-Khorshidi, G., Beckmann, C. F., Auerbach, E. J., Douaud, G., Sexton, C. E., Zsoldos, E., Ebmeier, K. P., Filippini, N., Mackay, C. E., Moeller, S., Xu, J., Yacoub, E., Baselli, G., Ugurbil, K., Miller, K. L., and Smith, S. M. (2014). ICA-based artefact removal and accelerated fMRI acquisition for improved resting state network imaging. *Neuroimage*, 95:232–247.

[Hagmann et al., 2008] Hagmann, P., Cammoun, L., Gigandet, X., Meuli, R., Honey, C. J., Van Wedeen, J., and Sporns, O. (2008). Mapping the Structural Core of Human Cerebral Cortex. *PLoS Biol.*, 6(7):1479–1493.

[Honey et al., 2009] Honey, C. J., Sporns, O., Cammoun, L., Gigandet, X., Thiran, J. P., Meuli, R., and Hagmann, P. (2009). Predicting human resting-state functional connectivity from structural connectivity. *Proc. Natl. Acad. Sci. U. S. A.*, 106(6):2035–40.

[Horn and Blankenburg, 2016] Horn, A. and Blankenburg, F. (2016). Toward a standardized structural-functional group connectome in MNI space. *Neuroimage*, 124(Pt A):310–322.

[Horn et al., 2017] Horn, A., Neumann, W. J., Degen, K., Schneider, G. H., and Kühn, A. A. (2017). Toward an electrophysiological "Sweet

spot" for deep brain stimulation in the subthalamic nucleus. *Hum. Brain Mapp.*, 38(7):3377–3390.

[Hutchison et al., 2013] Hutchison, R. M., Womelsdorf, T., Allen, E. A., Bandettini, P. A., Calhoun, V. D., Corbetta, M., Della Penna, S., Duyn, J. H., Glover, G. H., Gonzalez-Castillo, J., Handwerker, D. A., Keilholz, S., Kiviniemi, V., Leopold, D. A., de Pasquale, F., Sporns, O., Walter, M., and Chang, C. (2013). Dynamic functional connectivity: Promise, issues, and interpretations. *Neuroimage*, 80:360–378.

[Ipiña et al., 2020] Ipiña, I. P., Kehoe, P. D., Kringelbach, M., Laufs, H., Ibañez, A., Deco, G., Perl, Y. S., and Tagliazucchi, E. (2020). Modeling regional changes in dynamic stability during sleep and wakefulness. *Neuroimage*, 215:116833.

[Irrmischer et al., 2018] Irrmischer, M., Houtman, S. J., Mansvelder, H. D., Tremmel, M., Ott, U., and Linkenkaer-Hansen, K. (2018). Controlling the Temporal Structure of Brain Oscillations by Focused Attention Meditation. *Hum. Brain Mapp.*

[Jenkinson et al., 2002] Jenkinson, M., Bannister, P., Brady, M., and Smith, S. (2002). Improved Optimization for the Robust and Accurate Linear Registration and Motion Correction of Brain Images. *Neuroimage*, 17(2):825–841.

[Jobst et al., 2017] Jobst, B. M., Hindriks, R., Laufs, H., Tagliazucchi, E., Hahn, G., Ponce-Alvarez, A., Stevner, A. B. A., Kringelbach, M. L., and Deco, G. (2017). Increased Stability and Breakdown of Brain Effective Connectivity During Slow-Wave Sleep: Mechanistic Insights from Whole-Brain Computational Modelling. *Sci. Rep.*, 7(1):4634.

[King et al., 2013] King, J. R., Sitt, J. D., Faugeras, F., Rohaut, B., El Karoui, I., Cohen, L., Naccache, L., and Dehaene, S. (2013). Information Sharing in the Brain Indexes Consciousness in Noncommunicative Patients. *Curr. Biol.*, 23(19):1914–1919.

[Koch et al., 2002] Koch, M. A., Norris, D. G., and Hund-Georgiadis, M. (2002). An investigation of functional and anatomical connectivity using magnetic resonance imaging. *Neuroimage*, 16(1):241–250.

[Kolmogorov, 1941a] Kolmogorov, N. A. (1941a). Dissipation of energy in the locally isotropic turbulence. *C. R. Acad. Sci. URSS*, 32:16–18.

[Kolmogorov, 1941b] Kolmogorov, N. A. (1941b). The local structure of turbulence in incompressible viscous fluid for very large Reynolds numbers. *C. R. Acad. Sci. URSS*, 30:301–305.

[Kringelbach and Deco, 2020] Kringelbach, M. L. and Deco, G. (2020). Brain States and Transitions: Insights from Computational Neuroscience. *Cell Rep.*, 32(10):108128.

[Kringelbach et al., 2007] Kringelbach, M. L., Jenkinson, N., Owen, S. L., and Aziz, T. Z. (2007). Translational principles of deep brain stimulation. *Nat. Rev. Neurosci. 2007 88*, 8(8):623–635.

[Kuramoto, 1984] Kuramoto, Y. (1984). Chemical turbulence. In *Chemical Oscillations, Waves, and Turbulence*, pages 111–140. Springer.

[Laureys et al., 2004] Laureys, S., Owen, A. M., and Schiff, N. D. (2004). Brain function in coma, vegetative state, and related disorders. *Lancet Neurol.*, 3(9):537–546.

[Le Bihan, 2003] Le Bihan, D. (2003). Looking into the functional architecture of the brain with diffusion MRI. *Nat. Rev. Neurosci.*, 4(6):469–480.

[Leemans and Jones, 2009] Leemans, A. and Jones, D. K. (2009). The B -matrix must be rotated when correcting for subject motion in DTI data. *Magn. Reson. Med.*, 61(6):1336–1349.

[Li et al., 2015] Li, H. J., Hou, X. H., Liu, H. H., Yue, C. L., Lu, G. M., and Zuo, X. N. (2015). Putting age-related task activation into large-scale brain networks: A meta-analysis of 114 fMRI studies on healthy aging. *Neurosci. Biobehav. Rev.*, 57:156–174.

[Lim et al., 2018] Lim, J., Teng, J., Patanaik, A., Tandi, J., and Massar, S. A. (2018). Dynamic functional connectivity markers of objective trait mindfulness. *Neuroimage*, 176:193–202.

[López-González et al., 2021] López-González, A., Panda, R., Ponce-Alvarez, A., Zamora-López, G., Escrichs, A., Martial, C., Thibaut, A., Gosseries, O., Kringelbach, M. L., Annen, J., Laureys, S., and Deco, G. (2021). Loss of consciousness reduces the stability of brain hubs and the heterogeneity of brain dynamics. *Commun. Biol.*, 4(1):1–15.

[Lou et al., 2019] Lou, W., Wang, D., Wong, A., Chu, W. C., Mok, V. C., and Shi, L. (2019). Frequency-specific age-related decreased brain network diversity in cognitively healthy elderly: A whole-brain data-driven analysis. *Hum. Brain Mapp.*, 40(1):340–351.

[Lowe et al., 1998] Lowe, M. J., Mock, B. J., and Sorenson, J. A. (1998). Functional connectivity in single and multislice echoplanar imaging using resting-state fluctuations. *Neuroimage*, 7(2):119–132.

[Lurie et al., 2020] Lurie, D., Kessler, D., Bassett, D., Betzel, R. F., Breakspear, P. M., Keilholz, S., Kucyi, A., Liégeois, R., Lindquist, M. A., McIntosh, A. R., Poldrack, R., Shine, J., Thompson, W. H., Bielczyk, N., Douw, L., Kraft, D., Miller, R., Muthuraman, M., Pasquini, L., Razi, A., Vidaurre, D., Xie, H., and Calhoun, V. D. (2020). Questions and controversies in the study of time-varying functional connectivity in resting fMRI. *Netw. Neurosci.*, 4(1):30–69.

[Marusak et al., 2018] Marusak, H. A., Elrahal, F., Peters, C. A., Kundu, P., Lombardo, M. V., Calhoun, V. D., Goldberg, E. K., Cohen, C., Taub, J. W., and Rabinak, C. A. (2018). Mindfulness and dynamic functional neural connectivity in children and adolescents. *Behav. Brain Res.*, 336:211–218.

[Massimini et al., 2005] Massimini, M., Ferrarelli, F., Huber, R., Esser, S. K., Singh, H., and Tononi, G. (2005). Breakdown of cortical effective connectivity during sleep. *Science*, 309(5744):2228–2232.

[Mayneris-Perxachs et al., 2022] Mayneris-Perxachs, J., Castells-Nobau, A., Arnoriaga-Rodríguez, M., Martin, M., de la Vega-Correa, L., Zapata, C., Burokas, A., Blasco, G., Coll, C., Escrichs, A., Biarnés, C., Moreno-Navarrete, J. M., Puig, J., Garre-Olmo, J., Ramos, R., Pedraza, S., Brugada, R., Vilanova, J. C., Serena, J., Gich, J., Ramió-Torrentà, L., Pérez-Brocal, V., Moya, A., Pamplona, R., Sol, J., Jové, M., Ricart,

W., Portero-Otin, M., Deco, G., Maldonado, R., and Fernández-Real, J. M. (2022). Microbiota alterations in proline metabolism impact depression. *Cell Metab.*, 34(5):681–701.e10.

[Morcom and Henson, 2018] Morcom, A. M. and Henson, R. N. (2018). Increased prefrontal activity with aging reflects nonspecific neural responses rather than compensation. *J. Neurosci.*, 38(33):7303–7313.

[Muthuraman et al., 2016] Muthuraman, M., Fleischer, V., Kolber, P., Luessi, F., Zipp, F., and Groppa, S. (2016). Structural Brain Network Characteristics Can Differentiate CIS from Early RRMS. *Front. Neurosci.*, 10:14.

[Naik et al., 2017] Naik, S., Banerjee, A., Bapi, R. S., Deco, G., and Roy, D. (2017). Metastability in Senescence. *Trends Cogn. Sci.*, 21:509–521.

[Owen et al., 2006] Owen, A. M., Coleman, M. R., Boly, M., Davis, M. H., Laureys, S., and Pickard, J. D. (2006). Detecting Awareness in the Vegetative State. *Science (80-.).*, 313(5792):1402–1402.

[Panda et al., 2021a] Panda, R., Lopez-Gonzalez, A., Gilson, M., Gosseries, O., Thibaut, A., Frasso, G., Cecconi, B., Escrichs, A., group Collaborators, G., Deco, G., Laureys, S., Zamora-Lopez, G., and Annen, J. (2021a). Posterior integration and thalamo-frontotemporal broadcasting are impaired in disorders of consciousness. *bioRxiv*, page 2021.11.08.467694.

[Panda et al., 2021b] Panda, R., Thibaut, A., Lopez-Gonzalez, A., Escrichs, A., Bahri, M. A., Hillebrand, A., Deco, G., Laureys, S., Gosseries, O., Annen, J., and Tewarie, P. (2021b). Disruption in structural-functional network repertoire and time resolved subcortical-frontoparietal connectivity in disorders of consciousness. *bioRxiv*, page 2021.12.10.472068.

[Perl et al., 2021a] Perl, Y. S., Escrichs, A., Tagliazucchi, E., Kringelbach, M. L., and Deco, G. (2021a). On the edge of criticality: strength-dependent perturbation unveils delicate balance between fluctuation and oscillation in brain dynamics. *bioRxiv*, page 2021.09.23.461520.

105

[Perl et al., 2021b] Perl, Y. S., Pallavicini, C., Ipiña, I. P., Demertzi, A., Bonhomme, V., Martial, C., Panda, R., Annen, J., Ibañez, A., Kringelbach, M., Deco, G., Laufs, H., Sitt, J., Laureys, S., and Tagliazucchi, E. (2021b). Perturbations in dynamical models of whole-brain activity dissociate between the level and stability of consciousness. *PLoS Comput. Biol.*, 17(7):26.

[Ponce-Alvarez et al., 2015] Ponce-Alvarez, A., Deco, G., Hagmann, P., Romani, G. L., Mantini, D., and Corbetta, M. (2015). Resting-State Temporal Synchronization Networks Emerge from Connectivity Topology and Heterogeneity. *PLOS Comput. Biol.*, 11(2):e1004100.

[Popovych et al., 2019] Popovych, O. V., Manos, T., Hoffstaedter, F., and Eickhoff, S. B. (2019). What can computational models contribute to neuroimaging data analytics? *Front. Syst. Neurosci.*, 12:68.

[Puig et al., 2020] Puig, J., Biarnes, C., Pedraza, S., Vilanova, J. C., Pamplona, R., Fernández-Real, J. M., Brugada, R., Ramos, R., Coll-de Tuero, G., Calvo-Perxas, L., Serena, J., Ramió-Torrentà, L., Gich, J., Gallart, L., Portero-Otin, M., Alberich-Bayarri, A., Jimenez-Pastor, A., Camacho-Ramos, E., Mayneris-Perxachs, J., Pineda, V., Font, R., Prats-Puig, A., Gacto, M.-L., Deco, G., Escrichs, A., Clotet, B., Paredes, R., Negredo, E., Triaire, B., Rodríguez, M., Heredia-Escámez, A., Coronado, R., de Graaf, W., Prevost, V., Mitulescu, A., Daunis-i Estadella, P., Thió-Henestrosa, S., Miralles, F., Ribas-Ripoll, V., Puig-Domingo, M., Essig, M., Figley, C. R., Figley, T. D., Albensi, B., Ashraf, A., Reiber, J. H., Schifitto, G., Md Nasir, U., Leiva-Salinas, C., Wintermark, M., Nael, K., Vilalta-Franch, J., Barretina, J., and Garre-Olmo, J. (2020). The aging imageomics study: rationale, design and baseline characteristics of the study population. *Mech. Ageing Dev.*, page 111257.

[Puig et al., 2018] Puig, J., Blasco, G., Alberich-Bayarri, A., Schlaug, G., Deco, G., Biarnes, C., Navas-Martí, M., Rivero, M., Gich, J., Figueras, J., Torres, C., Daunis-i Estadella, P., Oramas-Requejo, C. L., Serena, J., Stinear, C. M., Kuceyeski, A., Soriano-Mas, C., Thomalla, G., Essig, M., Figley, C. R., Menon, B., Demchuk, A., Nael, K., Wintermark, M., Liebeskind, D. S., and Pedraza, S. (2018). Resting-State Functional

Connectivity Magnetic Resonance Imaging and Outcome After Acute Stroke. *Stroke*, 49(10):2353–2360.

[Raichle et al., 2001] Raichle, M. E., MacLeod, A. M., Snyder, A. Z., Powers, W. J., Gusnard, D. A., and Shulman, G. L. (2001). A default mode of brain function. *Proc. Natl. Acad. Sci. U. S. A.*, 98(2):676–682.

[Reuter-Lorenz and Cappell, 2008] Reuter-Lorenz, P. A. and Cappell, K. A. (2008). Neurocognitive Aging and the Compensation Hypothesis. *Curr. Dir. Psychol. Sci.*, 17(3):177–182.

[Rogers et al., 2007] Rogers, B. P., Morgan, V. L., Newton, A. T., and Gore, J. C. (2007). Assessing functional connectivity in the human brain by fMRI. *Magn. Reson. Imaging*, 25(10):1347–1357.

[Rosazza and Minati, 2011] Rosazza, C. and Minati, L. (2011). Resting-state brain networks: literature review and clinical applications. *Neurol. Sci.*, 32(5):773–785.

[Saenger et al., 2017] Saenger, V. M., Kahan, J., Foltynie, T., Friston, K., Aziz, T. Z., Green, A. L., Van Hartevelt, T. J., Cabral, J., Stevner, A. B., Fernandes, H. M., Mancini, L., Thornton, J., Yousry, T., Limousin, P., Zrinzo, L., Hariz, M., Marques, P., Sousa, N., Kringelbach, M. L., and Deco, G. (2017). Uncovering the underlying mechanisms and whole-brain dynamics of deep brain stimulation for Parkinson's disease. *Sci. Reports 2017 71*, 7(1):1–14.

[Schaefer et al., 2018] Schaefer, A., Kong, R., Gordon, E. M., Laumann, T. O., Zuo, X.-N., Holmes, A. J., Eickhoff, S. B., and Yeo, B. T. T. (2018). Local-Global Parcellation of the Human Cerebral Cortex from Intrinsic Functional Connectivity MRI. *Cereb. Cortex*, 28:3095–3114.

[Setsompop et al., 2013] Setsompop, K., Kimmlingen, R., Eberlein, E., Witzel, T., Cohen-Adad, J., McNab, J. A., Keil, B., Tisdall, M. D., Hoecht, P., Dietz, P., Cauley, S. F., Tountcheva, V., Matschl, V., Lenz, V. H., Heberlein, K., Potthast, A., Thein, H., Van Horn, J., Toga, A., Schmitt, F., Lehne, D., Rosen, B. R., Wedeen, V., and Wald, L. L. (2013). Pushing the limits of in vivo diffusion MRI for the Human Connectome Project. *Neuroimage*, 80:220–233.

[Shen et al., 2013] Shen, X., Tokoglu, F., Papademetris, X., and Constable, R. T. (2013). Groupwise whole-brain parcellation from resting-state fMRI data for network node identification. *Neuroimage*, 82:403–415.

[Sherman et al., 2014] Sherman, L. E., Rudie, J. D., Pfeifer, J. H., Masten, C. L., McNealy, K., and Dapretto, M. (2014). Development of the Default Mode and Central Executive Networks across early adolescence: A longitudinal study. *Dev. Cogn. Neurosci.*, 10:148–159.

[Smith, 2002] Smith, S. M. (2002). Fast robust automated brain extraction. *Hum. Brain Mapp.*, 17(3):143–155.

[Smith et al., 2009] Smith, S. M., Fox, P. T., Miller, K. L., Glahn, D. C., Fox, P. M., Mackay, C. E., Filippini, N., Watkins, K. E., Toro, R., Laird, A. R., and Beckmann, C. F. (2009). Correspondence of the brain's functional architecture during activation and rest. *Proc. Natl. Acad. Sci.*, 106(31):13040–13045.

[Soler-Toscano et al., 2022] Soler-Toscano, F., Galadí, J. A., Escrichs, A., Perl, Y. S., López-González, A., Sitt, J. D., Annen, J., Gosseries, O., Thibaut, A., Panda, R., Esteban, F. J., Laureys, S., Kringelbach, M. L., Langa, J. A., and Deco, G. (2022). What lies underneath: Precise classification of brain states using time-dependent topological structure of dynamics. *PLOS Comput. Biol.*, 18(9):e1010412.

[Sporns, 2013] Sporns, O. (2013). Network attributes for segregation and integration in the human brain. *Curr. Opin. Neurobiol.*, 23(2):162–171.

[Sporns et al., 2005] Sporns, O., Tononi, G., Kötter, R., O'Neill, M., and Young, M. (2005). The Human Connectome: A Structural Description of the Human Brain. *PLoS Comput. Biol.*, 1(4):e42.

[Spreng et al., 2016] Spreng, R. N., Stevens, W. D., Viviano, J. D., and Schacter, D. L. (2016). Attenuated anticorrelation between the default and dorsal attention networks with aging: evidence from task and rest. *Neurobiol. Aging*, 45:149–160.

[Sridharan et al., 2008] Sridharan, D., Levitin, D. J., and Menon, V. (2008). A critical role for the right fronto-insular cortex in switch-

ing between central-executive and default-mode networks. *Proc. Natl. Acad. Sci. U. S. A.*, 105(34):12569–12574.

[Tagliazucchi et al., 2012] Tagliazucchi, E., Balenzuela, P., Fraiman, D., and Chialvo, D. R. (2012). Criticality in large-scale brain FMRI dynamics unveiled by a novel point process analysis. *Front. Physiol.*, 3:15.

[Tagliazucchi and Laufs, 2014] Tagliazucchi, E. and Laufs, H. (2014). Decoding Wakefulness Levels from Typical fMRI Resting-State Data Reveals Reliable Drifts between Wakefulness and Sleep. *Neuron*, 82(3):695–708.

[Tagliazucchi et al., 2016] Tagliazucchi, E., N, C., ET, B., and H, L. (2016). Deep sleep divides the cortex into opposite modes of anatomical-functional coupling. *Brain Struct. Funct.*, 221(8):4221–4234.

[Tagliazucchi et al., 2013] Tagliazucchi, E., Von Wegner, F., Morzelewski, A., Brodbeck, V., Jahnke, K., and Laufs, H. (2013). Breakdown of long-range temporal dependence in default mode and attention networks during deep sleep. *Proc. Natl. Acad. Sci. U. S. A.*, 110(38):15419–15424.

[Tognoli and Kelso, 2014] Tognoli, E. and Kelso, J. A. (2014). The Metastable Brain.

[Tononi et al., 1994] Tononi, G., Sporns, O., and Edelman, G. M. (1994). A measure for brain complexity: relating functional segregation and integration in the nervous system. *Proc. Natl. Acad. Sci.*, 91(11):5033–5037.

[Toutain et al., 2020] Toutain, T. G., Baptista, A. F., Japyassú, H. F., Rosário, R. S., Porto, J. A., Campbell, F. Q., and Miranda, J. G. V. (2020). Does meditation lead to a stable mind? Synchronous stability and time-varying graphs in meditators. *J. Complex Networks*, 8(6):1–14.

[van den Heuvel et al., 2012] van den Heuvel, M. P., Kahn, R. S., Goñi, J., and Sporns, O. (2012). High-cost, high-capacity backbone for global brain communication. *Proc. Natl. Acad. Sci. U. S. A.*, 109(28):11372–7.

[Van Den Heuvel et al., 2009] Van Den Heuvel, M. P., Mandl, R. C., Kahn, R. S., and Hulshoff Pol, H. E. (2009). Functionally linked resting-state networks reflect the underlying structural connectivity architecture of the human brain. *Hum. Brain Mapp.*, 30(10):3127.

[van den Heuvel and Sporns, 2011] van den Heuvel, M. P. and Sporns, O. (2011). Rich-club organization of the human connectome. *J. Neurosci.*, 31(44):15775–86.

[Whitfield-Gabrieli and Nieto-Castanon, 2012] Whitfield-Gabrieli, S. and Nieto-Castanon, A. (2012). Conn : A Functional Connectivity Toolbox for Correlated and Anticorrelated Brain Networks. *Brain Connect.*, 2(3):125–141.

[Yu et al., 2019] Yu, M., Linn, K. A., Shinohara, R. T., Oathes, D. J., Cook, P. A., Duprat, R., Moore, T. M., Oquendo, M. A., Phillips, M. L., McInnis, M., Fava, M., Trivedi, M. H., McGrath, P., Parsey, R., Weissman, M. M., and Sheline, Y. I. (2019). Childhood trauma history is linked to abnormal brain connectivity in major depression. *Proc. Natl. Acad. Sci.*, 116(17):8582–8590.

[Zalesky et al., 2014] Zalesky, A., Fornito, A., Cocchi, L., Gollo, L. L., and Breakspear, M. (2014). Time-resolved resting-state brain networks. *Proc. Natl. Acad. Sci. U. S. A.*, 111(28):10341–10346.

[Zhao et al., 2015] Zhao, T., Cao, M., Niu, H., Zuo, X. N., Evans, A., He, Y., Dong, Q., and Shu, N. (2015). Age-related changes in the topological organization of the white matter structural connectome across the human lifespan. *Hum. Brain Mapp.*, 36(10):3777–3792.

Agraeixo

A mi querido maestro, Gustavo Deco, que creíste en mí cuando ni yo misma era capaz de hacerlo. Gracias por mostrarme el camino de la sabiduría y el conocimiento, con diplomacia, vino y humildad. Te estaré infinitamente agradecida por darme la oportunidad de trabajar contigo, por tus consejos profesionales y personales, por darme la libertad y confianza para explorar cualquier tema que despertara mi atención. Al Josep Puig, gran part d'aquesta tesi ha sigut gràcies a tu. Merci per mostrar-me que, malgrat tot, és possible no perdre mai la motivació i la passió per la feina. A l'Estela Càmara, per introducir-me en el fascinant món de la neuroimatge. A Yoni, por ayudarme cuando lo necesitaba. Ojalá podamos diseñar muchas más figuras juntos. Al Carles Biarnès, el tècnic més pro que he conegut mai.

A totes aquelles amigues i dones magnífiques que tant admiro i que m'han acompanyat durant aquest procès: la Venera, la Coco, la Daniela, la Dania, la Marcia, la Javiera, la Claudia, la Laura, la Irene, la Noelia, la Carlota, la Silvana, la Ada. Al Joan Rodríguez, pel suport i per les escapades on m'aciença del regne animal. Als amics del poble que sempre hi són quan necessito una pinta: el David, el Dani i el Josep. A Javi, por los cafés y las conversaciones que no interesan a nadie.

Special thanks to the Mind & Life Institute for awarding me with the Francisco J. Varela Research Grant. Thanks to all the collaborators who have shared the neuroimaging data and made this research possible: Dr Kringelbach, Dr Tagliazucchi, Dr Sitt, Dr Laufs, Dr Jacobs, and Dr Laureys. A tota la gent del Grup de Neurociencia Computacional i a tot el Centre de Cervell i Cognició de la Universitat Pompeu Fabra.

I a la meva estimada familia, als que hi són i als que ja no hi són. No podria haver-ne tingut una de millor: als meus pares pel seu amor incondicional, Jose Manuel i Mari Carmen; al meu germà i millor amic, Marc; als meus meravellosos oncles, la Espe i el Pedro, per ser-hi sempre; a la Cruz i el Pepe, a la Feli i el Fernando, a l'Isra i l'Arantxa, a la imparable Paqui; i per supósat, al meu amazonis, que m'ha acompanyat durant el confinament i la escriptura d'aquesta tesi.

En el lugar correcto en el momento adecuado; así me siento.